Dipl.-Ing. Robert Josef Enzinger

New Insights into Phase Formation Processes in Al-Mg-Si- and in Ti-V-alloys by High-Precision Isothermal Dilatometry

DOCTORAL THESIS

to achieve the university degree of
Doktor der technischen Wissenschaften

submitted to

Graz University of Technology

Supervisor

Univ.-Prof. Dr.rer.nat. Roland Würschum

Institute of Materials Physics

Graz, July 2021

Abstract

The controlled formation of secondary phases in alloys occurring as a reaction to sophisticated heat treatments is capable of decisively influencing their mechanical performance. Since, amongst others, these processes are accompanied by dimensional changes of the specimen, dilatometry which measures the length changes arising upon any kind of heat treatment, represents an indispensable method to investigate them.

Within this doctoral thesis, a self-designed and -constructed laser dilatometer featuring a superior resolution of several nanometres with a minimised drift over times as long as 10^6 s has been applied to study the secondary phase formation processes in two lightweight alloys. This is, on the one hand, a commercial-grade dilute Al-Mg-Si-alloy (AW 6060) with about half an atom percent Mg and Si and, on the other hand, a Ti-V-alloy with about 21 at% V and two different oxygen contents. For both alloy systems, the phase formation processes appearing upon isothermal ageing after solution annealing and quenching have been investigated.

For the Al-Mg-Si-alloy, a quantitative model has been created, which allows to calculate the length changes to be expected upon the formation of a maximum amount of its two most important *precipitation phases*, β'' and β'. By correlating the distinct length change features of the isothermal measurements recorded in the temperature range of 170 °C to 260 °C with these calculations, both phases could unambiguously be detected. Additionally, these considerations allow conclusions about the most probable lattice structure and composition of both phases, two quantities which have not been fully resolved until today. With respect to a kinetic analysis, a description of the measurements in the framework of the

Johnson-Mehl-Avrami-Kolmogorov kinetic equations has been found to be suitable. Besides yielding the activation energies for the formation of both precipitation phases, which are mandatory for any kind of simulation, these equations reveal the formation order of those phases in dependence of temperature and ultimately allow to draw part of the isothermal time-temperature-precipitation-diagram for this alloy, which is urgently sought for in industry.

In the case of the Ti-V-alloy investigated, a similar quantitative model has been created for the phases known to appear in this material in the temperature range up till 450 °C. By correlating it again to distinct features of the measurements, the phase regions of two formation modes of the metastable ω-phase and of its transformation to the equilibrium α-phase could unambiguously be identified. Furthermore, this model has been used to characterise the ω-phase particles with respect to their final composition after long-term ageing, a task which is not easily done by other techniques due to their nanometre size. Based on the Austin-Rickett kinetic equations, which have been found to be suitable to describe ω-formation, part of the isothermal time-temperature-transformation-diagram has been created. In this diagram, the influence of the oxygen content on formation kinetics gets most evident. Since oxygen is always a constituent of Ti-alloys and small changes in its concentration are known to decisively influence their mechanical properties, these investigations are highly relevant for research and industry.

In the third part of this thesis, a model for the kinetics of vacancies annealing at dislocations under the important condition of time-linear heating has been developed. Furthermore, a yet existing one for the isothermal annealing of vacancies at grain boundaries has been converted to the conditions of time-linear heating. By combining it with another kinetic model for non-isothermal recrystallisation, for the first time, differential dilatometry measurements of the full annealing behaviour of a severely plastically deformed Ni-sample could be modelled.

Kurzfassung

Die kontrollierte Bildung von Sekundärphasen in Legierungen als Reaktion auf ausgefeilte Wärmebehandlungen ermöglicht es, deren mechanische Eigenschaften entscheidend zu beeinflussen. Da solche Prozesse unter anderem mit Änderungen der Probenabmessungen einhergehen, stellt Dilatometrie, welche die Längenänderungen als Reaktion auf beliebige Wärmebehandlungen misst, eine unverzichtbare Methode zu deren Untersuchung dar.

In dieser Doktorarbeit wurde ein selbstentworfenes und -konstruiertes Laserdilatometer, welches eine überlegene Auflösung im Bereich einiger Nanometer bei minimaler Drift über Zeitspannen bis 10^6 s besitzt, verwendet, um Bildungsprozesse von Sekundärphasen in zwei Leichtmetalllegierungen zu untersuchen. Dies ist einerseits eine handelsübliche, niedriglegierte Al-Mg-Si-Legierung (AW 6060) mit in etwa einem halben Atomprozent Mg und Si, andererseits eine Ti-V-Legierung mit in etwa 21 at% V und zwei unterschiedlichen Sauerstoffgehalten. Im Falle beider Legierungssysteme wurden die Phasenbildungsprozesse während des isothermen Auslagerns nach Lösungsglühen und Abschrecken untersucht.

Für die Al-Mg-Si-Legierung wurde ein quantitatives Modell erstellt, welches die Berechnung der zu erwartenden Längenänderungen als Reaktion auf die Bildung eines maximalen Anteils ihrer beiden wichtigsten *Ausscheidungsphasen*, β'' und β', erlaubt. Durch die Korrelation der deutlich ausgeprägten Charakteristika der isothermen Längenmessungen im Temperaturbereich von 170 °C bis 260 °C mit diesen Berechnungen konnten beide Phasen eindeutig detektiert werden. Weiterhin sind Rückschlüsse auf die wahrscheinlichsten Gitterstrukturen und Zusammensetzungen beider Phasen möglich, zwei Größen, über die bis heute keine vollkommene Klarheit besteht. Hinsichtlich einer kinetischen Analyse erscheint die Beschrei-

bung im Rahmen der Johnson-Mehl-Avrami-Kolmogorov-Kinetik passend. Neben den Aktivierungsenergien für die Bildung beider Ausscheidungsphasen, welche obligatorisch für jede Art von Simulation sind, offenbart dieses Modell die temperaturabhängige Bildungsreihenfolge dieser Phasen und erlaubt es zuletzt, einen Teil des isothermen Zeit-Temperatur-Ausscheidungs-Diagramms zu erstellen, Diagramme, nach welchen in der Industrie dringend gesucht wird.

Im Fall der untersuchten Ti-V-Legierung wurde ein analoges, quantitatives Modell für jene Phasen aufgestellt, die bekannterweise im Temperaturbereich bis 450 °C in diesem Material auftauchen. Durch die Korrelation mit den Charakteristika der gemessenen Längenänderungen konnten auch in diesem System die Phasengebiete zweier Bildungsmodi der metastabilen ω-Phase und ihrer Umwandlung zur α-Gleichgewichtsphase eindeutig identifiziert werden. Weiterhin wurden dieses Modell verwendet, um die ω-Partikel hinsichtlich ihrer Endkonzentration nach Langzeitwärmebehandlungen zu charakterisieren - eine Aufgabe, welche mittels anderer Techniken wegen der nanoskaligen Größe der Partikel nicht einfach zu bewältigen ist. Basierend auf der Austin-Rickett-Kinetik, welche in diesem Fall als für die Beschreibung angemessen befunden wurde, konnte ein Teil des isothermen Zeit-Temperatur-Umwandlungs-Diagramms erstellt werden. In diesem Diagramm wird der Einfluss des Sauerstoffgehalts am deutlichsten sichtbar. Da Sauerstoff immer ein Bestandteil von Ti-Legierungen ist und kleine Konzentrationsänderungen bereits entscheidenden Einfluss auf deren Eigenschaften zeigen, sind diese Untersuchungen höchst relevant für Forschung und Industrie.

Im dritten Teil dieser Doktorarbeit wurde ein kinetisches Modell für das Ausheilen von Leerstellen an Versetzungen während des Aufheizens mit konstanter Rate entwickelt. Weiterhin wurde ein schon existierendes Modell für das Ausheilen von Leerstellen an Korngrenzen unter isothermen Bedingungen auf das Aufheizen mit konstanter Rate umgelegt. Durch Kombination desselben mit einem weiteren kinetischen Modell für die nicht-isotherme Rekristallisation konnten zum ersten Mal Differenzdilatometriemessungen aller Ausheilprozesse in stark plastisch verformten Ni-Proben modelliert werden.

Table of Contents

1 | Introduction

Gearbox housings and cooking utensils made of aluminium alloys, laptop housings and steering wheels made of magnesium alloys, artificial hip joints and eyeglass frames made of titanium alloys - this is just a minute number of examples for the manifold applications of the three most important lightweight metals in various fields of our modern-day life. In this context, besides finding new alloy systems with even more beneficial combinations of mechanical, physical and chemical properties, the *improvement* of processing strategies for the systems yet in use with the same objective represents an issue of permanently high topicality in materials science[1,2].

As a first important example, the optimisation of the mechanical and thermal treatments which are commonly applied to several classes of aluminium alloys, aims at obtaining even higher strength or hardness values[3]. In doing so, these alloys become suitable to replace heavy steel components in many fields of application as, e.g., in the automotive or aerospace industry, meeting thereby the request of reduced fuel consumption[4,5]. Another example of great current interest is concerned with several Ti-alloys, which are particularly well suited to be used for medical applications as artificial joints or screws due to their excellent biocompatibility and deformation characteristics similar to those of bone. Modifying the alloy composition, however, which appears reasonable from several perspectives, may lead to large hardness increases, causing stress shielding effects accompanied by bone degradation[6,7]. Optimised mechanical and thermal treatments may counteract this undesired effect[8].

From a material-related point of view, in both cases, the significant property changes can

be traced back to the formation of one or several secondary phases, which are intentionally initiated in case of the Al-alloy by applying special heat treatments[1], but are unwanted to happen in the case of the Ti-alloys[9]. In general, these phase formation processes are rather complex, since they often take place via several steps, i.e. metastable intermediate phases, and may get influenced by many external and internal parameters. Examples for external parameters include temperature and time but also the deformation conditions according to previous mechanical treatments. Internal parameters are, e.g., the size distribution of secondary phase particles, their lattice structure and composition and the homogeneity of distribution to name just a few. Because of the extensive impact of secondary phases on many material properties, however, it is desirable to know them and all influencing factors at maximum possible detail.

Dilatometry is one standard method for thermal analysis, which has been used to determine the length or volume changes of solid and liquid samples arising upon arbitrary kinds of temperature programmes at the highest precision yet for more than one and a half centuries[10,11]. Today, especially linear dilatometers are used, which measure the length changes as a reaction to a certain temperature profile. Besides basic measurements of the thermal expansion which is one of the most fundamental properties of any material, (secondary) phase formation processes can be studied as well according to their effect on the sample length[12]. For this purpose, specimen are subjected to temperature programmes, during which phase formation takes place in controlled manner allowing the systematic investigations of these processes[1]. As in the case of steels, quenching from high temperatures is mostly applied as a first step, which yields a state, where phase formation would start, if not being inhibited due to the low temperatures. Subsequently, either heating at various constant rates or fast heating to certain temperatures which are subsequently kept constant for some time, are applied in the most cases.

The formation of various secondary phases causes length changes of different size and sign, i.e., they may either be positive or negative, and get visible as peaks[12,13]. In the case of time-linear heating, thermal expansion superimposes these peaks, so the measurements have

to be corrected in order perform proper analyses of these processes. In any case, deriving quantitative models which establish the connection in between the variations in the sample length and changes on the microscopic level, i.e., the formation of a phase with a certain lattice structure and composition as well as the concurrent changes in the matrix, is indispensable for an in-depth understanding of these processes. This is particular important for systems featuring not only one, but several metastable phases, which may appear in parallel or transform into another. Additionally, compositions and lattice structures of these phases are often not exactly known, so by using these models together with the length changes measured, the correct lattice structures and compositions may be worked out[12].

From a technical point of view, in particular in the case of dilute alloys with the alloying element concentration amounting to below 1 at%, dilatometers featuring a high resolution are required, since the length changes to be expected are often correspondingly small in most cases[12]. If available, they provide the opportunity to continuously follow the phase formation and transformation processes, what allows conclusions to be drawn about the real kinetics of the processes, other than, e.g., the pictures of imaging techniques, which are undoubtedly important, but provide only snapshots of a minute section of the sample.

Within this thesis, studies concerning the phase formation processes taking place upon isothermal ageing in two light weight alloy systems based on dilatometry measurements are presented.

Chapter 4, *"Precipitate Formation Processes in an Al-Mg-Si-Alloy"* addresses investigations of the secondary phase formation processes in AW 6060, a dilute Al-Mg-Si-alloy, upon common heat treatments. Especially in this kind of alloy, often not the equilibrium phase is immediately formed, but metastable intermediate phases. The two most important of those are called β'' and β', where the formation of β'' is known to be responsible for the largest hardness increases. Mainly due to their small dimensions, lattice structures and compositions of these precipitation phases are not known with absolute certainty. Thus, Sect.4.5.1 focusses on creating mathematical models which establish the connection of lattice structures and compositions and the length changes measured, helping identifying both quantities. The

second part of the investigations, Sect.4.5.2, is concerned with finding a kinetic model which correctly reproduces the full dilatometric measurements for all temperatures and reveals the separate contributions of β'' and β'. Since such a model characterises the full time-temperature-behaviour of the system, it allows for extracting the very important formation rates and activation energies.

Chapter 5, *"Phase Formation Processes in a Strongly β-Stabilised Ti-V-Alloy"*, deals with secondary phase formation processes in β-stabilised Ti-alloys with about 21 at% V and two different oxygen contents. Here, upon common heat treatments, the formation of metastable ω-phase via different formation modes is observed, which may possibly transform into the equilibrium phase dependent on temperature and time. In the first part of this chapter, Sect.5.5.1, similar models as in the case of the Al-alloy are derived, which make it for the first time possible to explain the distinct length change features appearing for this system on the basis of lattice structures and phase fractions of the individual phases. In return, the models developed allow the identification of corresponding phase regions and for some quantitative calculations, which are described in Sect.5.5.3. The second part of this chapter, Sect.5.6, is concerned with finding an adequate kinetic model and applying it to the measurements. As in the case of the Al-alloy investigated, this yields the temperature dependent formation rates and allows to create part of the isothermal time-temperature-transformation-diagram, where the influence of varying oxygen contents becomes best visible. It is discussed in Sect.5.6.3.

Lastly, chapter 6, *"Kinetics of Vacancy Annealing"*, deals with finding mathematical descriptions for the annealing behaviour of vacancies at dislocations and at grain boundaries of various shapes under the important conditions of time-linear heating. In the following, one of the models developed is applied to measurements obtained for severely plastically deformed Ni. Obviously, this subject is not directly connected to secondary phase formation processes. Nevertheless, vacancy annealing is a highly relevant topic for any kind of secondary phase formation process, since vacancies get quenched in the course of the heat treatment and contribute in various ways, as, e.g., in the case of Al-Mg-Si-alloys, by supporting Mg and Si

in being transferred to the precipitates.

Before dealing with the investigations performed at lightweight alloys and the models created for vacancy annealing, in chapter 2, some basics concerning dilatometry and dilatometric measurements are given. Most of the measurements have been performed with a self-developed and -constructed laser dilatometer. Accordingly, in chapter 3, the dilatometer is described first in its original state in Sect.3.1. Afterwards, in Sect.3.2, the enhancements installed by the author during his doctoral studies are presented.

Basic information concerning the materials investigated and the state of research concerning the physical processes in these materials are given in the beginning of the respective chapters to improve readability.

List of publications related to this thesis

Resch, L.; Klinser, G.; Hengge, E.; **Enzinger, R.**; Luckabauer, M.; Sprengel, W.; Würschum, R.

Precipitation processes in Al-Mg-Si extending down to initial clustering revealed by the complementary techniques of positron lifetime spectroscopy and dilatometry

J. Mater. Sci., **53** (2018) 14657–14665

Okamoto, N.; Kasatani, S.; Luckabauer, M.; **Enzinger, R.J.**; Tsutsui, S.; Tane, M.; Ichitsubo, T.

Evolution of microstructure and variations in mechanical properties accompanied with diffusionless isothermal ω transformation in β-titanium alloys

Phys. Rev. Mater., **4** (2020) 123603

Enzinger, R.J.; Luckabauer, M.; Ichitsubo, T.; Würschum, R.

Modelling dilatometry data of isothermal ω-phase formation in a strongly β-stabilised TiV-alloy

Mater. Sci. Forum, (2021) 1851–1856.

List of publications not related to this thesis

Resch, L.; Luckabauer, M.; Helthuis, N.; **Enzinger, R.**; Okamoto, N.L.; Ichitsubo, T.; Sprengel, W.; Würschum, R.

Search for vacancies in concentrated solid-solution alloys with fcc crystal structure

Phys. Rev. Mater., **4** (2020) 060601

2 | Basics: Dilatometry

In this chapter, the most important basics concerning the measurement technique of *dilatometry* will be given. This includes a categorisation of this method into the vast class of thermal analysis methods as well as descriptions of its basic principle, of the types of dilatometers in use, of the commonly applied measuring modes, and of the results to be obtained based on dilatometry measurements. With regards to the basics and the state of research for each sample material investigated in the course of this thesis, they are not given here but in the respective chapters below to improve readability.

2.1 Thermal analysis techniques and dilatometry

Dilatometry (lat. dilatatio: expansion, meter: measure) or more exactly *thermo*-dilatometry deals with *the investigation of dimensional changes appearing upon temperature variations at zero load* and is classified today as one method belonging to the vast group of thermal analysis (TA) techniques[14]. These techniques have been extensively used in materials sciences in order to obtain information about the temperature behaviour of a variety of the most fundamental physical properties, thus providing the indispensable basis of materials characterisation and design. Examples include thermally-induced variations of the mechanical, electrical, magnetic and optical properties as well as changes in sample mass and dimensions[14].

If aiming at the investigation of dimensional changes, techniques allowing to examine their

variation as a function of pressure or stress represent another important branch of analysis methods. Since in the course of producing and processing metallic as well as non-metallic materials, mostly combinations of thermal and mechanical treatments are applied[15], they are grouped together and designated as thermo-mechanical analysis (TMA) methods. To this class belong all techniques, where measurements in dependence of pressure (stress) at a certain constant temperature also other than $T_{amb.}$, or, in dependence of temperature at constant and, in particular, non-negligible load are performed. Thus, besides thermo-dilatometry which may even be conducted under increased load, designated accordingly as (high-)pressure dilatometry[16], measuring dimensional changes upon (hot) tensile, torsion or flexure testing are attributed to the branch of TMA-methods.

When talking about TA-techniques, clear distinction must be made between heat fluxes and temperature changes. In the most cases, including dilatometry, a heat flux into/out of the investigated system is adjusted in order to obtain a desired temperature change. These temperature changes are recorded together with the concomitant changes of the state variable to be examined as, e.g., the electric polarisation, the magnetisation or the sample dimensions. In contrast, in the case of *thermometry*, the by far oldest TA-technique, temperature is the state variable to be measured here, where this time, the heat flux into/out of the system is adjusted to be constant[17]. In doing so, characteristics of the temperature changes can be analysed, which may e.g. be caused by the latent heat coming along with phase formation/transformation processes.

Especially with respect to other TA-techniques, it has to be emphasised that the dimensional changes measured in the course of dilatometry are a *direct* consequence of the temperature changes. Many other TA-techniques suffer from instrumental thermal lag effects, as, for instance, pertains to differential scanning calorimetry (DSC) measurements of the heat capacity changes. These lag effects are negligible for dilatometry, where a homogeneous temperature field within the specimen can be easily maintained[18].

2.2 Expansion behaviour of matter

Dimensional changes appearing as a reaction to temperature variations belong to the most fundamental properties of any kind of matter. With only a few exceptions, pure solid materials are found to expand upon heating and to contract upon cooling over the entire temperature range in this phase state. This effect is directly connected to the anharmonicity of the atomic potential curves, which makes the middle positions of the atoms move away from each other when temperature increases[19]. It may, however, be superimposed by other contributions, in particular, when more complex systems comprising several components are investigated, which may cause a temporarily reduced expansion or even contraction upon heating.

In the case of solids, length or volume changes are reasonably considered when speaking of thermal expansion, which are described by the so-called linear and volume coefficients of thermal expansion (CTEs), α and β:

$$\alpha(T) = \frac{1}{L_0} \cdot \frac{\mathrm{d}L}{\mathrm{d}T} \tag{2.1a}$$

$$\beta(T) = \frac{1}{V_0} \cdot \frac{\mathrm{d}V}{\mathrm{d}T}. \tag{2.1b}$$

In these definitions, L_0 and V_0 are the sample length and the volume under standard conditions, which are determined before launching a measurement. Since especially in the case of many pure metals, their CTEs are constant in a certain temperature range above $T_{amb.}$, α and β are often defined as average expansion coefficients.

In general, the extent of the thermal expansion of solids is closely related to the kind of bonding and to its crystal structure. As a rule of thumb, covalent and ionic materials show the lowest CTEs (e.g., $\sim 0.5 \cdot 10^{-6}\,\mathrm{K}^{-1}$ for fused silica at 20 °C), metals show intermediate ones (e.g., $\sim 23 \cdot 10^{-6}\,\mathrm{K}^{-1}$ for aluminium at 20 °C) and molecularly-bonded materials the highest

ones (e.g., $\sim 120 \cdot 10^{-6}\,\mathrm{K}^{-1}$ for Teflon® at 20 °C)[14]. Besides this, a lot of other factors may influence the thermal expansion of solids as, e.g., solid-solid phase transitions, secondary phase formation processes or even magnetostriction phenomena as in case of Invar, which are found to either reduce or enhance the thermal expansion coefficients[20]. Furthermore, solids may show anisotropic behaviour, i.e. the CTEs vary in different directions and may even be found to be negative in some directions.

Besides determining the thermal expansion of any kind of solid material, dilatometry has proved to be especially useful to investigate the shrinkage behaviour during sintering of ceramics and metals, the glass transition temperature of polymers, structural defects like vacancies, dislocations, and grain boundaries in metals, recrystallisation processes, and precipitation processes in alloys to name just a few[14].

In this thesis, amongst others, time-linear heating measurements are conducted at Ni-samples which had previously been subjected to a certain mechanical treatments. Since the thermal expansion behaviour of Ni, however, is not relevant in this case but only the effects caused by the mechanical treatment, a well-annealed reference sample is simultaneously measured, which is used for subtracting the thermal expansion later on. This measurement mode is described in detail in the following section.

Furthermore, with respect to the self-constructed dilatometer used to perform the greatest part of the measurements for this thesis, advantage has been taken of the low expansion coefficients of fused silica and Invar which have been used for some building components (see chapter 3).

2.3 Dilatometry: measurement principle

The general measurement principle of dilatometry is rather simple, whereas its technical implementation with respect to integral components and measuring devices is versatile and may turn out to be more complex according to the requirements.

In the early days of their standard application, more easy-to-use *volume dilatometers* were

quite common to be utilized for all kinds of investigations[21]. Today, mostly *linear dilatometers* are in use, where the length changes arising upon different temperature programmes are measured. When examining solid samples, one major advantage of the use of linear dilatometry instead of volume dilatometry is that possible macroscopic anisotropies in the dimensional changes can easily be detected and characterised by examining the sample in different alignments to the measurement direction.

In Fig.2.1, a schematic drawing of the basic parts of a linear dilatometer is shown. As in-

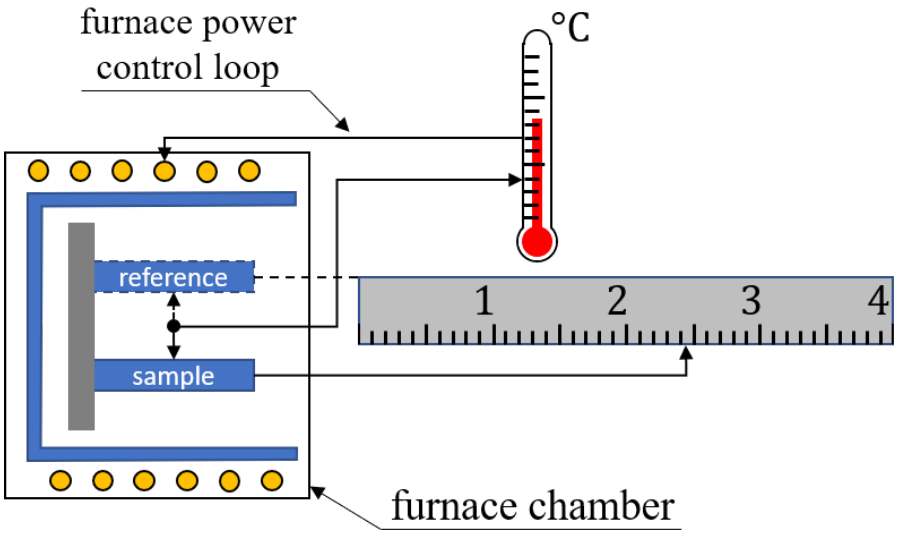

Figure 2.1: Schematic drawing of the measurement principle of dilatometry[14]. Measurements are either performed in an absolute mode, where only length changes of the sample are investigated or in differential mode, where the length changes of the sample are corrected with the ones of a reference sample (dashed lines).

dicated in this figure, distinction is made in between measuring the length changes of only a single sample (absolute dilatometry) or of the sample and (simultaneously) of a reference sample (differential dilatometry)[22].

Here, in the early days of linear dilatometry, a reference sample consisting of materials which show a well-known, large thermal expansion (e.g. pure aluminium), has often been used to determine temperature. When temperature is determined in another way, however, the measurement of the reference sample provides the possibility to correct the one obtained for the sample in certain ways. In doing so, differential dilatometry has been applied for various

systems, where the sample was subjected to a certain kind of modification (e.g. alloying, mechanical treatments), but the reference was not. By subtracting the reference signal from the sample signal, only the signal caused by the modifications is left back for analysis [22].
As mentioned, one possibility to simultaneously record temperature is by making use of the thermal expansion of the reference sample. Besides this, various methods of direct and indirect temperature measurements are used, where its determination by thermocouples is the most common. In the most cases, the measured temperature controls via a feedback loop the power which is supplied to the furnace.

2.4 Dilatometry: devices and measurement modes

Taking this basic principle as a starting point, dilatometers are commonly distinguished according to certain aspects, i.e., depending on

(i.) whether changes in length or volume are measured,

(ii.) which kind of device is used to determine the dimensional changes,

(iii.) the measurement modes which can be performed by the dilatometer.

Concerning (i.), as described above, most modern dilatometers are designed to record length changes. If the volume change of solid sample has to be known for some reason, there exists a relationship to the length changes, which turns out to become especially simple in the case of isotropic samples and will derived in the following (see Eq.2.2).
In order to make the absolute length or volume changes obtained for samples with different sizes and geometries comparable, they are indicated commonly as relative values, i.e., by dividing them by the sample length L_0 or volume V_0 under ambient or other well-defined conditions. Consider a squared sample with the edge lengths L_1, L_2 and L_3 under ambient conditions, which experience corresponding length changes of ΔL_1, ΔL_2 and ΔL_3 upon an

arbitrary temperature change. The corresponding volume changes can be calculated via

$$\frac{\Delta V}{V_0} = \frac{(L_1 + \Delta L_1)(L_2 + \Delta L_2)(L_3 + \Delta L_3) - L_1 L_2 L_3}{L_1 L_2 L_3}$$
$$= \frac{L_1 L_2 \Delta L_3 + L_1 \Delta L_2 L_3 + \Delta L_1 L_2 L_3 + L_1 \Delta L_2 \Delta L_3 + \Delta L_1 L_2 \Delta L_3 + \Delta L_1 \Delta L_2 L_3 + \Delta L_1 \Delta L_2 \Delta L_3}{L_1 L_2 L_3}. \tag{2.2a}$$

In case of an isotropic material, the *relative* length changes in all directions are the same and will be denoted in the following as $\Delta L/L_0$. Furthermore, if the length changes are small compared to the dimensions of the sample, all terms, where two or more length differences get multiplied, can be neglected in good approximation. In this way, one gets:

$$\frac{\Delta V}{V_0} \approx \frac{\Delta L_1}{L_1} + \frac{\Delta L_2}{L_2} + \frac{\Delta L_3}{L_3} = 3\frac{\Delta L}{L_0}. \tag{2.2b}$$

This simple relationship in between relative volume change and relative length change holds for any kind of sample geometry. If a sample shows anisotropic behaviour with respect to its length changes, measurements in several alignments of the sample with respect to the measurement direction have to be performed in order to estimate the volume changes.

Conerning (ii.), there exist several methods to measure the length changes of the samples, which are usually stated when speaking about a certain dilatometer.

In the course of *capacitance dilatometry*, sample length changes are transformed to changes in the distance of two capacitor plates, where the one is fixed and the other moveable and connected to the sample[23]. Variations of the distance of the capacitor plates are equivalent to changes in the capacitance, which are measured electronically. This measurement principle turns out to be quite advantageous due to the possibility to miniaturise these devices and to thus run them e.g., inside the limited space of cooling devices, where extremely low temperatures are generated[24,25]. The resolution of some measuring devices is described to amount to less than 1 Å[25].

Concerning *optical dilatometry*, this designation is used, on the one hand, for dilatometers, where absolute sample length changes are recorded via interferometry and, on the other hand, for dilatometers where the samples are directly imaged and dimensional changes are detected by comparing consecutive pictures.

With respect to the interferometric measurement principle, Fizeau was the first to use it to reliably detect length changes in the sub-μm-range yet in 1868[10,11]. He published his comprehensive studies, where especially the anisotropic thermal expansion of a large number of minerals is reported, in a pioneering article[10]. Automatised recording of temperature changes and of concurrent length changes as well as the use of highly stable lasers interferometry represent the most significant improvements with respect to handiness and resolution since the times of Fizeau. Today, the theoretical resolution limit of optical dilatometers is in the range of several pm[26].

Optical dilatometry which uses direct imaging to record dimensional changes of the sample and of a possible reference sample, is again especially useful to investigate soft samples which would be compressed by using push-rods (see below). Here, the dilatometers are equipped with magnification devices, where digital cameras are used to capture images of the sample (and the reference sample) at certain time steps. According to the physics of optical magnification, the resolution of such devices is slightly higher than the wavelength of the light used[27].

Measuring length changes by optical dilatometry is not involved with direct sample contact, which may be advantageous in some cases. The most frequently applied dilatometry techniques, however, are based on the direct mechanical contact in between the sensor unit and the sample. In this context, *push-rod dilatometers* represent the most common type of these contact methods. As the name suggests, a rod establishes the connection in between the sample which is mounted inside the furnace, and a device which records shifts of the rod. Here, mostly linear variable differential transducers (LVDT) are used as electronic displacement sensors, where in some cases also capacitance or optical sensors are used to detect shifts of the rod[28]. Since the rods are, owed to their direct sample contact, also subjected

to temperature changes, measurements have to be corrected by respective baseline measurements. Likewise, this type of dilatometers is often implemented in differential designs and rods as well as sample holders are made of materials with low expansion coefficients as, e.g., alumina or fused silica[28].

Concerning (iii.), commonly applied temperature programmes within dilatometric investigations consist usually of several stages and are designed to initiate desired processes in a controlled manner. There is no dilatometer which is adequate to be used for any kind of situation at highest precision, but devices are designed especially for a certain kind of temperature programme.

In this regard, probably the most frequent kinds of measurements performed are such, where a *constant heating rate*, i.e., a linear increase of temperature, is applied. Besides being a natural part of almost every temperature programme, in the course of which samples are heated to elevated temperatures, such measurements are particularly suited for the determination of CTEs, where, in order to obtain them, the length changes measured have to be differentiated with respect to the temperature profile[29]. Furthermore, this kind of measurements can be used to get an overview of other processes as e.g., phase transitions and phase formation processes, which cause the length to change less or more than just thermal expansion would yield in certain temperature ranges. In case of the expansion coefficient being sufficiently constant in the respective temperature region, information about the start and finishing points of such processes can easily be derived by analysing the derivative of such measurements.

In order to perform a more accurate analysis, it is preferable to perform differential dilatometry which allows for the correction with respect to the thermal expansion. Based on measurements with different heating rates, activation energies can be derived by applying kinetic analysis methods like, e.g., Kissinger's or Ozawa's method[30,31]. These methods make use of the heating-rate dependent shift of any feature of the measurements, which is attributed to processes other than thermal expansion. Activation energies belong to the most basic

elements needed to perform any kind of theoretical calculation or simulation and are thus urgently sought.

Furthermore, by plotting start and finishing point of the processes observed against time and temperature, one ends up with a so-called continuous-heating-transformation (CHT) diagrams which are one kind of time-temperature-transformation (TTT) diagrams. In Fig.2.2 (lower part), another kind of TTT-diagram is shown, which had been obtained based on isothermal measurements (see below). Since those diagrams contain, as the designation suggests, all information about the transformation behaviour of a material, they are urgently sought for, too, e.g., in the metal producing and processing industry. Conducting measurements with constant heating rates is a standard task and is thus possible to be performed by most dilatometers, where the accessible temperature range and applicable heating rates are different from one to another device.

With respect to cooling, not all dilatometers are able to perform this procedure at constant rates, i.e., in active/controlled manner, but, in the case of most devices, at least passive or uncontrolled active cooling is possible. In this regard, quenching dilatometers are devices, where controlled cooling with constant rates can be performed. If having conducted measurements at various cooling rates, these may also be used to calculate activation energies and to construct non-isothermal TTT-diagrams, which are designated as continuous-cooling-transformation (CCT) diagrams in this case[32]. Since quenching is part of many heat treatments which are commonly applied to materials, some dilatometers are able to even perform *in situ* quenching.

As in the case of non-isothermal measurements, activation energies and TTT-diagrams can both be obtained also from *isothermal measurements*. In order to make processes happen, the material has to be brought into a non-equilibrium state previously, e.g., by a high-temperature treatment followed by quenching, which transforms towards its equilibrium state during the isothermal measurement[33].

Fig.2.2 illustrates, how such diagrams are obtained under these conditions in the simple case of only one phase being formed. In the upper part of this figure, the increasing phase frac-

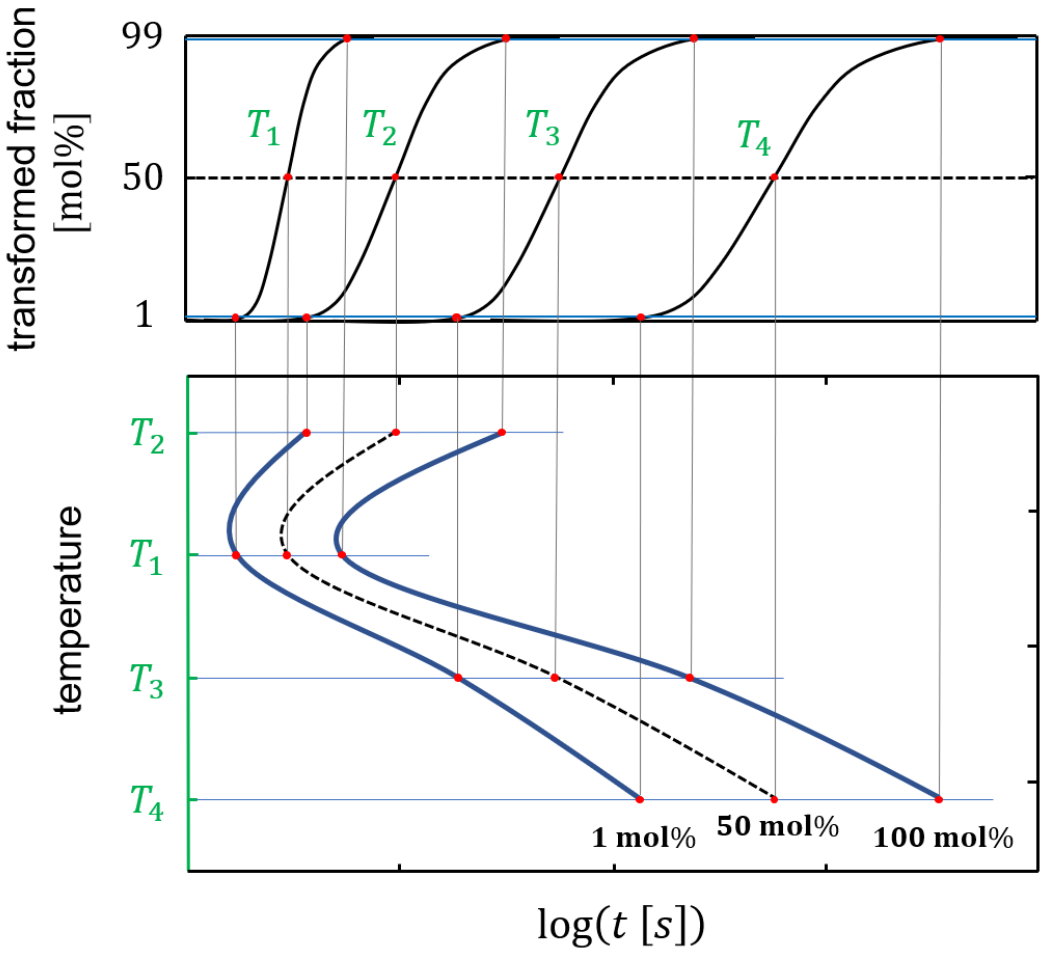

Figure 2.2: Graphical illustration of the procedure to construct an isothermal time-temperature-transformation diagram. Upper part: Transformed phase fraction in dependence of time and for several temperatures. From this diagram, time and temperature for the formation of 1, 50 and 99 mol% are determined and drawn into a corresponding diagram, as done in the lower part of this figure.

tion is drawn over time for several temperatures. Note, that the maximum phase fraction is likely to vary with temperature, so the respective percentage values are used. For every formation curve, the time is determined when the phase fraction has grown to certain values (red points, often 1, 50 and 99 mol%) at a certain temperature. As done in the lower part of Fig.2.2, these pieces of information are than drawn into a time-temperature-diagram. The procedure is analogous in case of non-isothermal measurements. Here, the phase fractions are a function of temperature, too. Concerning the phase fractions, in general, they can be determined from measurements received by various techniques as, e.g., dilatometry or dif-

ferential scanning calorimetry, which are capable of performing the respective temperature programmes, i.e., isothermal, linear heating or cooling measurements.

With respect to non-isothermal measurements, one advantage of conducting isothermal measurements at different temperatures is that phases won't get skipped unintentionally. Another advantage is the more secured determination of transformation rates and activation energies based on kinetic modelling[34]. Disadvantages relate, in particular, to the comparably long measurement times to grasp processes happening on long time scales and the necessity to hold the measuring system sufficiently stable.

As applied in the framework of differential scanning calorimetry[35], temperature *modulated measurements* either superimposed to time linear heating or at constant average temperature can be performed by some dilatometers[26]. Imprinting a modulation allows to mathematically decouple all processes which happen on time scales substantially larger than the modulation time period from such processes happening on time scales substantially smaller than it. Speaking more exactly, slow processes will not cause relevant contributions on average during one period duration, but fast processes will be able to catch up with the modulation. In the most cases, modulation frequencies are chosen in a way, so that only thermal expansion is able to follow it. In doing so, the result will be the same as if carrying out difference dilatometry, but with any uncertainties missing, which could possibly arise due to investigating a second sample[36].

Within this doctoral thesis,

- a self-designed and -constructed laser dilatometer is used to conduct absolute high-precision length change measurements. This device is especially designed for high-stability isothermal measurements and is able to perform in situ quenching. It is described in detail in the following chapter.

- a commercial vertical push-rod dilatometer (Linseis L75VD500LT) is used to conduct time-linear heating measurements in differential configuration, i.e., a well-annealed reference sample is simultaneously measured in order to subtract the thermal expansion.

3 | Experimental: Laser Dilatometer

The first part of this chapter deals with descriptions concerning the dilatometer at the Institute of Materials Physics (TU Graz), which has been used to performed the majority of the measurements presented and discussed within this thesis - a self-designed, self-constructed laser dilatometer. This device has been equipped with manifold improvements by the author in the course of his doctoral studies, which are described in the second part of this chapter.

3.1 Description of the set-up

All measurements which have been conducted to investigate secondary phase formation processes in Al- and Ti-alloys, were performed with a self-designed and -constructed laser dilatometer at the Institute of Materials Physics. Details about the set-up of this device have already been given elsewhere[26]. With respect to most commercially available dilatometers, it is characterised in particular by ...

- the possibility to produce temperature variations in the sample material in more fast and precise manner than in case of common devices.
- an exceptionally high resolution which allows to reliably resolve length changes of only several nanometres under most conditions.

Concerning the measurement principle, it allows to perform specifically ...

- isothermal measurements of unprecedented long-term stability owing to manifold arrangements made to avoid any kind temporal drift.
- modulated measurements of high modulation frequency owing to the non-contact, interferometric measurement principle.

In the following, the set-up and functionality of the dilatometer is described in detail in order to make these statements comprehensible. The explanations relate to the conditions present, when responsibilities for the device had been transferred to the author in the course of his doctoral studies. The enhancements installed by the author during his doctoral studies are described in the following chapter.

Mirror furnace:

Fig.3.1 shows the core part of the dilatometer, its furnace, wherein, depending on the measurement mode, either the sample and reference plane (high-precision absolute dilatometry, shown in this figure) or the sample and reference sample (differential dilatometry) are placed. Heating is done by focussed light which is emitted by surrounding halogen bulbs. Accordingly, the furnace walls are implemented as mirrors with a base plane consisting of three partially overlapping, concentrically arranged ellipses. The halogen bulbs (yellow cylinders in Fig.3.1) are positioned each in one of the outer focus points of these ellipses perpendicular to the base plate. Thus, the light of each halogen bulb is reflected by its surrounding mirror into the respective second focus point (or, speaking more exactly, into the respective focus line), where sample and reference sample are positioned in two of them. The three second focus points lie closely together right in the centre of the furnace. For the sake of clarity, one of these ellipses has been drawn into Fig.3.1 together with some beam paths illustrating the way of heating the samples by light. There is no sample in the focus point spotlighted by the third bulb - it is used to implement temperature measurement as is described in detail further below. According to this special kind of heating, large heating rates of several hun-

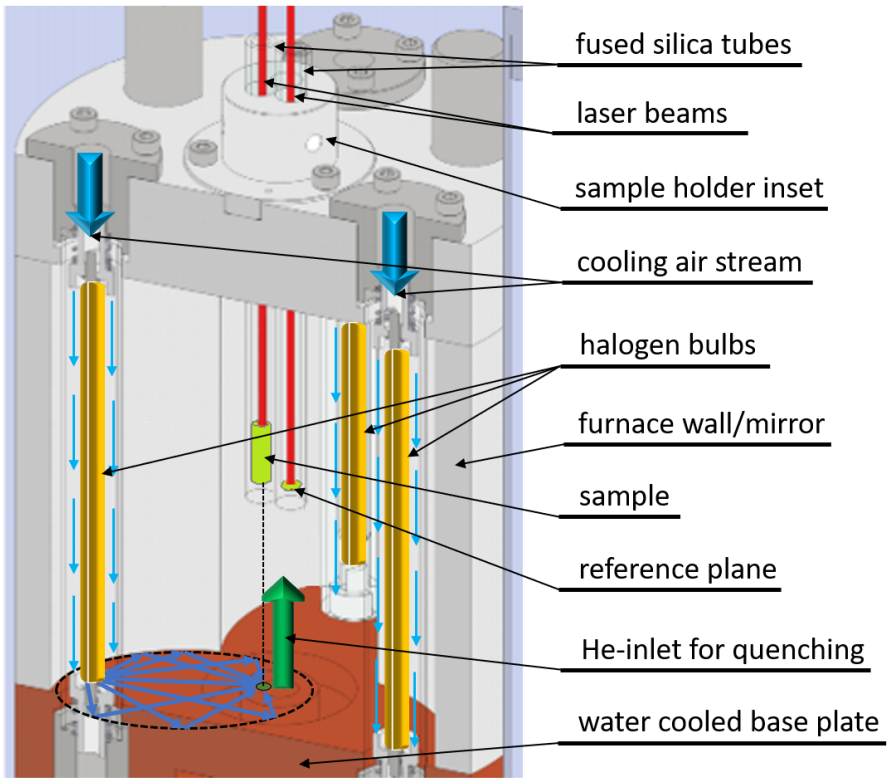

Figure 3.1: Furnace part of the laser dilatometer which has been developed and constructed at the Institute of Materials Physics (TU Graz). Two laser beams are focussed to hit the sample and a potential reference sample which are positioned in the middle of the furnace by inserting them into sealed fused silica tubes. The silica tubes are mounted inside a holder which is designed to be an inset in the cover plate of the furnace. Together with the reflecting furnace walls, the cover plate is fixed onto the water cooled base plate (copper coloured). Halogen bulbs are drawn in yellow and the helium gas stream, which can be let into the furnace for the purpose of quenching through a hole in the base plate, is indicated by a green arrow. For a detailed description of additional components and the functionality, the reader is referred to the text.

dred °C/min can be applied to yield temperatures of above 1000 °C at a minimum reaction time of the furnace of well below one second.

In order to make heating of the samples by the focussed light most effective and to prevent heat from being transferred by convection to parts of the furnace other than the sample/reference sample, it is mounted as a whole in high vacuum (final pressure $\sim 1 \times 10^{-5}$). Conversely, the halogen bulbs are not in high vacuum, but are positioned inside fused silica tubes with a continuous air flow going through them (see Fig.3.1, light blue arrows). In order to minimise heat conduction via the bulb holders to other parts of the furnace and to

guarantee a more or less constant temperature of the bulbs' surface, the air flow is adjusted correspondingly by a mass flow controller (see Fig.3.2, "MFC Air").
To sum up, a minimum reaction time of the furnace in combination with this special kind of heating principle allow for extremely fast temperature variations. Furthermore, the constant cooling of the halogen bulbs and high vacuum conditions inside the furnace suppressing any convection are just two elements being responsible for the unprecedented stability of this device.

Quenching/Cooling:

He-gas can be let directly into the furnace through a hole in the bottom plate for quenching or cooling purposes, where the mass flow has to be manually controlled by a corresponding programme (see Fig.3.1, dark green arrow and Fig.3.2, "MFC He"). For the purposes of quenching, a tube is introduced into the hole, the topside of which ends close to the bottom of the fused silica sample holding tubes (not drawn in Fig.3.1). In doing so, the He-gas is more directly blown to the samples yielding, nevertheless, comparably moderate quenching rates of several ten °C/s depending on how close the sample temperature is already to $T_{amb.}$. Automatised controlled cooling or quenching at certain rates is not possible to be conducted with this device.

Sample holder and temperature measurement:

Adjusted to the furnace design, the sample holder is also implemented in threefold symmetry. It consists of an inset with three drill holes, which can be mounted in the middle of the cover plate at the top of the furnace (see Fig.3.1). For measuring purposes, two of the drill holes are equipped with silica glass tubes which are sealed at the bottom and which possess a little lateral hole each (not drawn in Fig.3.1). When performing dilatometry measurements, the glass tubes are equipped with the sample and the reference sample/a reference plane, respectively. Sample and reference sample/reference plane are positioned at half height of the halogen bulbs, where the temperature field generated by the lamps should be hottest and

most homogeneous. In Fig.3.1, the setting to conduct high-precision absolute measurements is illustrated, where a sample (light green cylinder) has been inserted on the left hand side and no reference sample, but a reference plane (light green platelet) is present at the right hand side.

As illustrated in this figure, the laser beams could be made to be reflected directly by the sample surface and the reference plane. For practical reasons, however, silica rods of equal length are positioned above the sample and instead of the reference plane inside the second glass tube (not drawn here), which are vaporised with a reflecting nickel coating, where the laser beams get reflected.

In each case, temperature is measured by spot-welding thermocouples (type N) directly to

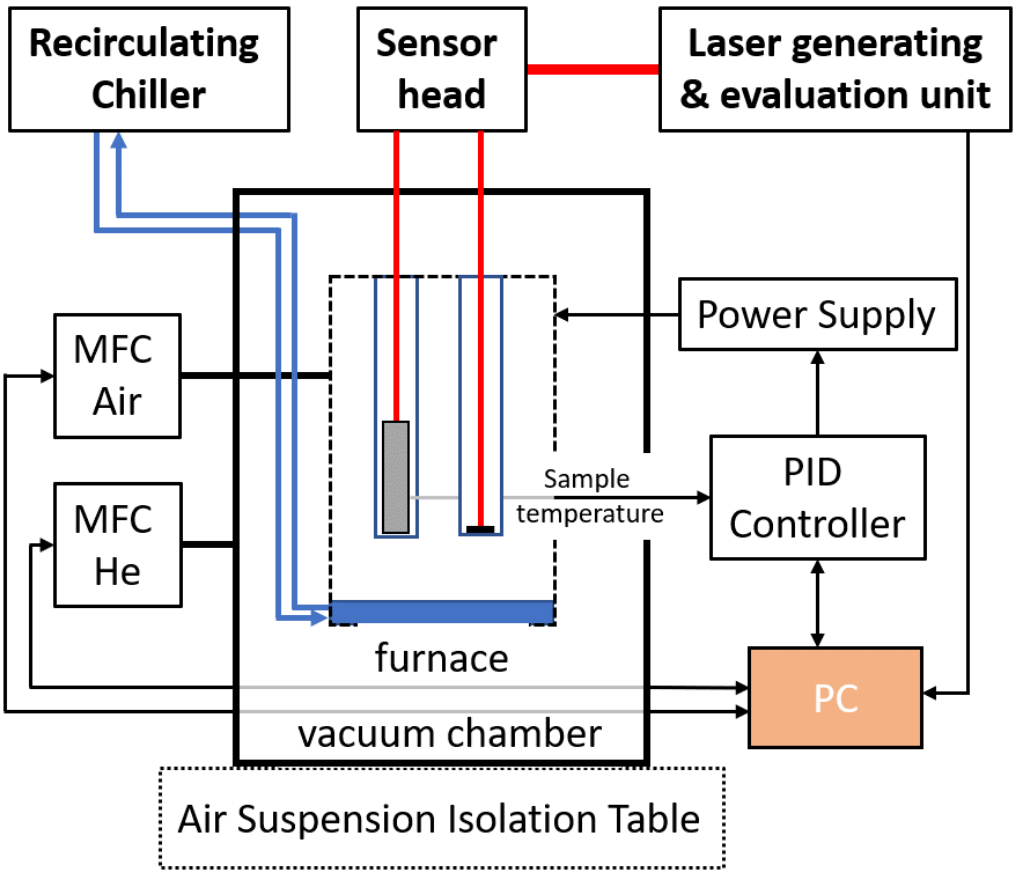

Figure 3.2: Functional block diagram of the dilatometer set-up with its main components and secondary devices.

the sample surface. The thermocouples are inserted from the outside via the third drill hole

of the sample holder inset and the little lateral hole in the glass tube. The temperature determined this way at the sample surface serves as input parameter for the PID controller which controls the lamp power via a feedback loop (see Fig.3.2). In this context, it should be mentioned that especially type N thermocouples are characterised by a low drift even over long measuring periods at high temperatures[37].

Thus, as another important element enabling the creation of precise temperature variations and a remarkably overall stability, the direct determination of temperature at the sample surface can be seen, which itself controls the power given to the samples. In many conventional dilatometers, temperature is not directly determined at the sample, but at certain distance to it.

Water-cooled base plate:

The middle part of the furnace with the reflecting walls at its inner side is made of aluminium which has been polished in order to obtain a high reflectivity for the light emitted from the halogen bulbs. In order to dissipate the heat which is injected into the reflecting walls owing to their non-ideal reflectivity, the mirror part of the furnace and the covering plate are pressed against a water cooled, copper bottom plate by adjusting screws (see Fig.3.1, copper base plate). During measuring, a continuous stream of water flows through the bottom plate which gets pressed into the circuit by a recirculating chiller (see Fig.3.2). This device measures the water temperature in the backflow line and sets the water temperature in the inflow line accordingly by using a PID-controller which is set to hold the bottom plate at a constant temperature of 20 °C, where the water temperature is measured with a precision of 0.1 °C. Cooling the base plate represents another important element which ensures the high stability of the dilatometer.

Length change measurements:

The length changes of the sample against a reference sample or of the sample against a reference plane are measured by a two-beam Michelson laser interferometer based on a SP120

DI (SIOS Messtechnik, Ilmenau, Germany) with a nominal resolution of 20 pm. The laser beam is generated by a He-Ne-tube in an external unit and is transferred via a single mode fibre-optic cable to the sensor head, where the beam is split into two individual beam lines (see Fig.3.2). Besides the optics for beam splitting, the sensor head contains two interferometer set-ups consisting of the usual birefringent prisms and sensors as well as of optics to properly focus the laser beams. The sensor head is mounted on a bridge made of stone, which can be moved its measuring position or away from it. In its measuring position, the sensor head is placed directly over the sealing cover plate of the vacuum chamber, which is a fast entry door equipped with a glass window, so that the laser beam can pass through it into the furnace.

Besides the usual isothermal and time-linear heating measurements which could also be conducted by using conventional dilatometers, the non-contact measuring method based on laser interferometry in combination with heating the sample by focused light results in a system with an exceptionally low inertia. This opens up the possibility for measurements featuring modulated temperature profiles with high modulation frequencies.

Correction and minimisation of environmental influences:

Several precautions have been taken in order to correct or minimise all kind of environmental influences on the measurements, thereby enabling in particular long-term measurements under isothermal conditions at unprecedented resolution. For this purpose, the whole dilatometer setting, i.e., the vacuum chamber with the furnace inside it together with the sensor head above, are mounted on a heavy stone plate which is carried by pneumatic springs. These springs together with the massive construction of the whole setting represent a most effective passive dampening system against all vibrations in the surroundings or of the floor (see Fig.3.2).

The mountings for the vacuum chamber as well as the movable bridge which carries the sensor head, are all made of large pieces of solid granite. Thus, being once at a certain temperature, it takes comparably long to change it and makes the system resistant against

short-term temperature variations. Additionally, the sensor head which may be subjected to short-term heat input due to its position directly above the furnace, is mounted on a plate made of Invar. Due to negligible heat expansion of this plate owing to the Invar effect, the position of the sensor head above the furnace and thus the points, where the laser beams hit the reflective Ni layers of the reflector rods, should not change, even during times of large/fast temperature changes.

Concerning the interferometric measurement principle, the length change measurements are directly influenced by the refractive index of the medium which has to be passed by the laser beams. Its refractive index is, amongst others, a function of its temperature, pressure and humidity. Thus, since there is a certain distance, which has to be passed by the laser beams through air on their way from the sensor head to the reflectors and back again, the so-called Edlén correction is applied[38,39]. In doing so, any influences, changes in the refractive index of air would have on the (long-term) stability of the device, are corrected. For this purpose, air temperature and humidity are determined by respective sensors.

3.2 Enhancements

As described in Sect.2.4, dilatometers are usually designed to perform measurements at the highest possible precision under certain circumstances, i.e., for instance, upon certain kinds of heat treatments. In this regard, the self-designed and -constructed laser dilatometer described in the previous section does not differ from other devices - various arrangements have been made in order to ensure the highest possible long-term stability under *isothermal conditions*. For the sake of clarity, a high long-term stability relates to a minimum drift, i.e., length changes over long time periods erroneously introduced by the device or external influences are small. Thereby, it is clear that a certain degree of interferences influencing the measurement signal is just natural. In the case of the present device, the mean drift has been determined to amount to less than 1.7 nm upon an isothermal heat treatment at 180 °C over a period of 48 h[26]. Since in the case of most specimen, the length changes appearing

upon comparable time periods are by far larger, such drift is uncritical.

When talking about isothermal measurements, heating or cooling to the respective temperature after arbitrary pretreatments is necessary, where especially the power required for heating naturally differs from that required for keeping the sample at constant temperature. As a consequence, heating power and thus sample temperature will be subjected to some kind of settling process right at the beginning of the isothermal treatment, the size of which mainly depends on how well the controller for the heating power is calibrated. In case of the present dilatometer, the sample temperature is settled quite fast, i.e., within seconds after any kind of pretreatment, owing to the low-inertia heating principle by focussed light (see Sect.3.1, "Mirror furnace").

In this context, the by far more critical parameter, applying also to the present device, is the extent of the transient response of the length changes coming along with this settling process of temperature. With respect to these length changes, this response may mainly be caused by the device itself and must not be directly related to temperature. Treatments prior to isothermal measurements are mostly used to create any kind of non-equilibrium state. Then, equilibrium is controllably established during the isothermal treatment, where this process is naturally fastest right at its beginning. Thus, since in the initial stage of the isothermal treatment, there just happens most, which makes this stage important, the transient response of the length changes in this stage should be as small as possible. Otherwise, the length resulting from the processes to be investigated are superimposed by the ones arising from the transient response, making either corrections necessary or, if not possible, initial data points have to be skipped. Accordingly, another objective is, to make the interferences caused by the settling processes in the beginning as small and short as possible.

The tool to find out about the size of the transient length change response are zero measurements which can also be used to correct the measurement signal. In the special case of the present dilatometer, the zero measurements recorded for low temperatures, i.e., the length changes measured without sample when heating in an arbitrary mode up to about 300 °C, vary in the range of several nanometres. Accordingly, a correction of the measurements is

not necessary in this case and also the data points right at the beginning can be used for analysis. On the contrary, when heating up to temperatures considerably above 300 °C, large length changes in the range of $\pm 1\mu$m and with alternating significant contributions appearing at time scales of several 10^4 s have been recorded, which are not acceptable. In this regard, Fig.3.3 shows an exemplary zero measurement (black curve) recorded right after heating to 800 °C, where the device had already been equipped with some improvements to reduce their size (see below).

Unfortunately, corrections by zero measurements do not appear really practicable in the present case for several reasons:

- If recording zero measurements without removing the sample holder from the device and reinstalling it afterwards, their repeatability is acceptable. Removing and reinstalling it, however, and possibly disassembling and assembling it or even replacing some components as would be done in the course of loading it with a sample, results in strongly different zero measurements. This also gives a hint about the necessity of reconsidering the sample holder design (see below).

- The zero measurements show long-term behaviour with large length changes occurring even at later times (see Fig.3.3). Additionally, the shape of the zero measurements varies with the heating rate applied and with the target temperature for isothermal ageing. Thus, measurements would be entailed with significant efforts, since for any single one, a zero measurement would have to be conducted first.

- The temperature distribution of the sealed fused silica tubes, where the sample is positioned for measuring purposes, and of the fused silica reflector rods on top of it, may strongly vary in case of a sample being present or not, since it may act like a hot plate. This may especially be problematic in the case of high temperatures, where the sample starts to emit radiation itself. Since the components made of fused silica are quite long, temperature differences of only a few degrees may cause noticeably different expansions despite the low expansion coefficient of fused silica. Additionally, since the

sample acts as a hot plate itself, the time spans to reach the equilibrium temperature may strongly vary. This means, the zero measurement without sample may even not be suitable to be used for correction.

Since conducting proper isothermal measurements at temperatures exceeding 300 °C is, however, indispensably important for a lot of alloy systems, the strategy has been, instead, to analyse the device with respect to potential causes of such zero measurements in order to minimise their size. The considerations made in this context and, based on them, the enhancements finely installed at the dilatometer, are described in the following.

In general, the more or less sudden appearance of such extensive transient responses of

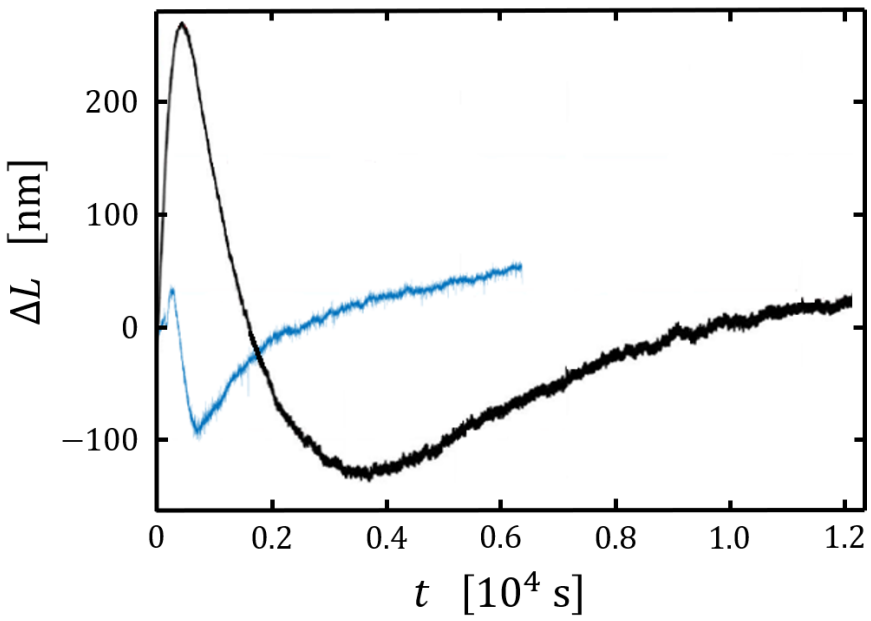

Figure 3.3: Exemplary zero measurement recorded during the isothermal treatment after heating the dilatometer in high vacuum to 800 °C with a heating rate of 100 °C min^{-1}. The black curve has been recorded after the dilatometer has been positioned inside a climate chamber. The blue curve has been recorded after equipping the device additionally with a water cooled recipient plate. For the measurements, a platelet was positioned on top of the sample holder inset, where the laser beams were reflected (see Fig.3.1).

the length changes for temperatures above 300 °C become comprehensible, when bearing in mind that the power consumption necessary to generate high sample temperatures does not increase linearly but rather exponential. The heating power required to keep the small

samples at constant temperature or to heat them up is minute, in particular, since they are positioned in high vacuum, so convection or notable heat conduction can be ruled out to contribute much. This means that a large amount of the power is introduced into several parts of the device other than the sample, which has to be dissipated.

In the following, the interferometric length change measurement is considered to work perfectly, i.e., it does not contribute to the zero measurements. In the light of the large amounts of heat, which have to be dissipated, when performing measurements at high ageing temperatures, the zero measurements could be explained by an uneven heat transfer to the various parts of the dilatometer. Such imbalance would lead to different expansions of the parts which either directly or indirectly influence the position of the two reflecting planes upon heating the device, and thus lead to zero measurements as the ones described above.

In order to test the influence of each single part of the dilatometer, a reflecting plate has been placed at different positions in the beam path. This is, for instance, the top of the sample holder inset (see Fig.3.1) or the the top of the fast entry door of the recipient (see Fig.3.4). In the following, based on multiple measurements, the considerations concerning the parts of the device, which turned out to be problematic with respect to an imbalance in the heat transfer, are given together with the countermeasures taken:

Climate chamber:

As described in Sect.3.1, the sensor head is mounted at the crossbar of a bridge made of solid stone, which can be moved for measuring purposes above the furnace part of the dilatometer. In its original state, the cooling air for the lamps was released right at the bottom side of the dilatometer (see Fig.3.4, fat red arrow). This represents a minor problem in case of isothermal measurements at low temperature, where the air gets not substantially heated over $T_{amb.}$. When performing measurements at high temperatures, however, the air may get heated to temperatures above 200 °C and its flow is notably increased. Thus large amounts of heat get placed at the bottom side of the dilatometer close to the two pillars carrying the bridge. Based on simple considerations, even minute temperature differences in between

both pillars do lead to uneven thermal expansion of both sides. Thus, the crossbar on top of the pillars and, together with it, the sensor head is tilted causing small but potentially notable contributions to the zero measurements.

As a countermeasure, plastic pipes have been installed, which channel the hot air away from the bottom side of the dilatometer. Since this system does not work perfectly, i.e., the interfaces in between the installed plastic pipes and the exhaust pipes of the dilatometers are leaky to a certain degree and the pipes get hot itself, the heat released at the bottom side may still lead to uneven expansions of the pillars. In addition to the heat produced at the bottom part of the dilatometer, there are some other parts of the dilatometer set-up, which heat up, especially in case of elevated sample temperature. In order prevent any unintended heat transfer to other parts of the dilatometer, the heat produced at any parts of the set-up has to be removed. For this purposes, since spray cooling has been found to be insufficient, the whole dilatometer set-up was placed within a climate chamber with a high air-throughput, which is able to remove the heat most effectively from the set-up. The zero measurement presented in Fig.3.3 has been recorded after the installation of this chamber, where the measurements recorded before showed an even worse behaviour, i.e., length changes larger in size and appearing on larger time scales.

Furnace and bottom plate:

With respect to the furnace, there exist several parts, which, when heat is transferred to them, may contribute notably to the zero measurements. First, the furnace walls are made of aluminium which has been polished at its inner surface to act as a mirror for the radiation emitted by the halogen bulbs. Due to the non-ideal reflection coefficient of aluminium, some part of the radiation is absorbed making the furnace walls to heat up, what has been proven by determining temperature at its top side during measurements. The temperature field generated by the halogen bulbs in their second focus points in the middle of the furnace is known to be inhomogeneous in between the different second focus points. This suggests, that heat is also introduced asymmetrically into the walls, leading to some parts of the furnace

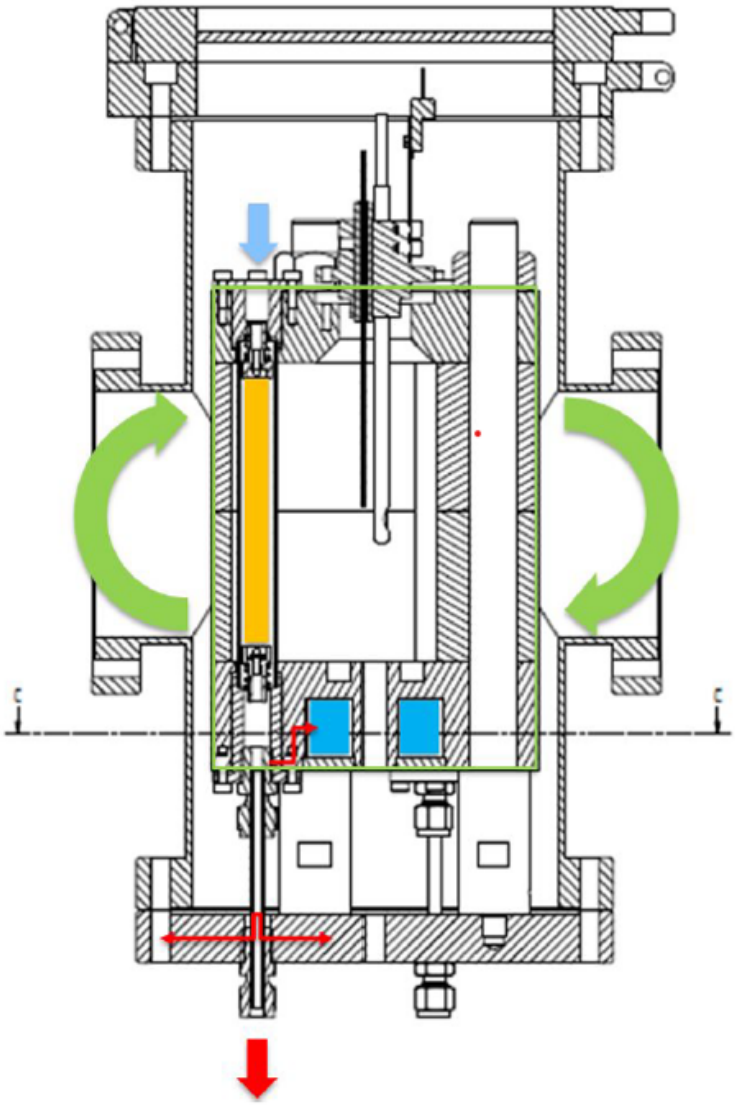

Figure 3.4: Furnace part of the dilatometer inside the recipient which gets evacuated for measuring purposes. The red thin arrows indicate the heat which is dissipated into the water cooled base plate of the furnace part and the recipient bottom plate. The red thick arrow marks the heat which is released at the bottom side of the dilatometer along with the cooling air flow. The green arrows indicate a possible tilt of the furnace part, which arises due to heat being asymmetrically transferred into the recipient bottom plate causing an imbalance in the thermal expansion of the pillars carrying the furnace part.

expanding more strongly than others. The effect of this asymmetrical heat transfer on the sample holder which is mounted inside the cover plate on top of the furnace, is described below.

Second, the furnace part consist of the cover plate with the sample holder inset, the reflecting

walls and the water-cooled bottom plate. The furnace part is mounted, as a whole, on three pillars positioned on the bottom plate of the recipient (see Fig.3.4). Especially in case of isothermal measurements at high temperatures, it has been found that this bottom plate heats up strongly. Assuming the heat transfer from this bottom plate to the three pillars to be only slightly asymmetrical, this is another mechanism, which is able to tilt the whole furnace as illustrated by the green arrows in Fig.3.4 and can thus significantly contribute to the zero measurements. Heating up of the bottom plate has been identified to be caused by the metallic exhaust pipes for the cooling air flow of the lamps being directly attached to the metallic bottom plate, admitting heat to be transferred the more or less unhindered into the plate (see Fig.3.4, red arrows). Since experiments of simply cooling the bottom plate in an air stream turned out to be successful with respect to minimising the size of the zero measurements, as a more permanent solution, the base plate of the recipient has been redesigned to be water-cooled. This results in notable minimisation of the size of the zero measurement in the range under 100 nm, which is a significant improvement (see Fig.3.3, blue curve).

Sample holder:

The sample holder is designed as an inset in the cover plate of the furnace. As described, sealed fused silica tubes are mounted inside it, which make the samples inside them to be positioned in the centre of the furnace (see Fig.3.1). Various zero measurements have been performed to test the effect, slight changes in the configurations of the sample holder will have on them. In doing so, the way, how the sealed fused silica tubes are attached to the sample holder has been changed and other diameters of the sample holding tubes have been used. In each case, the zero measurement seem to get influenced, but not in a decisive manner. So, the whole design of the sample holder has been scrutinised for possible other causes which show more notable contributions to the zero measurements.

As described, the fused silica tubes equipped with the reflecting rods, sample and reference sample are placed inside the inset which is placed in the covering plate right at the top of

furnace. Since the furnace is most probably expanding asymmetrically, the position right at the top is most inconvenient, because this way, the effect on the measurements, should be largest. Thus, several ideas have been developed for a completely redesigned sample holder, where the sample is not placed inside the fused silica tubes anymore. The redesigned sample holder is just about to be implemented.

To sum up, the dilatometer has been equipped with several enhancements, which all aim at a reduction of the zero measurements in size. This becomes necessary, since the zero measurements cannot be used to for correction of the measurements. The largest improvements have been obtained by installing a climate chamber surrounding the dilatometer, which allows to most effectively dissipate all the heat generated, and by redesigning the recipient bottom plate to be water-cooled. In a next step, the sample holder should get redesigned, where corresponding plans yet exist and are about to be implemented.

4 | Precipitate Formation Processes in an Al-Mg-Si-Alloy

Back in the year 1954, the annual production of primary aluminium surpassed for the first time that of copper, ousting it from its number one position as the most important non-ferrous metal[40]. Since then, the worldwide production of aluminium has increased strongly – in the last 30 years, in particular, it has *more than doubled* in each decade[1]. This information gives a hint of the great importance of aluminium or rather its alloys which are present today in almost every area of our modern-day life[4,41,42].

Their broad use mainly originates from the possibility to prepare alloys with a vast spectrum of properties by subjecting them to different kinds of thermal and/or mechanical treatments and by adding various kinds of alloying elements. In doing so, above all, strength values in the wide range of $70 - 800\,\mathrm{N/mm^2}$ ($\sim$ medium hard steels) are achievable combined with a low mass density ($\rho_{\mathrm{Al}} \sim 1/3\,\rho_{\mathrm{Fe}}$)[1].

Increased strength or hardness upon heat-treating some Al-alloys is found to be caused by the formation of precipitation phases. A textbook example of this class are Al-Cu-alloys, where the specifics of the precipitation phases appearing are well-known[43,44]. Another important example are Al-Mg-Si-alloys, to which the material investigated hereinafter belongs. Their precipitation sequence turns out to be more complex and is less well-examined. However, since being suitable for extrusion and lightweight engineering[45], the optimisation of existing thermal treatments to yield even better mechanical properties is a topic of ongoing interest.

4.1 Classification of Al-alloys, 6xxx Al-alloy group

Al-alloys are naturally categorised into classes according to their main alloying elements, the most important ones of which are Mg, Mn, Cu, Si, and Zn or combinations of these elements[1]. According to kind and concentration of alloying elements present, part of these alloys is suitable to be brought into its final shape by casting, where the other part is more favourable to be mould by forming processes. Correspondingly, the respective alloys are denoted as cast and wrought Al-alloys (AC and AW)[46,47]. In Fig.4.1, a categorisation of wrought aluminium alloys is made according to their main alloying elements (circles) and the predominant effect leading to hardness increases (red and blue box). If a notable hardening effect is found upon applying certain heat-treatments, Al-alloys are termed as heat-treatable/age-hardenable (see Fig.4.1, red box)[46]. Here, the formation of a finely distributed second phase is found to be responsible for major hardening effects. In case of non-heat-treatable alloys, the mere presence of alloying elements and increases in the dislocation density by forming processes in the cold state are the predominant strengthening mechanisms, which are referred to as solid solution hardening and strain hardening, respectively (see Fig.4.1, blue box)[48].

The alloy investigated hereinafter is denoted as "AW 6060 in T6 condition" (see Tab.4.1 for its composition). According to the descriptions above, this alloy evidently belongs to the group of wrought Al-alloys (AW), where the first digit of the following four ones, a 6, indicates that its main alloying elements are Mg and Si (see Fig.4.1, 6xxx-alloy group, filled green circle). For this alloy class, the second digit is always zero. The third and fourth digit provides information about the compositional range of both, main and minor alloying elements.[1] AW 6060 is heat-treatable. Being "in T6 condition" means, the material has been subjected to a special kind of heat treatment in order to obtain maximum hardness prior to delivery.

[1]Note: The designation of the aluminium alloy investigated has been chosen according to the DIN standard EN 573 for wrought aluminium alloys. There are, however, other designation systems in use across the world.

In general, Al-Mg-Si-alloys are known to possess medium to high strength, to be most suitable for extrusion, as mentioned, and to be easily heat-treated. They are used for a broad

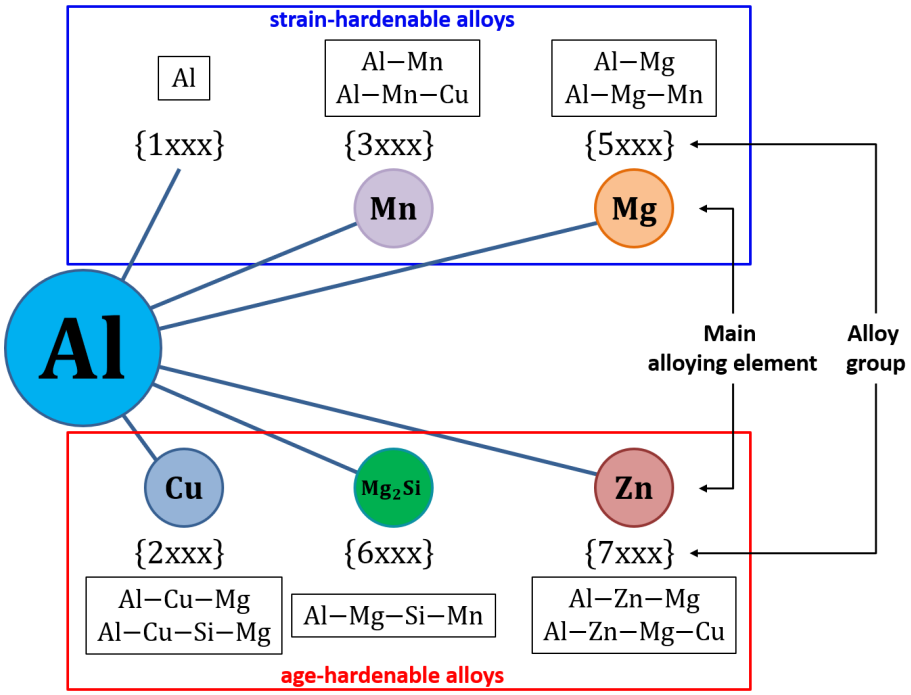

Figure 4.1: Classes of wrought aluminium alloys. A first categorisation has been made according to the main alloying elements (circles/numbers beneath or above). Additionally, the most important representatives of the respective alloy groups are listed with their composition with respect to most important other alloying elements (boxes framed in black). A further categorisation has been made according to the fact whether the alloys are strain-hardenable or age-hardenable (blue and red box).[2]

range of applications as, for instance, in the automotive industry for profiles and exterior parts, for railcars or doors and window frames to name just a few[1,47,48]. In Fig.4.1, the composition of these alloys with respect to Mg and Si is denoted as Mg_2Si (filled green circle). This does not mean that Mg and Si are always added in exactly this proportion, but alludes to the composition of the precipitate phase formed in equilibrium. Correspondingly, alloys with a proportion of $Mg/Si = 2$ are denoted as balanced and alloys with $Mg/Si < 2$ and $Mg/Si > 2$ as "excess Si" and "excess Mg", respectively[1].

[2]This figure has been created based on a similar one from section 3.2.1 of the *The Aluminium Automotive Manual* (version 2002) of the European Aluminium Association[49]

4.2 State of research: precipitation sequence in Al-Mg-Si-alloys

By applying specially designed heat treatments to Al-Mg-Si-samples, large hardness increases can be achieved, which originate from thermally activated, diffusion-controlled formation processes of precipitation phases. In general, preconditions for precipitate formation are a large solubility of the alloying elements at elevated temperatures and a strongly reduced one at low temperatures, thereby making the formation of a second phase energetically favourable.

Accordingly, samples are first solution annealed at elevated temperatures, where already existing precipitates get dissolved, i.e., Mg- and Si-atoms get statistically distributed in substitutional manner over the Al-lattice, and are now present in *solid solution*. Upon quenching, this configuration is retained, but in unstable state, which is termed as *super-saturated solid solution* (SSSS). Owing to the strongly reduced solubility for Mg and Si at low temperatures, precipitate formation starts during the subsequent ageing sequence. The quenching rates necessary for the alloying elements to remain in SSSS are mainly determined by the kind(s) of major alloying element(s) and especially by the presence of certain minor alloying elements as Cr, Mn, or Cu, which are known to drastically increase the required quenching rates since they provide favourable sites for the phase formation to start [1].[3]

After quenching, ageing may entirely be performed at temperatures around $T_{amb.}$, which is called "natural ageing" (NA), or at elevated temperatures, commonly in the range of $160 - 210\,°C$, which is called "artificial ageing" (AA), eventually in combination with each other or with a short period of ageing at intermediate temperatures in the range of $80 - 100\,°C$, which is called "pre-ageing" (PA). In doing so, at least if not applying ageing temperatures larger than approximately $300\,°C$, not the equilibrium precipitation phase called β (compo-

[3] In case of AW 6060, quenching rates of $50\,°C min^{-1}$ or lower (depending on the exact ratio of Mg and Si) are known to be required in order to keep Mg and Si in SSSS. In case of e.g. AW 6082, an alloy with a slightly higher Mg and Si-contents and, especially, Mn-additions, the required quenching rates are more than 160 times higher [50].

sition: Mg_2Si) is formed, since its immediate formation is energetically unfavourable, but metastable intermediate phases according to the precipitation sequence:

$$\text{SSSS} \longrightarrow \text{clustering, pre-}\beta'' \longrightarrow \beta'' \longrightarrow \beta'/\text{U}_1/\text{U}_2/\text{B}' \longrightarrow \beta. \tag{4.1}$$

Upon ageing at elevated temperatures, some of the initial phases may be skipped. Analogously, at low temperatures, the precipitation sequence may get effectively stuck after the formation of a certain metastable phase[51].

The most important parameters which influence the hardness response due to precipitate formation, are their size and distribution as well the kind of interface of the precipitates with the surrounding matrix[52]. In general, the more close the precipitation phases reach to the equilibrium β-phase, the more incoherent they become with the surrounding matrix, the more their Al-content is reduced with their concentration approaching Mg_2Si, and the larger they become. In order to obtain large hardness increases, AA at temperatures in the range of $160 - 185\,°C$ is applied eventually in combination with some NA time interval after quenching. Here, preceding NA is known to either enhance or diminish the maximum hardness values achievable[53].

With a view to the precipitation sequence, it must be mentioned that the characteristics of its individual phases as well as the sequence as a whole are still under discussion, varying mainly along with the kind of heat treatment applied and depending on the exact alloy composition[54]. The precipitation sequence, as shown in Eq.4.1, is the result of a literature survey of existing studies, which deal with alloys of similar compositions to that of the investigated sample. Since relevant for understanding the publications included in this chapter, the precipitation phases appearing in Al-Mg-Si-alloys are described in the following in detail.

Clustering-phases/pre-β''-phase:

Clusters do appear as a first precipitation stage right after quenching, independent of the further steps of the heat treatment. They are described as agglomerates which are found

to exist on the fcc Al-lattice, consisting mainly of either Mg- or Si-atoms or of both kinds of atoms (co-clusters) and of large fractions of Al-atoms[55–57]. Today, it is assumed that there are at least two clustering stages. At first, Mg- and/or Si-rich clusters form primarily depending on the overall alloy composition (balance, Si-excess, Mg-excess) and on the first stages of the heat treatment. Subsequently, these clusters grow into co-clusters. Due to their minute size and their large coherency with the surrounding Al-lattice as well as due to the absence of an ordered arrangement of the different kinds of atoms contained in those clusters, only the most sensitive measurement techniques as PALS, HAADF-STEM and APT combined with simulations are suitable to investigate them[55,58,59].

In this context, pre-β'' is described by some authors as just another clustering phase which still shows fcc-lattice structure, but with the alloying element atoms being being arranged in an ordered structure[56,57].[4] For these pre-β''-clusters, a wide range of compositions is discussed, where only some of them may represent suitable precursors for the following β''-phase and the other ones most likely dissolve during the following stages of the precipitation sequence[60].

Despite their minute size and short time scales of existence, in general, clusters formed during some time at $T_{amb.}$ right after quenching are known to notably influence the subsequent precipitate phases[61,62]. Note, that this is just one example of the great influence, clustering phases may have on subsequent precipitation phases.

β''-phase:

The needle-shaped β''-precipitates are oriented along $\langle 100 \rangle_{\mathrm{Al}}$-direction with a typically size of $4 \times 4 \times 50\,\mathrm{nm}^3$ and represent the first precipitation phase which shows a lattice structure deviating from the fcc Al-lattice, with a clearly defined arrangement of Si-, Mg- and Al-atoms inside them[63,64]. Due to large coherency strains accompanying these precipitates, which are still coherent with the surrounding matrix, they are easily detected by high-resolution

[4]Note: The way of dividing the clustering phases as presented here is not the only one possible. In fact, there is no generally recognised way of designating the individual clustering stages, mainly due to the uncertainty about the factors influencing their appearance and constitution

TEM and XRD[63,65]. Despite this, there existed controversies for several decades about their structure as well as composition. Here, especially the Al-content of the β''-particles has been under discussion. Today, for samples with a composition close to that of the alloy investigated hereinafter (see Tab.4.1), monoclinic crystal structure with a composition of $Mg_4Al_3Si_4$ is widely accepted[59,66].

The presence of β''-precipitates, possibly in combination with some small fraction of the preceding clustering phases, is known to cause the largest hardness increases with respect to the SSSS-state[64]. Maximum hardness values corresponding to a proper size and distribution of those precipitates are obtained by AA at a standard temperature of 175 °C for a certain time interval, eventually in combination with some preceding NA time interval (peak-aged conditions)[64].

When performing long-term NA, only moderate increases in hardness are achieved. Here, "β''-like" precipitates are known to be formed over very long periods of time, which are rather spherical than needle-shaped, and the precipitation sequence is known to effectively stop after their formation[67]. Correspondingly, after having achieved peak-hardness conditions by AA at 175 °C, the precipitate structure is metastable, but does not change substantially upon quenching to $T_{amb.}$ within time-scales accessible.

β'/U1/U2/B$'$-phase:

Up till today, it is not entirely clear, whether the formation of the phases belonging to this precipitation stage occurs simultaneously to the formation of β''-precipitates, but in slower mode, or whether they are arising by transformation of β''-precipitates[68]. Similarities in between needle-shaped β''- and at least β'-precipitates which are in general described as larger versions of β''-precipitates, i.e., as columns or rods, may give a hint, however, of a transformation mechanism[69].

Similar to the clustering phases, β'-, U1, U2 or B$'$-precipitates or combinations of these kinds of precipitates may be found depending on the heat treatment, the overall alloy composition as well as on the presence of certain minor alloying elements[70]. In case of the alloy investi-

gated hereinafter, mainly β'-precipitates are found to be formed during AA[71].

Due to their increased size with respect to β''-precipitates and also due to large coherency strains with the surrounding Al-matrix – β'-precipitates are described as semi-coherent – they are easily investigated. β'-precipitates show hexagonal crystal structure and a composition of Mg_9Si_5 with no Al-atoms being found inside them, which is already close to the composition of the equilibrium β-phase (Mg_2Si)[69]. In general, the formation of large proportions of β'-precipitates is avoided in the course of AA because of the negative influence on hardness (over-ageing).

β-phase:

Finally, as a last step of the precipitation sequence, the equilibrium β-phase is formed. Here again, it is not entirely clear, whether this occurs via direct transformation of β'-phase particles or by their dissolution accompanied by the nucleation of β-phase precipitates[72]. As in the case of β''-precipitates, there are no Al-atoms contained inside them. Their composition amounts to Mg_2Si arranged in Ca_2F-lattice structure (fcc)[65,73]. β-phase precipitates are found to be present as comparably large platelets which are incoherent to the surrounding matrix, and thus require high amounts of energy to be formed. Consequently, their formation is not observed for low temperatures, i.e., substantially lower than 300 °C[71,74].

4.3 Motivation

Precipitation phase formation in Al-alloys is a complex topic, since it often occurs by running through several stages. In this context, in particular the precipitates formed during the first stages are usually quite hard to investigate. This is, on the one hand, due to their minute size with large fractions of Al-atoms inside them, which makes their distinction from the surrounding matrix a challenging task, and, on the other hand, due to the initially fast kinetics which often make several precipitation stages overlap. As a consequence, precipitate

lattice structures and compositions are often not exactly known.

Concerning dilatometry, the formation of each precipitation phase results in either positive or negative sample length changes of certain value per unit phase fraction[13,75]. Together with mathematical models which establish the connection of the sample length changes to the changes caused by precipitate formation on the microscopic scale, dilatometry can thus severe as a most valuable tool to identify the formation of certain kinds of precipitates and to decide, moreover, over their composition and lattice structure.

Hence, the first publication included in this work (out of two, see Sect.4.2, Article 1) aimed at ...

- ... developing quantitative models which allow to calculate the length changes to be expected upon the formation of a variable amount of the different precipitation phases appearing in AW 6060 based on information about their lattice structure and composition.

- ... aiding, in return, the identification of the most probable composition and lattice structures of the precipitation phases based on the measured length changes and in agreement with the results obtained by other techniques.

Assume now two precipitation phases, appearing either successively or in parallel, which cause length changes of opposite sign and of strongly different value. Due to (partial) compensation of the length changes coming along with the formation of these two phases, peak heights, onset and endpoints appear distorted, which complicates the interpretation of dilatometry measurements.

This specific situation is encountered in the course of β''- and β'-precipitation phase formation in AW 6060. In order to accurately identify the individual contributions of each phase to the overall length change nevertheless, kinetic modelling based on the length change models obtained in the course of the first publication is required.

Thus, the second publication included in this work (see Sect.4.2, Article 2) aimed at ...

- ... finding an adequate kinetic model for β''-precipitate formation and either the parallel formation or its transformation to the β'-phase. In this context, "adequate" refers to good fitting results and reasonable interpretability of the parameters of the model.
- ... determining the temperature depending rates for β''-formation and its transformation to β' as well as creating the isothermal TTT-diagram and calculating the corresponding activation energies for both processes based on these rates.

4.4 Experimental

The Al-alloy investigated belong to the class of heat-treatable Al-Mg-Si-alloys (6xxx-group), where the base material is designated as AW 6060, meaning, it possesses a nominal composition of $0.30 - 0.6\,\mathrm{wt\%}\,\mathrm{Si}$ and $0.35 - 0.6\,\mathrm{wt\%}\,\mathrm{Mg}$. Samples have been cut from a square AW 6060-rod and twisted off to obtain cylindrical shape featuring a length of 20 mm and a diameter of 5.65 mm. The material has been analysed with respect to its exact composition by OES (Optical Emission Spectroscopy) yielding the values which are listed in Tab.4.1 in wt% as well as at%[5]. According to the composition given in at% in this table (second column), the material must be denoted as "excess-Si", since, with respect to the composition of the equilibrium β-precipitation phase (Mg_2Si), it contains too much Si. This statement is also valid after subtracting the Si-amount which is bound inside primary Fe-rich precipitates[76]. In order to receive length change contributions exclusively from precipitate formation processes, but not from other microstructural changes occurring, as for instance from grain growth, the samples have been solution annealed for approximately 48 h under Ar-atmosphere at atmospheric pressure at a temperature of 540 °C after their preparation. The heat treatment subsequently applied to the samples has been chosen according to the ones commonly performed in industry to achieve maximum hardness. It is shown in Fig.4.2. Solution annealing has been conducted till the sample length does not change anymore. Since

[5]The exact composition of the AW 6060-samples investigated has been determined at the Institute of Nonferrous Metallurgy at the University of Leoben by Prof. Pogatscher and co-workers.

Table 4.1: Composition of the AW 6060-samples investigated in this work given in wt% and at%.

element	wt %	at %
Al	balance	
Mg	0.5790 ± 0.0060	0.6430 ± 0.0060
Si	0.5360 ± 0.0070	0.5160 ± 0.0070
Fe	0.2250 ± 0.0020	0.1090 ± 0.0010
Cu	0.0020 ± 0.0010	0.0010 ± 0.0003
Mn	0.0048 ± 0.0001	0.0024 ± 0.0001
Ti	0.0114 ± 0.0005	0.0064 ± 0.0002
Zn	0.0045 ± 0.0018	0.0019 ± 0.0007

length changes at these temperatures originate from precipitate dissolution, this indicates that all dissolution processes have come to an end. After solution annealing, quenching to $T_{amb.}$ has been performed in an He-gas stream. Subsequently, the samples have been aged for a short period of 4 min at 30 °C and fast heated to ageing temperatures ranging from $170 - 360$ °C (see Fig.4.2, green-coloured box), where they have been isothermally aged for

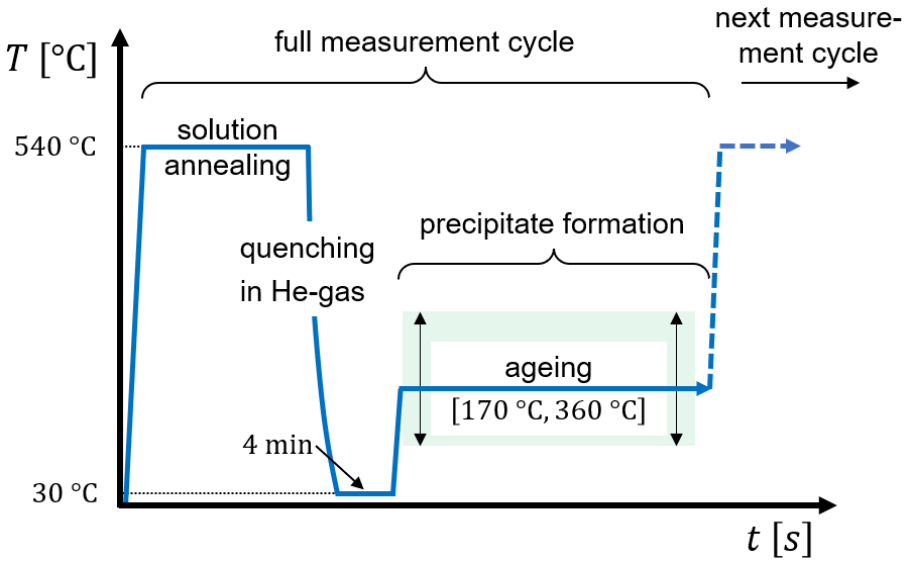

Figure 4.2: Heat treatment applied to the samples consisting of solution annealing, quenching to 30 °C, holding at this temperature for 4 min, heating to ageing temperatures ranging from 170 °C to 360 °C and ageing for various time periods. If ageing is finished, another measurement sequence is started by heating the sample again to solution annealing temperatures.

variable periods of time. In order to make sure that no irreversible processes, but only precipitate formation takes place during ageing, the measurement at the ageing temperature of 180 °C has been repeated approximately after every third measurement at arbitrary ageing temperatures and the congruency with the preceding measurements at this temperature was checked. The full heat treatment has been performed *in situ*.

As a supportive technique, indentation hardness measurements have been performed exclusively for the ageing temperature of 180 °C after various time intervals of ageing. They were carried out with an EMCOTEST DuraJet measuring device according to Brinell method with a 2.5 mm spherical indenter under 31.25 kp load.

In order to calculate the unit cell volumina of the precipitation phases appearing based on information about lattice structures and compositions, as required for the first publication (see Sect.4.2, Article 1), the visualisation programme VESTA (Visualization for Electronic and STructural Analysis) by Momma and Izumi has been used[77].

Kinetic modelling and thus curve fitting of the measurements obtained, as done for the second publication (see Sect.4.2, Article 2), has been performed by using the MatLab-routine "nlinfit".

4.5 Publications

Two peer-reviewed published articles have been included in this work in the following, which constitute the main part of this chapter. They deal with the creation of a complete kinetic model concerning the precipitation phase formation processes taking place in AW 6060-samples upon isothermal AA after solution annealing and quenching.
Hereto belongs first a model which establishes the connection in between the length changes appearing and the formation of certain fractions of precipitate phases (see Sect.4.5.1). Second, by applying an adequate kinetic model for the phase formation and transformation processes in question taking place, the evolution of the corresponding phase fractions can be used in order to determine temperature dependent formation/transformation rates, to prepare TTT-diagrams and to calculate formation energies (see Sect.4.5.2).

In article 1 (Sect.4.5.1,[12]), a model is introduced which allows to calculate the length changes caused by the formation of precipitation phases in AW 6060 based on information about their respective lattice structures and compositions. The results of a broad literature survey concerning these quantities are presented and the corresponding length changes calculated by assuming the largest possible fraction of these phases to precipitate. The length changes for mere β''-, β', and β-precipitate formation are calculated these way are compared in the following to the measured length changes at ageing temperatures, where a maximum amount of the respective phases is known to be formed. Furthermore, considerations concerning the potential influence of excess volume on the length changes calculated coming along with the interfaces in between the precipitates and the surrounding matrix are discussed.

Article 2 (Sect.4.5.2,[33]) deals with the creation of a kinetic model for the temperature range, where the formation of β''- and β'-precipitation phases is observed, i.e., in between

180 °C and 260 °C. A model in the framework of simple exponential functions has been found to provide the best fitting results. The calculated length changes for a maximum content of both phases being formed as described in article 1 are used as amplitude factors in the kinetic model. By applying the model developed to the measured data, β''-phase and β'-precipitate formation rates could be determined. On their basis, furthermore, the isothermal TTT-diagram for the respective temperature range could be created and the formation energies of both phases be calculated.

4.5.1 Article 1: Identification of precipitation phases in AW 6060 by quantitative volumetric estimations

Preamble: The article "*Quantitative volumetric identification of precipitates in dilute alloys using high-precision isothermal dilatometry*" was published in Philosophical Magazine Letters **98** (301-309), October 2018[12].

The quantitative model presented in this work allows to understand the length changes measured by dilatometry as being caused as combined effect of a precipitation phases forming and concomitant changes in the surrounding matrix. It has been developed by the author in collaboration with Elisabeth Hengge and Martin Luckabauer. All dilatometry measurements have been performed by the author supported by Elisabeth Hengge (diploma student). A very detailed literature survey concerning the kind of phases appearing upon ageing at various temperatures, their composition as well as lattice structure has been prepared by Elisabeth Hengge together with the author. The calculations using both quantities in order to estimate the length changes to be expected upon the formation of the various precipitation phases have been performed by Elisabeth Hengge. The manuscript has been written by Roland Würschum in collaboration with Elisabeth Hengge and the author and was reviewed by Wolfgang Sprengel and Martin Luckabauer.

All measurements have been performed *in situ* in the self-developed and -constructed dilatometer described in Sect.3.1. This dilatometer is characterised by unprecedented sensitivity and stability. In this context, it must be emphasised that the length changes measured upon isothermal ageing, which have to be ascribed to precipitation phases, have sometimes been in the range up to only 50 nm. Such tiny length changes are to be expected for the alloy investigated, since it is a rather dilute one. Most commercially available dilatometers, however, are normally not able to even detect length changes of this order of magnitude. Furthermore, keeping the ambient conditions (mainly temperature) sufficiently constant throughout the longest time scales of ageing, i.e., for more than 10^6 s ($\sim$ 11.5 d) as necessary in case of NA (not shown in this article), is not an easy task, too.

PHILOSOPHICAL MAGAZINE LETTERS
2018, VOL. 98, NO. 7, 301–309
https://doi.org/10.1080/09500839.2018.1542170

Taylor & Francis
Taylor & Francis Group

Quantitative volumetric identification of precipitates in dilute alloys using high-precision isothermal dilatometry

E. Hengge, R. Enzinger, M. Luckabauer*, W. Sprengel and R. Würschum

Institute of Materials Physics, Graz University of Technology, Graz, Austria

ABSTRACT

The present case study demonstrates that high-precision dilatometry serves as sensitive tool for quantitatively characterising precipitation processes down to small relative length changes in the range of 10^{-5} and covering long time scales exceeding 10^5 s. For a dilute Al-based Al–Mg–Si alloy, the amount of the metastable coherent β''-phase and the semicoherent β'-phase as well as of the stable β-phase could be determined on an absolute scale from in-situ relative length change measurements upon long-time isothermal annealing. The quantitative analysis allows an assessment on the various contributions of the length change, i.e. the volume excess of the precipitates, the volume change of the matrix upon precipitation of solute atoms, and the length change due to the formation of interfaces.

ARTICLE HISTORY
Received 9 May 2018
Accepted 25 October 2018

KEYWORDS
Dilatometry; precipitation; alloys; thermal analysis

Studying precipitation phenomena in alloys experimentally on a quantitative scale is a challenging task. Among the techniques of thermal analyses, dilatometry, which measures length changes on an absolute scale, has turned out to be suitable for monitoring transformation processes in alloys [1–6]. Compared to differential scanning calorimetry, dilatometry is also sensitive under isothermal conditions [1,2,7,8] which is favourable compared to non-isothermal ones due to the more direct access to the underlying kinetics. Regarding resistometry, which is also suitable for long-term isothermal studies (e.g. ref. [9]), dilatometry is structurally more specific. However, dilatometry has so far been scarcely applied to derive quantitative information on the amount, e.g. the volume fraction, of precipitates. If at all, such studies have been restricted to alloy systems where the transformation is associated with volume changes in the range of at least several 10^{-4} and where the heating conditions are chosen that the transformation occurs on a time scale of minutes [3]. Therefore, precipitation processes in dilute alloys, such as aluminium alloys of the 6xxx series with low amounts of Mg and Si, up to now have been considered to be inaccessible by

CONTACT R. Würschum wuerschum@tugraz.at Institute of Materials Physics, Graz University of Technology, Petersgasse 16, 8010 Graz, Austria
*Present address: Institute of Materials Research, Tohoku University, 2-1-1 Katahira, Sendai 980-8577, Japan

dilatometry owing to the minor volume changes upon precipitation [5]. This pertains even more to long processing times exceeding 10^4 s which are of practical interest. Just the understanding of the precipitation processes occurring in these types of alloys on long time scales is of upmost importance due to their high technological relevance and due to the high complexity of the precipitation processes involving metastable phases.

Recently, a high-stability non-contact dilatometer based on 2-beam Michelson interferometry was developed that enables isothermal measurements of relative length change measurements in the sub-10^{-5} regime with minimised drift over times as long as 10^6 s [10]. This advanced technique is applied in the present work to quantitatively study precipitation phenomena which are associated with tiny relative length changes which have not been accessible before. In order to demonstrate the potentials of this technique for assessing application-relevant issues, commercial grade Al–Mg–Si alloy (EN AW-6060) is used. From the dilatometric measurements upon isothermal heat treatment at slightly elevated temperatures (so-called ageing), the quantitative amount of various metastable phases, which are formed on long time scales of $>10^4$ s, could be determined. Preliminar measuring results without any quantitative analysis have been communicated recently in a conference contribution [11].

The measurements were performed in a self-developed, high-stability laser dilatometer, the design and operation of which is described in detail elsewhere [10]. Chemical analysis of the EN AW-6060 Al–Mg–Si alloy by means of optical emission spectroscopy revealed a Mg- and Si-content of 0.65 at.% and 0.52 at.%, respectively, with additional traces of primarily Fe (0.11 at.%). For the dilatometric measurements cylindrical-shaped samples with a length of 20 mm and a diameter of 5.7 mm were used. Solution annealing was performed in the dilatometer at 540°C for 30 min with subsequent quenching down to 32°C in a helium gas stream with a rate sufficiently high for achieving a supersaturated solid solution [12]. After keeping the sample for 4 min at this temperature, heating up to the temperature of isothermal precipitation treatment between 170°C and 260°C was performed with a rate of 100°C/min. As onset for the isothermal length change measurements the time was chosen when the temperature approached the final temperature by ± 0.01°C; the dead time up to the onset is in the range of 100 s. The temperature was measured by means of Nicrosil-Nisil thermocouple directly welded to the sample under Ar atmosphere. Prior to the experiments, the sample was annealed at 540°C for 24 hours to obtain a fully recrystallised microstructure in order to exclude any influence of grain boundaries on the length change measurements. For comparison with precipation studies in literature, standard characterisation of the progress of precipation by means of hardness measurements was performed, applying the Brinell method with a hardness tester (type EMCO-TEST DuraJet).

Figure 1a shows the relative length change $\Delta L/L$ in dependence of time t measured at various annealing temperatures. Exemplarily, from seven

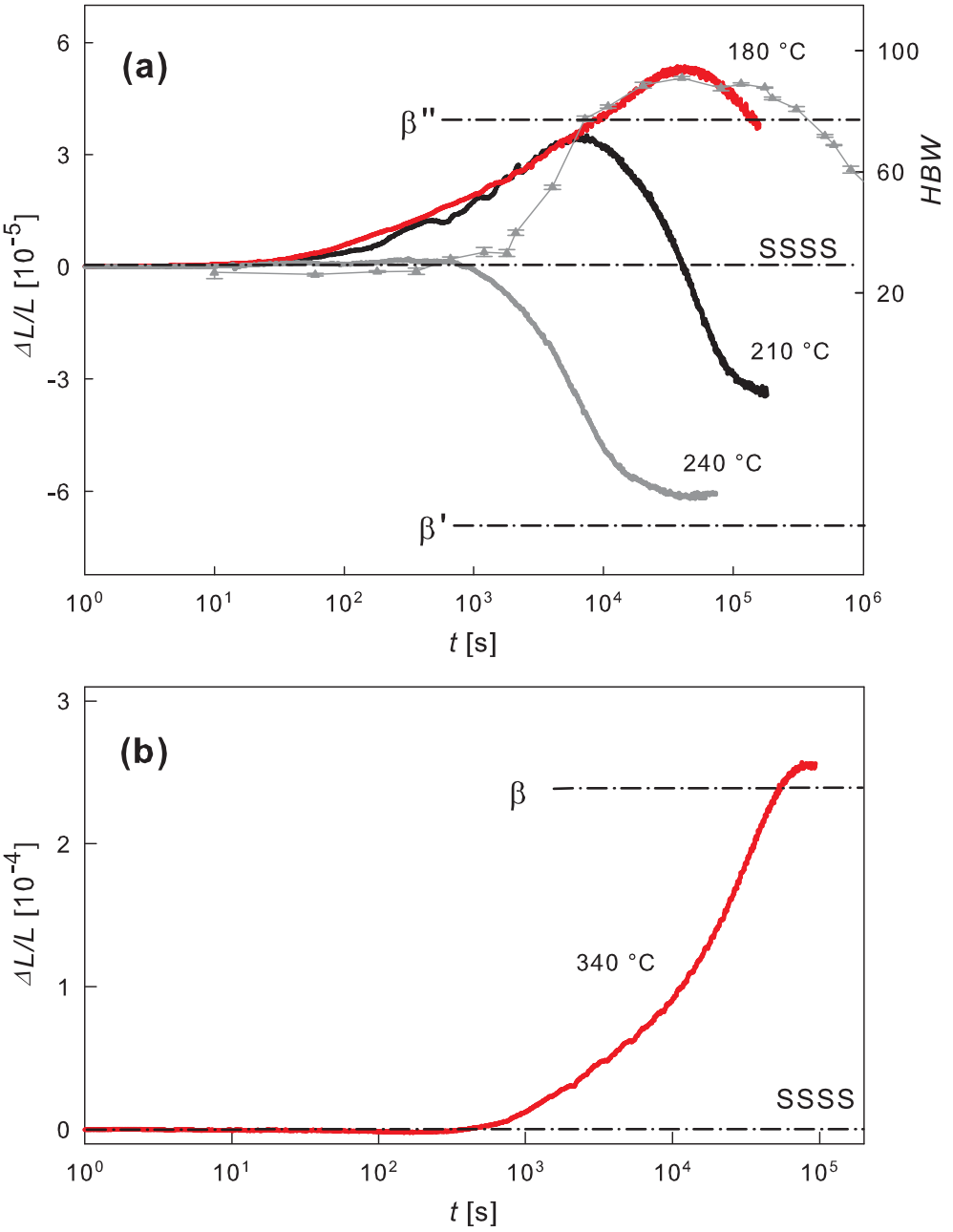

Figure 1. Relative length change $\Delta L/L$ in dependence of time t measured at the annealing temperatures of (a) 180°C, 210°C, 240°C, and (b) 340°C. The horizontal lines mark the quantitatively estimated length changes arising from formation of (a) β'', β', and (b) β; the line SSSS refers to the initial state of supersaturated solid solution (see discussion). (a) Corresponding Brinell hardness *HBW* measured upon ex-situ annealing at 180°C (▲, right-scale axis).

different temperatures, the curves are shown for 180°C, 210°C, and 240°C. For 180°C and 210°C, the relative length first increases in the range of several 10^{-5} and subsequently decreases. With decreasing temperature, the length maximum is shifted to longer times. For 240°C only a tiny length increase occurs prior to the decrease which in the measuring time of 7.3×10^4 s reaches a minimum

value of $\Delta L/L \simeq -6.1 \times 10^{-4}$ related to the starting value. For 210°C, approximately the same $\Delta L/L$-decrease is deduced with respect to the relative length maximum. For 180°C, the $\Delta L/L$-minimum is not reached during the time span of the measurement. The $\Delta L/L - t$-curves are highly reproducible as evidenced by multiple repetitions of the measuring sequence comprising solution treatment, quenching, and annealing. The Brinell hardness *HBW* exhibits a maximum for pretty the same annealing time as that of $\Delta L/L$ (Figure 1a).

The Al–Si–Mg alloy was chosen for the present study not least because the precipitation sequence of this alloy has been subject of comprehensive research before, so that the potentials of our new experimental approach can be easily assessed by means of comparison with available literature. A review of the complex precipitation sequence is, for instance, given by Ravi and Wolverton [13]. Briefly speaking, the precipitation sequence prior to the formation of the equilibrium Mg_2Si β-phase is governed by the metastable coherent phase β'' and the semicoherent phase β'. The hardness increase is considered to be due to the β''-phase which prevails in the hardness maximum [14]. Scanning transmission electron microscopy in combination with ab-initio calculations suggest that β'' is best described by monoclinic $Mg_4Al_3Si_4$ [15, 16]. In the so-called overageing regime, prior to the equilibrium phase, the metastable phase β' is reported as the predominant phase [17] consisting of hexagonal Mg_9Si_5 [18].

Based on the precipitation sequence described in the previous paragraph, the observed length change will at first be discussed qualitatively and subsequently be analysed quantitatively. Since the length variation with annealing time reflects the hardness behaviour, the length increase has to be attributed to the formation of coherent β''-phase and the length decrease to the formation of the semicoherent β'-phase. With increasing temperature the β'-formation and, therefore, the length decrease sets in earlier, so that the maximum length increase associated with β'' is reduced (compare 180°C and 210°C in Figure 1a) or is even nearly suppressed (240°C). The direct formation of the equilibrium β-phase fcc-Mg_2Si [19] could be monitored upon annealing at 340°C for 10^5 s leading to a relative length increase of $\Delta L/L \simeq 2.6 \times 10^{-4}$ (Figure 1b).

For the quantitative analysis, we adopt the simple picture that in the $\Delta L/L$-maximum at 180°C exclusively the β''-phase and in the $\Delta L/L$-minimum at 210°C or 240°C exclusively the β'-phase is present. The maximum amount of β'' of type $Mg_4Al_3Si_4$ is determined by the minor component of Mg and Si in the matrix, i.e. by the Si-content. Here, it has to be taken into consideration that the low amount of Fe-impurity (0.11 at.%) permanently binds an equal amount of Si, since Fe is known to form an intermetallic phase $Al_{14}Fe_3Si_3$ which is stable once it has been formed during both solution annealing and subsequent ageing. This yields a remaining amount of Si of 0.41 at.% for the formation of $Mg_4Al_3Si_4$ precipitates, or an equivalent total atomic fraction $f_{\beta''}$ of 0.0113. The relative length change associated with the

β''-phase is given by

$$\left.\frac{\Delta L}{L}\right|_{\text{prec}} = \frac{1}{3} \times \frac{\Delta v}{v}|_{\text{prec}} \times f_{\text{prec}}, \tag{1}$$

where

$$\left.\frac{\Delta v}{v}\right|_{\text{prec}} = \frac{\frac{n_{\text{ssss}}}{n_{\text{prec}}} v_{\text{prec}} - v_{\text{ssss}}}{v_{\text{ssss}}} \tag{2}$$

denotes the difference in the atomic volume between the precipitate and the supersaturated solid solution. In Equation (2), $v_{\text{prec/ssss}}$ and $n_{\text{prec/ssss}}$ represent the volume of the unit cell and the number of atoms per unit cell, respectively, for the precipitate (here, the β''-phase) and the supersaturated solid solution (SSSS). In Equation (1) ΔL is normalised to the length L. For the total relative length change

$$\left.\frac{\Delta L}{L}\right|_{calc} = \left.\frac{\Delta L}{L}\right|_{\text{prec}} + \left.\frac{\Delta L}{L}\right|_{matrix} \tag{3}$$

in addition the relative length change

$$\left.\frac{\Delta L}{L}\right|_{matrix} = \frac{\Delta a}{a} \times f_{matrix} \tag{4}$$

of the Al-matrix has to be taken into account. In Equation (4) a denotes the lattice constant of SSSS, Δa the variation of a due to precipitation, and $f_{matrix} = 1 - f_{\text{prec}}$ the atomic fraction of the matrix after β''-formation. The values for $\Delta a/a$ follow from the linear variation of the lattice constant of Al (0.40464 nm)[20] with the amount of solutes as given by [21]

$$\begin{aligned} \Delta a_{(Mg)} &= 0.4555\,\text{pm} \times \text{at\%Mg}, \\ \Delta a_{(Si)} &= -0.1474\,\text{pm} \times \text{at\%Si}. \end{aligned} \tag{5}$$

The quantitative estimation of the length changes $\Delta L/L$ upon formation of β' and β is performed in the same fashion as for β'', again with L referring to the initial state of supersaturated solid solution, i.e. the starting value of the length measurements (t=0 in Figure 1). Here, the maximum amount of both β' and β is determined by the Mg-content (0.65at.%) in SSSS due to the higher relative fraction of Mg in these precipitates compared β''.

The relative variations of $\Delta L/L_{matrix}$ (Equation (4) are independent of the coefficient of thermal expansion. The same pertains to $\Delta L/L_{\text{prec}}$ (Equation (1) assuming that the coefficients of thermal expansion for β' and β'' are the same as that of Al. In the case of β, the different coefficients of thermal expansion for pure Al ($2.67 \times 10^{-5}\,\text{K}^{-1}$, $\Delta T = 320^{\circ}\text{C}$) [22] and β ($1.41 \times 10^{-5}\,\text{K}^{-1}$,

$\Delta T = 320°C$) [23] have to be considered for calculating $\Delta v/v_{\mathrm{prec}}$ (Equation (2)) and $\Delta L/L_{\mathrm{prec}}$.

The relative maximum length changes $(\Delta L/L)_{calc}$, which are estimated in this way according to Equation (3) for the β''-, β'-, or β-preciptation in the three consecutive stages, are given in Table 1 and depicted in Figure 1 as dashed-dotted horizontal lines. As major result, it has to be emphasised that each of the quantitatively estimated length changes fairly well describes the respective experimental data.

The quantitative consideration of $(\Delta L/L)_{calc}$ outlined above sheds light on the two contributions, i.e. the volume excess of the precipitates ($(\Delta L/L)_{\mathrm{prec}}$, Equation (1)), on the one hand, and the associated volume change of the matrix ($(\Delta L/L)_{matrix}$, Equation (4)), on the other hand (see Table 1). Indeed, the remarkable result, that the length decreases upon formation of β' (Figure 1a), finds its explanation in the fact that the expansion, which arises from the volume excess of the precipitate, is less than the contraction of the matrix that is caused by the precipitation of the lattice-expanding Mg-atoms. For β'', a net expansion occurs since in this case the lattice-expanding Mg-atoms and the lattice-contracting Si-atoms segregate in equal amounts and, therefore, the volume contraction of the matrix is lower than in the case of β'-precipitation (Figure 1a). We note that the sign inversion of the relative length change upon precipitation, which arises from the interplay between the precipitate and matrix volume, is a particular feature of dilatometry, that brings additional specificity in the characterisation of precipitates.

Table 1. Summary of relative length changes associated with precipitation of β'', β', and β. f_{prec}, $(\Delta v/v)_{\mathrm{prec}}$, $(\Delta L/L)_{\mathrm{prec}}$: atomic fraction, difference of atomic volume (Equation (2)), and associated relative length change (Equation (1)) of precipitates, respectively. $\Delta a/a$, $(\Delta L/L)_{matrix}$: relative difference of lattice parameter and associated relative length change of matrix (Equation (4)), respectively. $(\Delta L/L)_{calc}$: net estimated relative length change according to Equation (3). $(\Delta L/L)_{exp}$: measured relative length change deduced from the extrema of the $\Delta L/L$ curves. The crystallographic data of the precipitates are taken from literature (for references see text); *n* denotes the number of atoms per unit cell.

Precipitate	β''	β'	β
Composition	$Mg_4Al_3Si_4$	Mg_9Si_5	Mg_2Si
Space group, *n*	C2/m, 22	P63/m, 28	Fm-3m, 12
System	monoclinic	hexagonal	fcc
Lattice parameter [nm]	*a*=1.516 *b*=0.405 *c*=0.674	*a*=0.715 *c*=1.215	*a*=0.6338
f_{prec}	0.0113	0.0101	0.0098
$(\Delta v/v)_{\mathrm{prec}}$	0.092	0.155	0.260
$(\Delta L/L)_{\mathrm{prec}}$ [10^{-4}]	3.47	5.23	8.46
$\Delta a/a$ [10^{-4}]	−3.11	−5.99	−6.12
$(\Delta L/L)_{matrix}$ [10^{-4}]	−3.08	−5.93	−6.06
$(\Delta L/L)_{calc}$ [10^{-4}]	0.39	−0.71	2.40
$(\Delta L/L)_{exp}$ [10^{-4}]	0.53 (180°C)	−0.61 (240°C)	2.60 (340°C)

As shown in Figure 1a, the predicted length change of β'' with respect to SSSS is lower and, vice versa, that for β' is higher than the measured experimental values, i.e. the extrema of the $\Delta L/L$-curves. These correlated shifts presumably arise from the above mentioned delayed onset of the measurement, so that for t=0 a low amount of precipitates probably already exists and, therefore, the reference state does not correspond to entire pure SSSS.

Furthermore, it has to be mentioned that the solute concentration ratio of Si/Mg slightly exceeds that of the precipitates β' and β. The simple quantitative estimation given above therefore implies that a minor part of Si is not precipitated in β' and β. In the case of β at 340°C the non-precipitated part of Si of 0.09 at.% well exceeds the solubility of Si in Al [24]. For β' at 240°C this part amounts to a value of 0.05 at.% that exceeds the solubility limit at this temperature. The excess Si is assumed to segregate at interfaces and to lead to the formation of precipitates with a higher Si fraction, i.e. MgSiAl (so-called U2) [25]. The limiting case that Si precipitate entirely at 240°C would be associated with a fraction of U2 of 0.0033 along with a slightly reduced fraction of β' of 0.0084 and a reduced relative length contraction of -4.4×10^{-5} in this stage. This value is a little less than the experimentally observed one, which may indicate that the fraction of U2 is lower in agreement with literature [17].

Finally, the issue will be briefly addressed in how far the excess volume associated with interfaces between precipitates and the matrix may play a role. The expansion ϵ_{IF} of a hetero-interface of a precipitate, which is incoherent with the matrix, can be assumed to be in the range of that of grain boundaries (ϵ_{GB}). A value ϵ_{GB} of ca. 0.3×10^{-10} m has been deduced for fcc metals by dilatometry [26]. (Note that the thickness ϵ_{IF} or ϵ_{GB} should not be confused with the width of the interface [26].) A spherical precipitate with radius r is associated with an interface excess volume of $4\pi r^2 \epsilon_{IF}$, which results in a relative length change due to the formation of interfaces of

$$\left.\frac{\Delta L}{L}\right|_{IF} = \frac{\epsilon_{IF}}{r} \times f_{\text{prec}}. \tag{6}$$

For a relative fraction of precipitates $f_{\text{prec}} = 0.01$, $(\Delta L/L)_{IF}$ is about two orders of magnitude lower than the measured value $\Delta L/L$ for β, if a precipitate radius r=100 nm is assumed or even less for larger radii. Therefore, length variations due to interfacial excess volume $(\Delta L/L)_{IF}$ are negligible compared to $(\Delta L/L)_{\text{prec}}$ and $(\Delta L/L)_{matrix}$. In the same manner length changes due to remnant vacancies are negligible due to their low concentration according to simulation studies [27].

In conclusion, the present case study demonstrates that high-precision dilatometry serves as a structurally specific and sensitive tool for quantitatively characterising precipitation processes even if they are associated with only tiny

length changes and even if they occur on long time scales which are hardly accessible by other thermal techniques. Although not the topic of this letter, it should be mentioned that these measurements also yield insight into long time scale process kinetics. It is highly specific to derive activation energies or time-temperature-precipitation diagrams for the different precipitates. This type of analysis especially in the present case of Al alloys is subject to a forthcoming publication. The method presented here opens novel pathways to specifically assess precipitation processes in light-weight alloys.

Acknowledgments

The authors are indebted to S. Pogatscher, Inst. Nonferrous Metall., Univ. Leoben, Austria, for chemical analysis and for discussion.

Disclosure statement

No potential conflict of interest was reported by the authors.

References

[1] C. Garcia-Mateo, F. Caballero, C. Caballero and C.G. de Andres, Scripta Mater. 61 (2009) p.855.
[2] F. Wantang, Z. Wang, T. Jing and Y. Zheng, J. Mater. Sci. Technol. 14 (1998) p.478.
[3] F. Lasagni, M. Dumont, C. Salamida, J.A. Acuna and H.P. Degischer, Int. J. Mater. Res. 100 (2009) p.1005.
[4] I. Wierszllyowski and S. Wieczorek, Defect Diff. Forum 237 (2005) p.768.
[5] B. Milkereit, M. Reich and O. Kessler, Mater. Sci. Forum 877 (2017) p.147.
[6] M.I. Daoudi, A. Triki, A. Redjaimia and C. Yamina, Thermochim. Acta 577 (2014) p.5.
[7] A. Grajcar, W. Zalecki, P. Skrzypczyk, A. Kilarski, A. Kowalski and S. Kołodziej, J. Therm. Anal. & Calorim. 118 (2014) p.739.
[8] V. Recarte, R. Pérez-Sáez, M. No and S. Juan, J. Phys. IV France 07 (1997) p.C5-329.
[9] M. Stipcich, A. Cuniberti and V. Noseda Grau, J. Alloy. Compd. 542 (2012) p.248.
[10] M. Luckabauer, W. Sprengel and R. Würschum, Rev. Sci. Instr. 87 (2016) p.075116.
[11] M. Luckabauer, E. Hengge, G. Klinser, W. Sprengel and R. Würschum, *In Situ real-time monitoring of aging processes in an aluminum alloy by high-precision dilatometry*, in *Magnesium Technology 2017*, K. Solanki et al., eds., Springer Intern. Publ., Cham, 2017, p.669–674.
[12] B. Milkereit, N. Wanderka, C. Schick and O. Kessler, Mater. Sci. Eng. A 550 (2012) p.87.
[13] C. Ravi and C. Wolverton, Acta Mater. 52 (2004) p.4213.
[14] M. Takeda, F. Ohkubo, T. Shirai and K. Fukui, J. Mater. Sci. 33 (1998) p.2385.
[15] P.H. Ninive, A. Strandlie, S. Gulbrandsen-Dahl, W. Lefebvre, C.D. Marioara, S.J. Andersen, J. Friis, R. Holmestad and O.M. Løvvik, Acta Mater. 69 (2014) p.126.
[16] H.S. Hasting, A.G. Frøseth, S.J. Andersen, R. Vissers, J.C. Walmsley, C.D. Marioara, F. Danoix, W. Lefebvre and R. Holmestad, J. Appl. Phys. 106 (2009) p.123527.
[17] C.D. Marioara, H. Nordmark, S.J. Andersen and R. Holmestad, J. Mater. Sci. 41 (2006) p.471.

[18] R. Vissers, M.A. van Huis, J. Jansen, H.W. Zandbergen, C.D. Marioara and S.J. Andersen, Acta Mater. 55 (2007) p.3815.
[19] A.H. Geisler and J.K. Hill, Acta Cryst. 1 (1948) p.238.
[20] G. Chiarotti (ed.), Landolt-Börnstein - Group III Condensed Matter 24B: 1.6 Crystal Structures and Bulk Lattice Parameters of Materials, Springer, Berlin, 1994.
[21] W.B. Pearson, A Handbook of Lattice Spacings and Structures of Metals and Alloys, Pergamon Press, Amsterdam, 1958, p.349.
[22] A.J.C. Wilson, Proc. Phys. Soc. 53 (1941) p.235.
[23] M. Imai, Y. Isoda and H. Udono, Intermetallics 67 (2015) p.75.
[24] W.D. Treadwell and R. Walti, Helvet. Chim. Acta 25 (1942) p.1154.
[25] S.J. Andersen, C.D. Marioara, A. Frøseth, R. Vissers and H.W. Zandbergen, Mater. Sci. & Eng. A 390 (2005) p.127.
[26] E.-M. Steyskal, B. Oberdorfer, W. Sprengel, M. Zehetbauer, R. Pippan and R. Würschum, Phys. Rev. Lett. 108 (2012) p.055504.
[27] S. Pogatscher, M. Werinos, H. Antrekowitsch and P.J. Uggowitzer, Mater. Sci. Forum 794–796 (2014) p.1008.

4.5.2 Article 2: Modelling precipitation phase formation and transformation kinetics in AW 6060

Preamble: The article "*High-precision isothermal dilatometry as tool for quantitative analysis of precipitation kinetics: case study of dilute Al alloy*" was published in Journal of Materials Science **54** (5083-5091), December 2018[33].

Based on the length change changes predicted for a maximum content of the precipitation phases appearing, a kinetic model to describe the formation processes of β'' and β'-phase has been sought. The idea to do so has been developed by the author. Likewise, an adequate kinetic model with respect to the chronology of the precipitation phases appearing and with respect to the choice of a suitable framework for their description was found by the author. Model fitting of the dilatometric curves, calculating the activation energies for the phases found to be formed and creating the respective part of the isothermal TTT-diagram has all been performed by the author. The calculation of the activation energies for β''- and β'-formation according to the Kissinger method have been performed by Elisabeth Hengge. The manuscript has been written by the author in collaboration with Roland Würschum and was reviewed by Elisabeth Hengge and Wolfgang Sprengel.

A great number of simulations was required in order to find the adequate kinetic model to describe β''- and β'-precipitate formation for the broad range of temperatures. The model developed represents a simple tool to fully investigate the formation processes of both phases based on dilatometry measurements. Together with the approach presented in the first publication of how to estimate the length changes being associated with phase formation processes, it may thus serve as a template for the simple and secured derivation of activation energies. Together with the TTT-diagram created based on them, they are urgently sought in science as well as in industry.

J Mater Sci

Metals

High-precision isothermal dilatometry as tool for quantitative analysis of precipitation kinetics: case study of dilute Al alloy

R. Enzinger[1], E. Hengge[1], W. Sprengel[1], and R. Würschum[1,*]

[1] *Institute of Materials Physics, Graz University of Technology, Petersgasse 16, 8010 Graz, Austria*

Received: 5 October 2018
Accepted: 29 November 2018

ABSTRACT

An in-depth case study of precipitation kinetics for alloys is presented utilizing recent progress in high-precision isothermal dilatometry by measuring relative length changes down to the range of 10^{-5} and covering large timescales exceeding 10^5 s. Using a dilute Al–Mg–Si alloy as model system, the different phases that form during isothermal heat treatment could quantitatively be analyzed both with respect to the absolute amount of precipitates and with respect to the underlying kinetics. Owing to the distinct length change features upon multi-step precipitation processes, the formation of the metastable β''- and β'-phases can unambigously be detected and furthermore can specifically be distinguished and resolved. From the reaction rate analysis of the precipitation-induced relative length change, that was isothermally measured for temperatures between 170 °C and 260 °C, the evolution with time of the atomic fraction of both the β''- and the β'-phase was determined. The results were also used to construct the isothermal time–temperature–precipitation diagrams which are important for technologically relevant processes.

Introduction

Fast high-temperature dilatometry is widely used in materials science for the characterization of phase transformations and for studying precipitation kinetics in ferrous alloys. For the study of such processes in light-weight alloys at much lower temperatures, the method of primary choice usually is differential scanning calorimetry (DSC) owing to its ease of use and its versatility. For the sake of sensitivity, DSC is commonly applied using time-linear heating, i.e., under non-isothermal conditions; however, this requires more complex procedures of analysis. Compared to DSC, which is based on the heat flow, i.e., the rate of change of a variable, dilatometry directly measures the volume, i.e., a state variable where the measuring signal is independent of the heating rate. Therefore, dilatometry remains sensitive also under long-term isothermal measurement conditions [1–4].

Address correspondence to E-mail: wuerschum@tugraz.at

https://doi.org/10.1007/s10853-018-03210-z

Published online: 06 December 2018

Recently, a highly stable, non-contact dilatometer was developed that enables measurements of relative length changes $\Delta L/L(t)$ under isothermal conditions in the sub-10^{-5} regime with minimized drift over times as long as 10^6 s [5]. This advanced technique opened up the possibility for quantitative studies of precipitation phenomena which are associated with tiny relative length changes that occur on long time-scales and which so far have not been accessible. In order to demonstrate the potentials of this technique especially for assessing technologically relevant processes, a commercial grade Al–Mg–Si alloy (EN AW-6060) was used as a suitable model system [6]. On the one hand, the complex precipitation sequence of this alloy involves metastable phases, and on the other hand, the precipitation sequence of this alloy has been subject of comprehensive research before (for reviews see, e.g., Refs. [7, 8]). In conclusion, the merit of the current experimental approach can easily be demonstrated by comparison with data readily available. As outlined in a preceding paper [6] by the authors' group, from in situ measurements of relative length change, the amount of the metastable coherent β''-phase and the semicoherent β'-phase as well as of the stable β-phase has been determined previously on an absolute scale. There, the observed length change associated with each of the different phases could quantitatively be correlated with the theoretically expected contributions of the length change arising, on the one hand, from the volume excess of the precipitates, and on the other hand, from the volume change of the matrix due to the removal of solute atoms from the Al matrix [6]. This finding already demonstrated that high-precision isothermal dilatometry enables a quantitative volumetric identification of precipitates in dilute alloys.

In the present paper, in order to exploit the full potentials of this dilatometric measuring technique, not only the maximum values of the length changes are considered for determining the amount of precipitates, but also the isothermal behavior of the entire relative length change variation $\Delta L/L(t)$ with time t will analytically be analyzed to study the kinetics of the precipitation processes. The analysis is performed in the framework of the Johnson-Mehl-Avrami-Kolomogorov (JMAK) theory which was found to be suitable to grasp major kinetic features even for complex precipitation sequences in Al alloys [9]. Although it is evident that detailed insight into precipitation processes in Al alloys on an atomistic scale ultimately requires more advanced models (see, e.g., Refs. [10–13]), the application of simple models, like JMAK, allows a direct and analytical fit to experimental data.

The characteristic features of the $\Delta L/L(t)$ dilatometer curves also allows to derive time–temperature–precipitation (TTP) diagrams. For ferrous metals comprehensive atlases of transformation diagrams already exist [14], a proper amount of which has been assembled based on dilatometry data. For nonferrous metals and in particular for light-weight alloys such as aluminum alloys, available data only cover a few selected chemical compositions [15]. For instance, in situ differential scanning calorimetry (DSC) has been applied to study TTP diagrams in Al alloys [16] and in a more recent work dilatometry has been performed under cooling conditions providing significant data in the field of precipitation analysis in Al alloys [17]. However, dilatometric measurements on this kind of alloys have so far been restricted to relatively highly alloyed Al alloys as used in the study mentioned before or to steels [18, 19] which both exhibit volume changes upon precipitation much larger compared to that ones of the Al alloy investigated in this work. Here, we present a direct way to study isothermal TTP diagrams for comparably low-alloyed Al alloys making use of isothermal high-precision dilatometry.

Experimental procedure

The dilatometer measurements were performed in a high-stability non-contact dilatometer based on two-beam Michelson interferometry. A detailed description of the self-developed dilatometer and of the measurement procedure for the Al alloy is given elsewhere by Luckabauer et al. [5] and Hengge et al. [6], respectively. Summarizing briefly, the studies were performed on cylindrical-shaped samples (length: 20 mm, diameter: 5.7 mm) of commercial grade EN AW-6060 Al–Mg–Si alloy. The compositions of the main elements were confirmed by optical emission spectroscopy and a Mg content of 0.65 at.%, a Si content of 0.52 at.%, and additional traces of primarily Fe (0.11 at.%) were determined. For each measurement run, a solution annealing was performed inside the dilatometer at 540 °C for 30 min with then subsequent quenching in a helium gas

stream, then holding at 32 °C for 4 min, and a final fast heat-up (100 °C/min) to temperatures between 170 °C and 260 °C for the isothermal precipitation treatment. Unless otherwise stated the difference between the sample's length right after the heating step to aging temperatures and its actual length standardized to the its length at room temperature is termed as $\Delta L/L$. Prior to the whole experiment series, the sample was annealed at 540 °C for 24 h to obtain a fully recrystallized microstructure.

Hardness measurements (EMCO-TEST DuraJet, Brinell method) as standard characterization technique of the progress of precipitation were also performed for comparison.

Experimental results

Figure 1 shows relative length change curves $\Delta L/L$ obtained during aging in dependence of time t at 180 °C measured for multiple repetitions of the entire measuring sequence comprising solution annealing, quenching, and aging. The good agreement of the various $\Delta L/L(t)$-curves demonstrates the high reproducibility of the measurements and the high stability of the dilatometer. The variation of the Brinell hardness, *HBW*, also shown in Fig. 1, exhibits a maximum at about the same aging time as that of $\Delta L/L$.

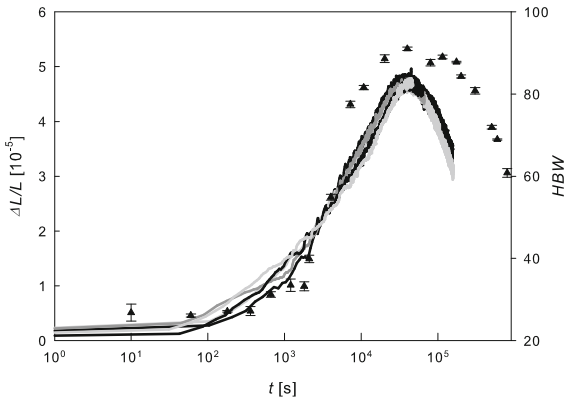

Figure 1 Reproducability of length change measurements and correlation with hardness. Relative length change $\Delta L/L$ in dependence of time t measured at the aging temperature of 180 °C and the corresponding Brinell hardness, HBW, measured upon ex situ aging at 180 °C (black triangle, right-scale axis). Except for the lowest HBW value the size of the error bars are within the size of the symbol.

The characteristic variation of the $\Delta L/L(t)$ curves upon isothermal aging for various temperatures between 170 °C and 260 °C is shown in Fig. 2. For all temperatures except 260 °C, the relative length change $\Delta L/L$ first increases in the range of several 10^{-5} and then subsequently decreases. The maximum in length is shifted to higher values and longer times with decreasing annealing temperature. For 260 °C or 240 °C none or only a tiny length increase occurs prior to the decrease. For 240 °C, 230 °C, and 210 °C, where the minimum value of $\Delta L/L$ is reached during the measuring interval, the differences between the respective $\Delta L/L$-maxima and -minima are very similar and are in the range of 6×10^{-5}. For 170 °C, 180 °C, and 200 °C the $\Delta L/L$-minimum is not yet being reached during the time span of the measurement.

Analysis

Quantitative identification of precipitation sequence

As outlined by the authors in a preceding paper [6] that was focused on the maximum values of the length changes only, the observed increase in the length is due to the formation of the metastable coherent β''-phase and the decrease in the length results from the formation of the metastable semicoherent β'-phase. This conclusion is based on a comparison with available literature data and in particular based on

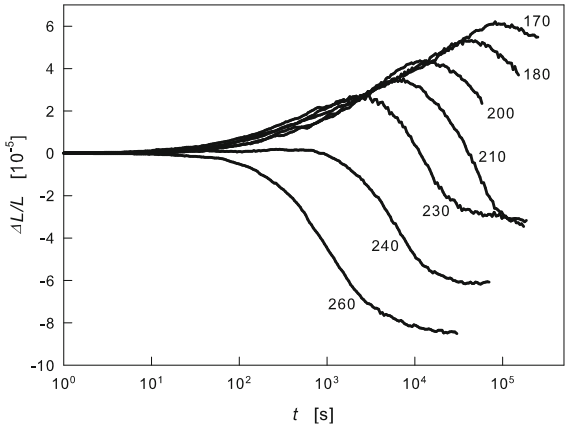

Figure 2 Variation with aging temperature. Relative length change $\Delta L/L$ in dependence of time t measured at the quoted aging temperature (unit °C).

the clear correlation between the aging characteristics of the length change and the hardness (Fig. 1). In fact, the hardness increase is due to the β''-phase as manifested in the hardness maximum [20]. In the subsequent, so-called overaging regime, which coincides with the regime of length decrease, the metastable β'-phase is reported to be the predominant phase [21]. A length increase upon precipitation of the β''-phase and a length decrease upon β'-precipitation turns out to be the result of the counterbalance between the volume expansion due to the formation of the precipitates and the volume contraction of the Al matrix due to the removal of solute atoms from the matrix. For the formation of β'' which is considered to be $Mg_4Al_3Si_4$ (see Ref. [6] and references therein), a net expansion occurs since in this case the Mg atoms that expand the Al matrix and the solved Si atoms that contracts the Al matrix contribute in equal amounts to the precipitates so that the expansion due to the formation of β'' exceeds that of the matrix contraction. Even though the specific volume of β'-precipitates, which are supposed to consist of Mg_9Si_5, is higher than that of β'', a net contraction occurs upon β'-precipitation because the matrix contraction due to the removal of the lattice-expanding Mg atoms dominates (see [6]). This analysis of the various length change contributions does not only yield the correct quantitative amounts for the metastable phases β'' and β', but also that of the final, stable β-phase which can well be observed at higher temperatures within time spans accessible here (see [6]). For the details of the analysis the reader is referred to Ref. [6].

Analysis of precipitation kinetics

In a next step going beyond the consideration of the absolute change of the $\Delta L/L$-curves in the following a central topic will addressed, namely the quantitative analysis of the $\Delta L/L(t)$-curves with respect to the underlying kinetics.

For the rates of formation $\dot{c}_{\beta''}$ for β'' and $\dot{c}_{\beta'}$ for β' we use the following approach for the rate equations:

$$\dot{c}_{\beta''}(t) = k_1\left\{c_0 - \left[c_{\beta''}(t) + c_{\beta'}(t)\right]\right\} - k_2 c_{\beta''}(t)\,, \tag{1}$$

$$\dot{c}_{\beta'}(t) = k_2 c_{\beta''}(t)\,, \tag{2}$$

where $c_{\beta'',\beta'}$ and $k_{1,2}$ are the atomic fractions and formation rates for the precipitate phases β'' and β', respectively, and the parameter c_0 denotes the maximum amount of precipitates which is finally attained. Equation (1) corresponds to JMAK kinetics for the formation of β'' (Avrami exponent of $n = 1$) combined with a second term dealing with the transformation to the β'-phase. The rate ansatz according to Eq. (2) describes a situation where β' is formed by transformation of β'', a notion which is in line with the literature [21, 22] and which will be extended below for elevated temperature.

For the initial conditions $c_{\beta''}(t=0) = c_{\beta'}(t=0) = 0$ the solutions for β'' (Eq. 1) and β' (Eq. 2) read:

$$c_{\beta''}(t) = c_0 \frac{k_1}{k_2 - k_1}\left\{\exp(-k_1\,t) - \exp(-k_2\,t)\right\}, \tag{3}$$

$$c_{\beta'}(t) = c_0 \frac{1}{k_2 - k_1}\left\{-k_2\exp(-k_1\,t) + k_1\exp(-k_2 t)\right\} + c_0\,. \tag{4}$$

And the total amount of precipitates $\beta_{tot}(t)$ is given by

$$c_{\beta,tot}(t) = c_{\beta''}(t) + c_{\beta'}(t) = c_0\left[1 - \exp(-k_1\,t)\right]. \tag{5}$$

According to Eq. (5), irrespective of a mutual transformation of β'' and β', the formation of the total amount of precipitates is governed by the rate constant k_1. Since c_0 represents the limiting value of $c_{\beta'}$ (Eq. 4), a value of $c_0 = 0.0101$ is taken which was derived for the maximum amount of the β'-phase, and which is slightly less than the value of 0.0113 derived for β'' (see Ref. [6]).

For fitting the $\Delta L/L$-curves, the coefficients $(\Delta L/L)/c$ for the variation of $\Delta L/L$ with $c_{\beta''}$ and $c_{\beta'}$ are taken from our previous work [6]. Then a fraction of 0.0101 for β' corresponds to $\Delta L/L = -0.71 \times 10^{-4}$, i.e., a coefficient $(\Delta L/L)/c = -7.03 \times 10^{-3}$. For β'', $\Delta L/L = 0.39 \times 10^{-4}$ is obtained for a maximum fraction of 0.0113 [6], corresponding to $(\Delta L/L)/c = 3.35 \times 10^{-3}$. This finally yields the fit curve

$$\frac{\Delta L}{L}(t) = 3.35 \times 10^{-3}\, c_{\beta''}(t) - 7.03 \times 10^{-3}\, c_{\beta'}(t)\,, \tag{6}$$

with $c_{\beta''}(t)$, $c_{\beta'}(t)$ according to Eqs. (3) and (4). Fitting the experimental $\Delta L/L(t)$-curves yields for each aging temperature the two rates k_1 and k_2 as the only fit parameters. The values of k_1 and k_2 deduced from the analyses of the $\Delta L/L(t)$-curves for the various isothermal temperatures are shown in Fig. 3 in an Arrhenius representation. It is evident that for high temperatures the two-rate fit is inappropriate, since

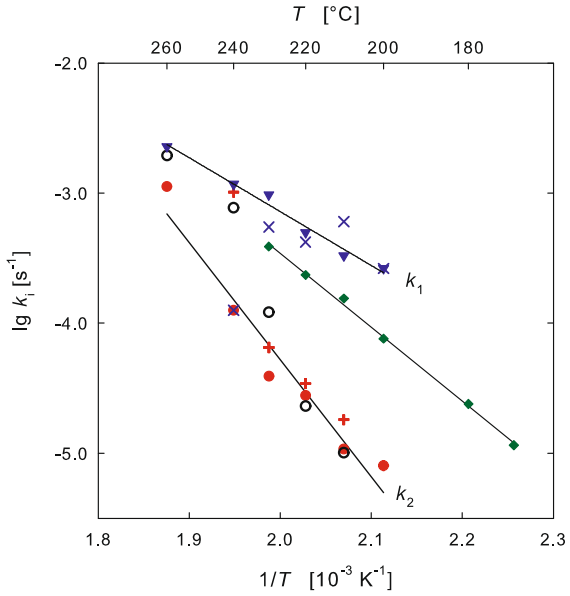

Figure 3 Arrhenius plot of precipitation kinetics. Arrhenius representation of reaction rates k_1 (blue), k_2 (red), k_3 (black, empty circle) determined from fitting the $\Delta L/L$-curves according to the present model as well as Arrhenius representation of the temporal shift of the peak maxima (green, diamond) of the $\Delta L/L$-curves (Fig. 2) with varying temperature T according Eq. (11). k_1 (blue, two-rates fit: ×, three-rates fit: filled inverted triangle), k_2 (red, two-rates fit: +, three-rates fit: filled circle).

the $\Delta L/L(t)$-decrease without preceding increase, e.g., for 240 °C (Fig. 2) would imply a rate k_1 at this temperature that is lower than those at the lower temperatures (see crosses in Fig. 3). As characteristic for metastable precipitation phenomena, this indicates that for the high temperatures, in addition to a $\beta'' \rightarrow \beta'$ transformation, β'-precipitates may also form directly. In the rate equation system above (Eqs. 1, 2), a direct formation of β' (concentration: $c_{\beta'_{\mathrm{dir}}}$) can be considered in a straightforward manner by an additional rate equation

$$\dot{c}_{\beta'_{\mathrm{dir}}}(t) = k_3\left\{c_0 - \left[c_{\beta''}(t) + c_{\beta'}(t) + c_{\beta'_{\mathrm{dir}}}(t)\right]\right\} \tag{7}$$

and a corresponding extension of Eq. (1) by the summand $c_{\beta'_{\mathrm{dir}}}(t)$ within the angular shaped brackets. The solution for this three-rates approach reads

$$c_{\beta''}(t) = c_0 \frac{k_1}{k_2 - (k_1 + k_3)}\left\{\exp(-(k_1 + k_3)\,t) - \exp(-k_2\,t)\right\}, \tag{8}$$

$$c_{\beta'}(t) = c_0 \frac{1}{k_2 - (k_1 + k_3)} \left\{-\frac{k_2 k_1}{k_1 + k_3}\exp\left(-(k_1 + k_3)\,t\right) + k_1 \exp(-k_2 t)\right\} + c_0 \frac{k_1}{k_1 + k_3}\,. \tag{9}$$

$$c_{\beta'_{\mathrm{dir}}}(t) = c_0 \frac{k_3}{k_1 + k_3}\left\{1 - \exp(-(k_1 + k_3)\,t)\right\}, \tag{10}$$

which for $k_3 = 0$ contains as special case the two-rates solutions (Eqs. 3, 4). As shown in Fig. 3, the rate k_3 for the direct formation of β' starts to exceed the rate k_2 of the $\beta'' \rightarrow \beta'$ transformation at 200 °C and steeply increases for higher temperatures, demonstrating that in this temperature regime direct β-formation prevails.

Fitting the experimental $\Delta L/L(t)$-curves with the three-rates solutions by replacing $c_{\beta'}(t)$ in Eq. (6) by $[c_{\beta'}(t) + c_{\beta'_{\mathrm{dir}}}(t)]$ yields pretty similar rates k_1 and k_2 for $T < 240$ °C as the two-rates solution (see Fig. 3). From linear fits of the three-rates solutions including $T = 240$ °C, the activation energies $Q_1 = (0.90 \pm 0.30)$ eV and $Q_2 = (1.42 \pm 0.28)$ eV can be deduced for the reactions rates k_1 and k_2, respectively. As shown in Fig. 4 for representative temperatures, the present model according to Eq. (6) yields

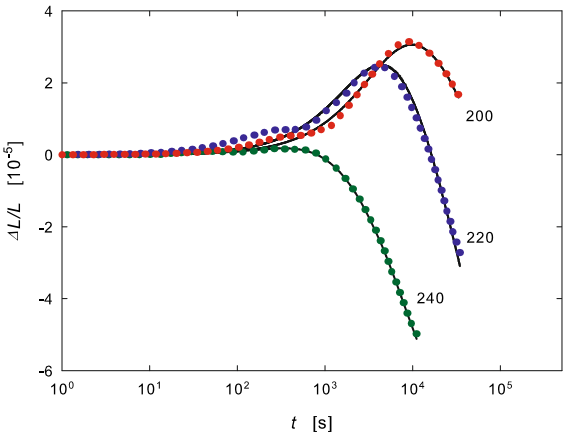

Figure 4 Fit of $\Delta L/L$-curves (solid lines) according to the present model (Eq. 6). Dotted lines: corresponding experimental curves (cf. Fig. 2). The aging temperature (unit °C) are quoted. $T = 200, 220$ °C: two-rates fit (Eqs. 3, 4); $T = 240$ °C: three-rates fit (Eqs. 8–10).

fits that reasonably well match to the experimental $\Delta L/L$-curves.

For the sake of completeness, in addition to the above deduced kinetics, as derived from fitting of the $\Delta L/L$-curves, a simple kinetic analysis can be obtained from the temporal shift of the peak maxima of the $\Delta L/L$-curves. For this purpose the time t corresponding to each peak maximum of $\Delta L/L$ (Fig. 2) is plotted in Fig. 3 in an Arrhenius representation with varying temperature T, i.e.,

$$\frac{1}{t} = \frac{1}{t_0}\exp\left(-\frac{Q_{\text{eff}}}{k_B T}\right), \tag{11}$$

where t_0^{-1} denotes a pre-exponential factor and Q_{eff} the activation energy. From the linear fit of the data (Fig. 3), a value $Q_{\text{eff}} = (1.13 \pm 0.07)$ eV is deduced for the activation energy. This value is between those obtained for k_1 and k_2 (Fig. 3, see discussion).

TTP diagram

From the $\Delta L/L(t)$-curves a time–temperature–precipitation (TTP) diagram can be constructed. In the following, data points of the isothermal TTP diagram will at first be derived directly from the $\Delta L/L(t)$-curve and then from the fitted data obtained in the preceding section.

The temperature T and time t associated with each extremum of the $\Delta L/L(t)$-curves define one set of data points in the time–temperature–precipitation (TTP) diagram. The maxima of the $\Delta L/L(t)$-curves (Fig. 2) correspond to the respective temperature and time where the metastable β''-phase attains its maximum amount. For the metastable β'-phase the characteristic T- and t-values are given by the onset where the minimum of $\Delta L/L(t)$ is reached. The corresponding data points of the isothermal TTP diagram, which can directly be constructed in this way from the dilatometer measurements, are shown in Fig. 5 as filled symbols.

Additionally, isothermal TTP data for $c_{\beta''}(t)$ and $c_{\beta'}(t)$ can also be derived from the fitted values k_1, k_2 and the corresponding linear interpolations according to an Arrhenius behavior (Fig. 3) by making use of the relation between $c_{\beta''}(t)$, $c_{\beta'}(t)$ and k_1, k_2 (Eqs. 3, 4).[1] Corresponding sets of $c_{\beta''}(t)$- and $c_{\beta'}(t)$-curves for various temperatures are shown in Fig. 6, which yield the TTP data depicted in Fig. 5. For β'', the TTP data points are taken from the maxima of the $c_{\beta''}(t)$-curves (see crossed symbols in Fig. 6a); for β' the TTP data points correspond to $c_{\beta'} = 0.98$ (see crossed symbols in Fig. 6b).

From the $c_{\beta''}(t)$- and $c_{\beta'}(t)$-plots in Fig. 6 also the time span, after which any other fraction of precipitates is reached, can be determined directly. For the sake of illustration, the threshold values for reaching 60 % of the maximum concentration of β'' and β' are also shown in Fig. 5.

Discussion

The analysis in the preceding section demonstrates that high-precision dilatometry serves as sensitive tool for the quantitative analysis of precipitation processes even if they are associated with only tiny length changes and even if they occur on long time-scales. The $\beta'' \rightarrow \beta'$ transformation in Al–Mg–Si alloys, which could be resolved in detail here, is hardly accessible by other thermal techniques as stated, e.g., for standard DSC [16]. Also with standard dilatometry upon linear heating, the formation of β'' in Al–Si–Mg alloys is much weaker discernible [23].

The substantially enhanced sensitivity in the present studies allowed a detailed kinetic analysis. Here, the sign inversion of the relative length change upon $\beta'' \rightarrow \beta'$ transformation, which arises from the interplay between the precipitate and matrix volume, turned out as a particular feature of dilatometry that brings additional specificity for the precipitate characterization. The deduced activation energies are similar to those found earlier for Al–Si–Mg alloys [23]; they also can be considered as characteristic for metastable precipitates in Al alloys [24, 25]. The quantitative analysis confirms that the $\Delta L/L$-maximum arises from the competing effects of expansion and contraction due to β''- and β'-formation, respectively. Since the coefficients of expansion due to the formation of β'' and the contraction due to the formation of β' are different (see Eq. 6), it is evident that the maxima arising from the sum of these contributions is shifted to earlier times compared to the time when a maximum amount of β''-phase is present. Therefore, the activation energy Q_{eff} deduced above from the time shift of the maximum of the length

[1] The consideration is restricted to the temperature regime $T < 240$ °C for which the two-rates model is valid.

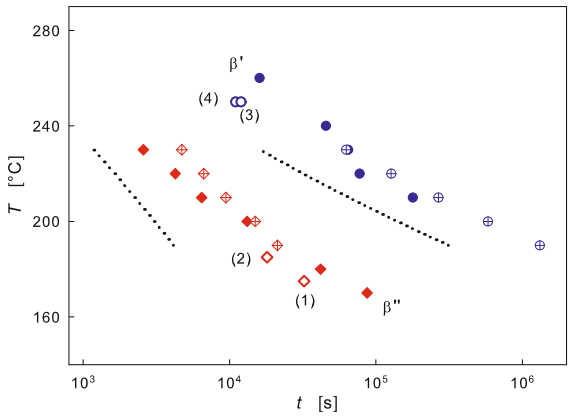

Figure 5 Isothermal TTP diagram. Time–temperature–precipitation (TTP) characteristic for the formation of β''- and β'-precipitates in AW 6060. Filled symbols refer to data directly taken from $\Delta L/L$-curves (maxima: β''; mimina: β'; see text); crossed symbols denote the values deduced from the fit with two rates $k_{1,2}$ (see crossed symbols in Fig. 6a, b). The dotted lines show the threshold values for reaching 60 % of the maximum concentration of β'' and β' (see filled symbols in Fig. 6a, b). The numbered data points (empty symbols) refer to data taken from literature (see Table 1).

increase with aging temperature can be considered as an effective value, at most. These maxima should therefore also not be conceptually intermixed with those occurring upon heat release in DSC. Since the coefficients of expansion due to the formation of β'' and the contraction due to the formation of β' are different (see Eq. 6), it is evident that the maximum arising from the sum of these contributions is shifted to earlier times compared to the point when the β''-phase attains its maximum value. From this point of view, it is also quite clear that the value of activation energy Q_{eff} lays between those of the rates k_1 and k_2 for the formation of β''- and β'-formation, respectively. One should also note that the $\Delta L/L$-maximum for each temperature can be well described by the present model (Eq. 6); however, this is not the case for the minimum which starts to occur toward the end of each measuring run (Fig. 2). These minima are due to a further transformation process of the β'-precipitates. A quantitative kinetic description of this process on the basis of a model correspondingly extended by a further rate constant would, however, require measurements for even longer aging times well exceeding 10^5 s.

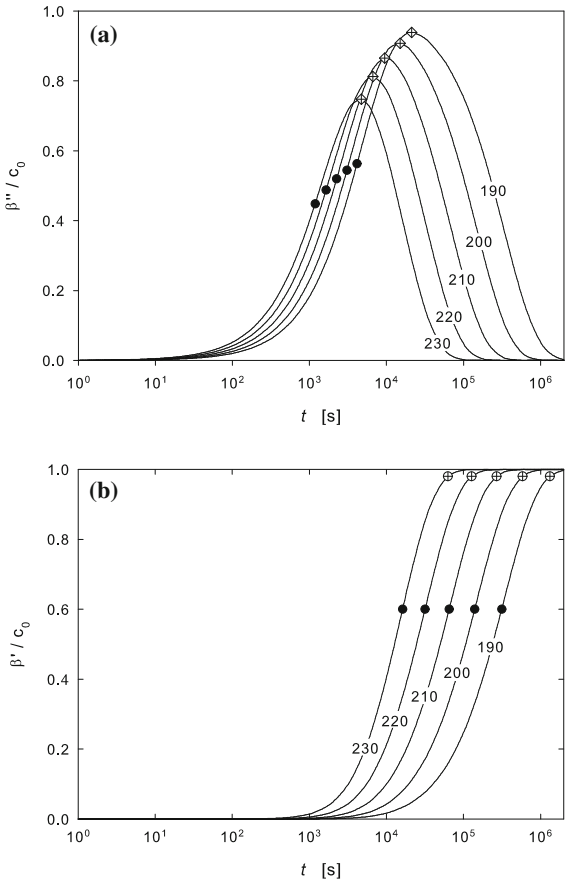

Figure 6 Evolution of the formation of precipitates β' (a) and β'' (b) with time for various temperatures according to fit of present model with two rates $k_{1,2}$ (Eqs. 3, 4). The symbols marked with a cross correspond to the maximum (a) or to a fraction of 0.98 (b) of the relative concentration $c_{\beta',\beta''}/c_0$; the filled symbols mark 60 % of the maximum concentration.

Finally, we will address the attractive potentials of dilatometry for constructing TTP diagrams. The part of the isothermal TTP diagram presented here (Fig. 5) focuses on the technologically most relevant range of temperatures for the formation of β'' and β'. It nicely summarizes that at low aging temperatures and short aging times, first the β''-phase is formed, which transforms into the β'-phase at higher temperatures. The good agreement between the data points deduced directly from the extrema of the $\Delta L/L$-curves and the data points deduced from the model fit (Fig. 5) confirm the assumption made above that the extrema of the dilatometric curves represent the respective maximum concentration of β'' and β'.

Table 1 Data points of the TTP diagram (see Fig. 5) that have been extracted from literature. The number (No.) corresponds to the number in that figure

No.	T (°)	t (s)	Precipitate	References
(1)	175	32400	β''	[26]
(2)	185	18000	β''	[27]
(3)	250	11000	β'	[21]
(4)	250	12000	β'	[28]

However, for β'' at elevated temperatures the corresponding $\Delta L/L$-maximum occurs at slightly lower temperatures compared to the calculated $c_{\beta''}$-maximum. This arises from the opposing contribution of β'' and β' to the overall volume change and the fact that with increasing temperature the onset of β'-formation is more strongly shifted to shorter times compared to that of β''. As demonstrated by the lines representing 60 % of already formed phase (Fig. 5), the data obtained from fitting the $\Delta L/L$-curves allow to determine the relative amount of β'' and β' at any desired point in the isothermal TTP diagram, i.e., for specific technologically relevant heat treatment condition. It should be noted that this type of isothermal TTP diagram, which has been obtained starting from supersaturated solid solution by a heating step to the respective aging temperature has to be distinguished from the TTP diagrams obtained from dilatometric curves under, e.g., cooling conditions [17].

For comparison, four data points extracted from TEM investigations taken from the literature are included in the diagram (Fig. 5). According to those studies, the maximum amounts of β'' and β' prevail for the temperatures and times quoted in Table 1, whereby the samples have been subjected to equivalent isothermal heat treatment. These data points fit remarkably well to the present results obtained by dilatometry.

The characteristic C-curve in the TTP diagram should, in principle, also be detectable with dilatometry. This requires an appropriate adjustment of the heating unit in order to monitor the very early stage of the precipitation processes in the first hundreds of seconds of aging. The focus of the present work, however, laid on long range isothermal aging condition.

It becomes evident from the discussion above that the direct access to the application-relevant TTP diagrams marks a highly attractive feature of the present simple kinetic analysis. However, it is also apparent that the presented high-precision dilatometry with its particular length change characteristics upon multi-step precipitation processes provides a superior experimental database which is highly suitable for advanced modeling as well.

Acknowledgements

Open access funding provided by Graz University of Technology. The authors are indebted to Dr. Martin Luckabauer (Inst. Mater. Res., Tohoku Univ., Sendai, Japan) for fruitful discussion.

References

[1] Garcia-Mateo C, Caballero F, Capdevila C, de Andres CG (2009) Estimation of dislocation density in bainitic microstructures using high-resolution dilatometry. Scripta Mater 61:855–858

[2] Grajcar A, Zalecki W, Skrzypczyk P, Kilarski A, Kowalski A, Kołodziej S (2014) Dilatometric study of phase transformations in advanced high-strength bainitic steel. J Therm Anal Calorim 118:739–748

[3] Wantang F, Wang Z, Jing T, Zheng Y (1998) A new approach to isothermal precipitation kinetics of carbides. J Mater Sci Technol 14:478–480

[4] Recarte V, Pérez-Sáez R, No M, Juan S (1997) Dilatometric study of the precipitation kinetics in Cu–Al–Ni shape memory alloys. J Phys IV France 07(C5):329–334

[5] Luckabauer M, Sprengel W, Würschum R (2016) A high-stability non-contact dilatometer for low-amplitude temperature-modulated measurements. Rev Sci Instr 87:075116

[6] Hengge E, Enzinger R, Luckabauer M, Sprengel W, Würschum R (2018) Quantitative volumetric identification of precipitates in dilute alloys using high-precision isothermal dilatometry. Philos Mag Lett. https://doi.org/10.1080/09500839.2018.1542170. (**in press**)

[7] Ravi C, Wolverton C (2004) First-principles study of crystal structure and stability of Al–Mg–Si–(Cu) precipitates. Acta Mater 52:4213–4227

[8] van Huis M, Chen J, Zandbergen H, Sluiter M (2006) Phase stability and structural relations of nanometer-sized, matrix-embedded precipitate phases in Al–Mg–Si alloys in the late stages of evolution. Acta Mater 54:2945–2955

[9] Sha W (2007) Application of simple practical models for early stage ageing precipitation kinetics and hardening in aluminium alloys. Mater Des 28:528–533

[10] Svoboda J, Shan YV, Kozeschnik E, Fischer FD (2017) Couples and pairs formation-thermodynamic and kinetic modelling applied to Al–Mg–Si. Model Simul Mater Sci Eng 25:065011

[11] Fallah V, Stolle J, Ofori-Opoku N, Esmaeili S, Provatas N (2012) Phase-field crystal modeling of early stage clustering and precipitation in metal alloys. Phys Rev B 86:134112

[12] Fallah V, Korinek A, Ofori-Opoku N, Raeisinia B, Gallerneault M, Provatas N, Esmaeili S (2015) Atomic-scale pathway of early-stage precipitation in Al–Mg–Si alloys. Acta Mater 82:457–467

[13] Liang Z, Chang CST, Abromeit C, Banhart J, Hirsch J (2012) The kinetics of clustering in Al–Mg–Si alloys studied by Monte Carlo simulation. Int J Mater Res 103:980–986

[14] Vander Voort GF (ed) (1991) Atlas of time–temperature diagrams for irons and steels. ASM Intern, Materials Park

[15] Vander Voort GF (ed) (1991) Atlas of time–temperature diagrams for nonferrous alloys. ASM Inter, Materials Park

[16] Milkereit B, Giersberg L, Kessler O, Schick C (2014) Isothermal time–temperature–precipitation diagram for an aluminum alloy 6005A by in situ DSC experiments. Materials 7:2631–2649

[17] Milkereit B, Reich M, Kessler O (2017) Detection of quench induced precipitation in Al alloys by dilatometry. Mater Sci Forum 877:147–152

[18] Pastor A, Valles P, Medina SF (2017) Study of phase transformations in steel x38crmov5-1 using dilatometry and differential thermal analysis. Steel Res Int 88:1600229

[19] Piyada S, Nataliya T, Christoph K, Wolf W, Ulrich P, Dietmar H, Wolfgang B (2008) Phase transformation modelling and parameter identification from dilatometric investigations. Steel Res Int 79:793–799

[20] Takeda M, Ohkubo F, Shirai T, Fukui K (1998) Stability of metastable phases and microstructures in the ageing process of Al–Mg–Si ternary alloys. J Mater Sci 33:2385–2390. https://doi.org/10.1023/A:1004355824857

[21] Marioara CD, Nordmark H, Andersen SJ, Holmestad R (2006) Post-β'' phases and their influence on microstructure and hardness in 6xxx Al–Mg–Si alloys. J Mater Sci 41:471–478. https://doi.org/10.1007/s10853-005-2470-1

[22] Tsao CS, Chen CY, Jeng US, Kuo TY (2006) Precipitation kinetics and transformation of metastable phases in Al–Mg–Si alloys. Acta Mater 54:4621–4631

[23] Daoudi MI, Triki A, Redjaimia A, Yamina C (2014) The determination of the activation energy varying with the precipitated fraction of β'' metastable phase in an Al–Mg–Si alloy using non-isothermal dilatometry. Thermochim Acta 577:5–10

[24] Dorward RC (1973) Preaging effects in Al–Mg–Si alloys. Metall Trans 4:507–512

[25] Ovono DO, Guillot I, Massinon D (2007) Determination of the activation energy in a cast aluminium alloy by TEM and DSC. J Alloys Compd 432:241–246

[26] Murayama N, Uemori R, Hashimoto N, Saga M, Kikuchi M (1997) Effect of silicon addition on the composition and structure of fine-scale precipitates in Al–Mg–Si alloys. Scripta Mater 36:89–93

[27] Andersen S, Zandbergen H, Jansen J, Træholt C, Tundal U, Reiso O (1998) The crystal structure of the β'' phase in Al–Mg–Si alloys. Acta Mater 46:3283–3298

[28] Matsuda K, Sakaguchi Y, Miyata Y, Uetani Y, Sato T, Kamio A, Ikeno S (2000) Precipitation sequence of various kinds of metastable phases in Al–1.0mass % Mg_2Si–0.4mass% Si alloy. J Mater Sci 35:179–189. https://doi.org/10.1023/A:1004769305736

4.6 Summary and conclusion

A complete kinetic model for the formation of β''- and β'- precipitation phases in AW 6060 has been developed. In correspondence with the measurements performed, it offers the indispensably important basis for qualitative as well as quantitative analyses of these phase formation processes, which yield important quantities like the activation energies for their formation as well as the possibility to identify phase region.

Article 1: "*Quantitative volumetric identification of precipitates in dilute alloys using high-precision isothermal dilatometry*"

- A model has been created, which allows to predict the length changes occurring in AW 6060-samples upon precipitation phase formation processes based on information about the composition and lattice structure of the respective phases.
- An extensive literature survey has been carried out collecting information about compositions and lattice structures of the precipitation phases which are most likely to be formed upon isothermal ageing at various temperatures in AW 6060.
- By applying the model derived, the length changes accompanying the formation of the largest possible amount of the respective precipitation phases has been calculated. By comparing them to the measured length changes for temperatures, where, according to results from secondary techniques and information from literature, a maximum content of the respective precipitation phases is present, the appearance of the individual phases has been identified and, in return, the validity of the model derived has been proven.
- For the calculations performed, the excess volume coming along with the interfaces of the precipitate had been neglected a priori. Their influence has been justified to be negligible posteriori by assuming a typical degree of excess volume coming along with the interfaces of the individual precipitates.

Article 2: "*High-precision isothermal dilatometry as tool for quantitative analysis of precipitation kinetics: case study of dilute Al alloy*"

- Based on the calculations to estimate the sample length changes appearing upon the formation of β''- and β'-precipitation phases introduced in the first publication, kinetic models for the parallel and consecutive emergence of both phases have been tested. Consecutive formation of β''- and β'-precipitation phase in the framework of the JMAK-kinetic model has been found to be adequate. The Avrami-exponent has been found to be $n = 1$, in agreement of the diffusion-controlled formation of small particles.

- Fitting the dilatometric data obtained by the kinetic model for the entire temperature range, where β''-formation and its transformation to β' occurs, the phase fractions present at any time as well as the temperature dependent formation rates could be determined.

- Based on the temperature dependent rates and phase fractions, activation energies for the formation of both phases could be determined and the isothermal TTT-diagram be created.

5 | Phase Formation Processes in a Strongly β-Stabilised Ti-V-Alloy

Titanium alloys are widely recognised for offering a superior combination of properties, including a high strength-to-weight ratio, great corrosion resistance as well as excellent biocompatibility making them indispensable for modern industrial society[78–80]. Owed to their high production costs, however, their use remains reserved rather for a number of special applications than for widespread usage[81].

Compared to other classes of Ti-alloys, β-Ti-alloys are not as favourable to be used due to their higher mass density and reduced corrosion resistance. Nonetheless, focus has increasingly shifted to this class over the past decades due to the possibility of keeping these alloys entirely in the β-phase or creating sophisticated $\alpha+\beta$-microstructures by heat-treating them, making in this way accessible a broader range of mechanical and functional properties.

In former times, emphasis used to be put on preventing the formation of metastable nanoscale ω-phase in these alloys, which appears in the course of common heat treatments, because of its detrimental influence on mechanical properties[82,83]. Today, however, research is devoted to this phase eagerly in order to find (better) methods of suppressing its formation or to use it as precursor for finely dispersed metastable α''- or equilibrium α-phase precipitates[84,85]. Furthermore, the general complexity associated with ω-phase formation and evolution makes its investigation a profitable topic from a physical point of view[86].

5.1 Basics

5.1.1 Classification of Ti-Alloys

Pure titanium is an allotropic material, i.e., it appears in different crystal structures in its solid state. The more loosely-packed body-centred-cubic (bcc) β-phase is stable at temperatures exceeding 882 °C and the hexagonal close-packed (hcp) α-phase is stable at temperatures beneath (see Fig.5.1(a) and Fig.5.3). According to the kind of element added, alloying results in...

(i) ... stabilising the α-phase field towards even higher temperatures (see Fig.5.1 (b)). This is equivalent to an increase of the so-called the *β-transus temperature*. Accordingly, the respective alloying elements are called *α-stabilisers* which are found to dissolve either interstitially (e.g. O, N, C) or substitutionally (e.g. Al).

(ii) ... stabilising the β-phase field towards lower temperatures (see Fig.5.1 (c) and (d)). This is equivalent to a decrease in the β-transus temperature. The respective alloying elements are designated to as *β-stabilisers* which are subdivided into β-isomorphous (e.g. Mo, Nb, V, Ta) and β-eutectoid (e.g. Fe, Cr, Mn, Co) ones.

(iii) ... no or even minor effect on the phase fields (see Fig.5.1 (a)). These elements are thus referred to as *neutral* (e.g. Sn, Zr).

The phase diagrams for the respective classes of alloying elements resemble each other, where the specific values of two-phase lines, points of coexistence, or other features naturally differ from one case to the other.

Due to yet decent ultimate strength values equal to that of low-graded steels, titanium is applied to a large fraction in its technically pure form in four grades featuring different contents of oxygen which is its most important α-stabiliser. However, in order to make the full range of properties accessible, some fraction of β-phase has to be stabilised at $T_{amb.}$ or

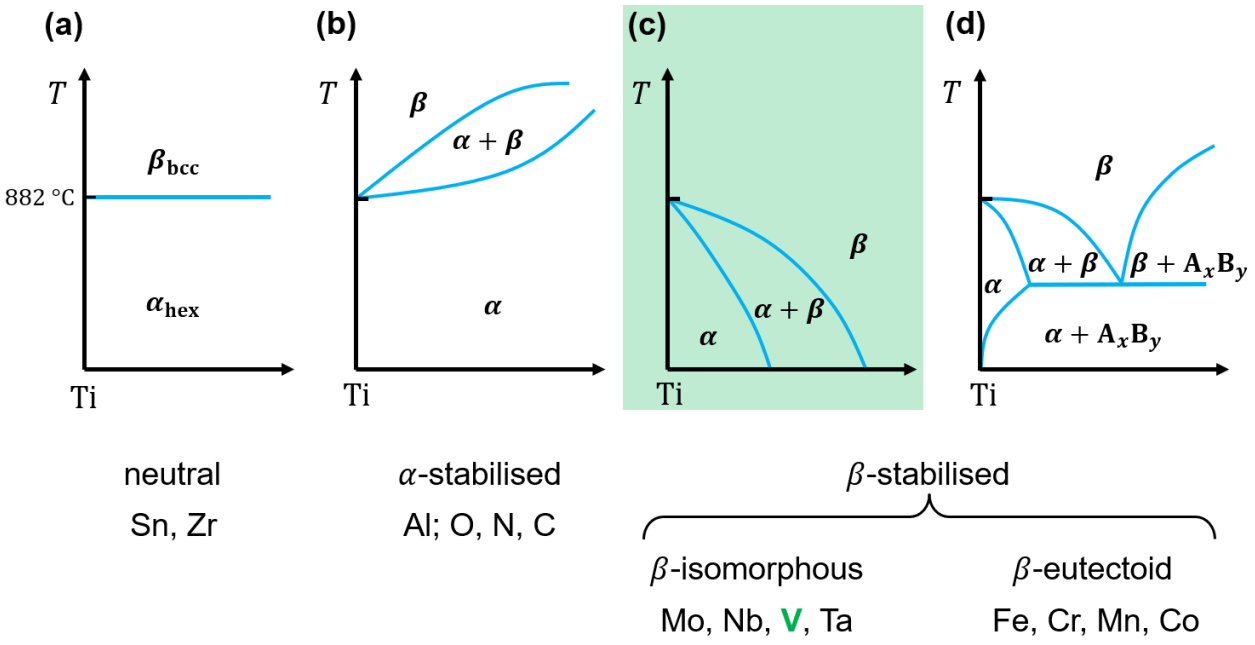

Figure 5.1: Schematic phase diagrams of Ti-alloys obtained by adding different types of alloying elements. The alloy investigated throughout this work is a Ti-V-alloy which belongs to the β-isomorphous class (highlighted in green).

the material even kept fully in the β-phase, but at the lowest β-stabiliser content possible. Compared to the α-phase, the β-phase shows increased ductility and ensures higher diffusion rates, but at reduced strength and creep resistance. Correspondingly, the resulting mechanical properties of such β-Ti-alloys are mainly determined by the absolute phase fractions of α- and β-phase as well as by their microstructural arrangement which may be adjusted to suit the requirements by applying certain combinations of mechanical processing and heat treatments. Hence, the microstructure is found to be either more lamellar or equiaxed in fine or coarse configuration, providing each a unique combination of mechanical properties (for a detailed overview of this topic see for instance[78]).

In case of β-isomorphous Ti-alloys, their β-stabiliser content determines their subdivision into α-, near-α-, $\alpha + \beta$-, metastable β- or stable β-alloys (see Fig.5.2), where again, each class features a certain spectrum of characteristics.[1] As a key feature, $\alpha + \beta$- as well as metastable β-Ti-alloys are heat-treatable. A common heat treatment comprises solution an-

[1]Note: The region, where decomposition of the β-phase is favoured, is found to be either stable or metastable depending on the presence of impurity elements like oxygen, inter alia[87].

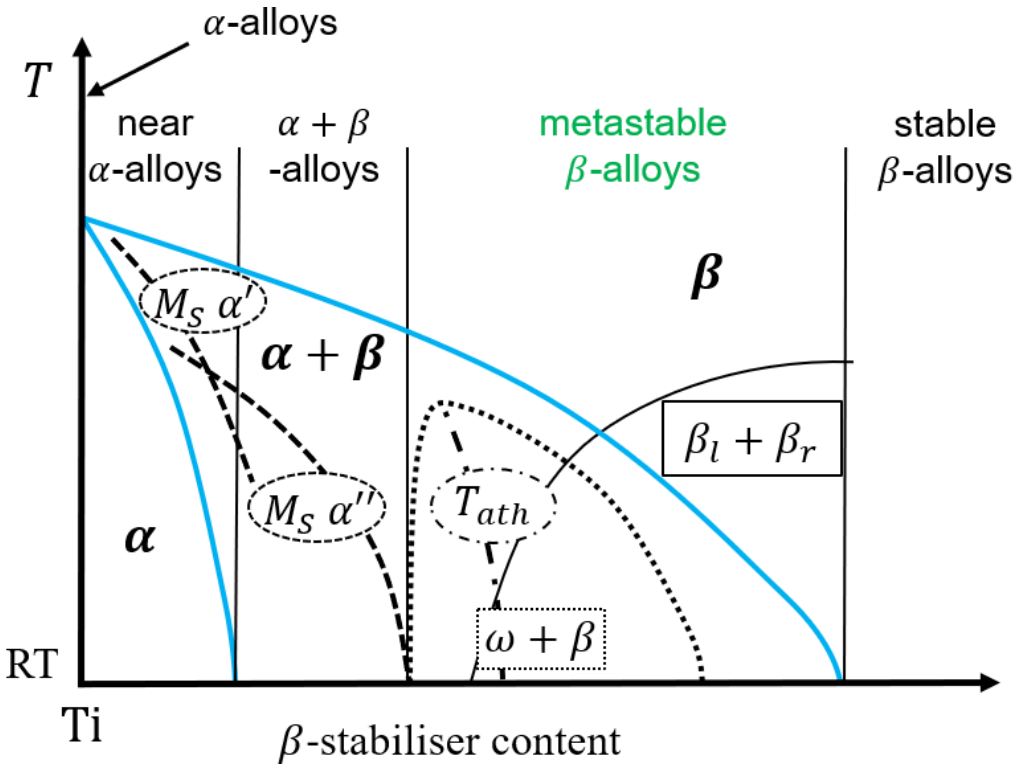

Figure 5.2: Schematic phase diagram of β-isomorphous Ti-alloys with the phase regions of α-, near-α-, $\alpha + \beta$-, metastable β- and stable β-alloys marked according to their common classification. Additionally, the starting lines M_S for martensitic α' or α'' formation (dashed lines) and for athermal ω-formation T_{ath} (dash-dotted line) are drawn. The dotted contour line marks the phase region, where ω-formation takes place and the solid black contour line marks the phase region, where decomposition of the (quenched) β-phase into β-stabiliser lean and rich regions, β_l and β_r, takes place.[2]

nealing at temperatures in the β-phase region, quenching, and subsequent ageing at elevated temperatures in the $\alpha + \beta$-phase region. Upon quenching, the high-temperature β-phase is retained in an unstable state, so part of it transforms to metastable phases and/or the equilibrium α-phase during subsequent ageing making accessible even more advanced phase structures. In the case of α and $\alpha+\beta$-alloys, martensitic transformation occurs upon quenching down below the the so-called M_S lines (martensite start) leading to a formation of α'- and α''-martensitic phases (dashed formation lines in Fig.5.2). To this group belongs Ti-6Al-4V, one of the first and most thoroughly investigated Ti-alloys, which possesses a market share of more than 50 % today, due to its well balanced spectrum of mechanical properties.

[2]Note: This phase diagram is only a schematic drawing, so the exact positions, sizes, and shapes of the phase regions and formation lines are found to vary from alloy to alloy.

With regards to the investigations presented hereafter, these have been conducted at Ti-samples with a nominal content of Ti 21 at%V, which belongs to the group of metastable β-alloys. In this case, upon quenching from solution annealing temperatures, the formation of another metastable phase, the so-called ω-phase is observed, which has been described as a kind of a local martensitic transformation[88]. ω-phase formation is found to happen via different modes. In this context, T_{ath} (dashed-dotted-line in Fig.5.2) marks the temperature, where, when being undershot, ω-formation inevitably starts yet during quenching. Besides this, ω-phase is known to be created by other formation modes in the course of heat treatments resulting in a whole region, where it has been found to emerge (area limited by the dotted line in Fig.5.2). Additionally, an underlying spinodal decomposition process of the β-phase into β-stabiliser lean and rich regions denoted by β_l and β_r is known to be obligatory for some ω-formation modes (area limited by solid black line in Fig.5.2).

5.1.2 ω-phase formation modes and ω-to-α-transformation

The ω-phase has first been discovered in metastable TiCr-alloys by Frost and co-workers in 1954[89]. Since then, it has been found to be the high-pressure equilibrium phase of the group IV metals (Ti, Zr, Hf)[90] and its presence been proven in alloys of these metals with various alloying elements under ambient pressure[9,91]. From a crystallographic point of view, the ideal ω-phase possesses hexagonal crystal structure, where the relations $a_\omega = \sqrt{2}a_\beta$ and $c_\omega = \frac{\sqrt{3}}{2}a_\beta$ hold between the lattice constants of the ω-phase and its parent β-phase (see Fig.5.3, lower part, left). According to this close relation between both structures, ideal ω-phase can be considered to be generated from the β-phase by a "collapse" of two neighbouring $[111]_\beta$-lattice planes into another giving a new middle plane as illustrated in Fig.5.3, lower part. Concerning the emergence of the ω-phase upon common heat treatments, as already mentioned, one differentiates between different *formation modes*. The immediate formation of the ideal or "commensurate" ω-phase is not encountered in the most cases, but rather intermediate versions of it with respect to the degree of lattice plane collapse (see Fig.5.3,

lower part, right), which are also termed as "incommensurate".

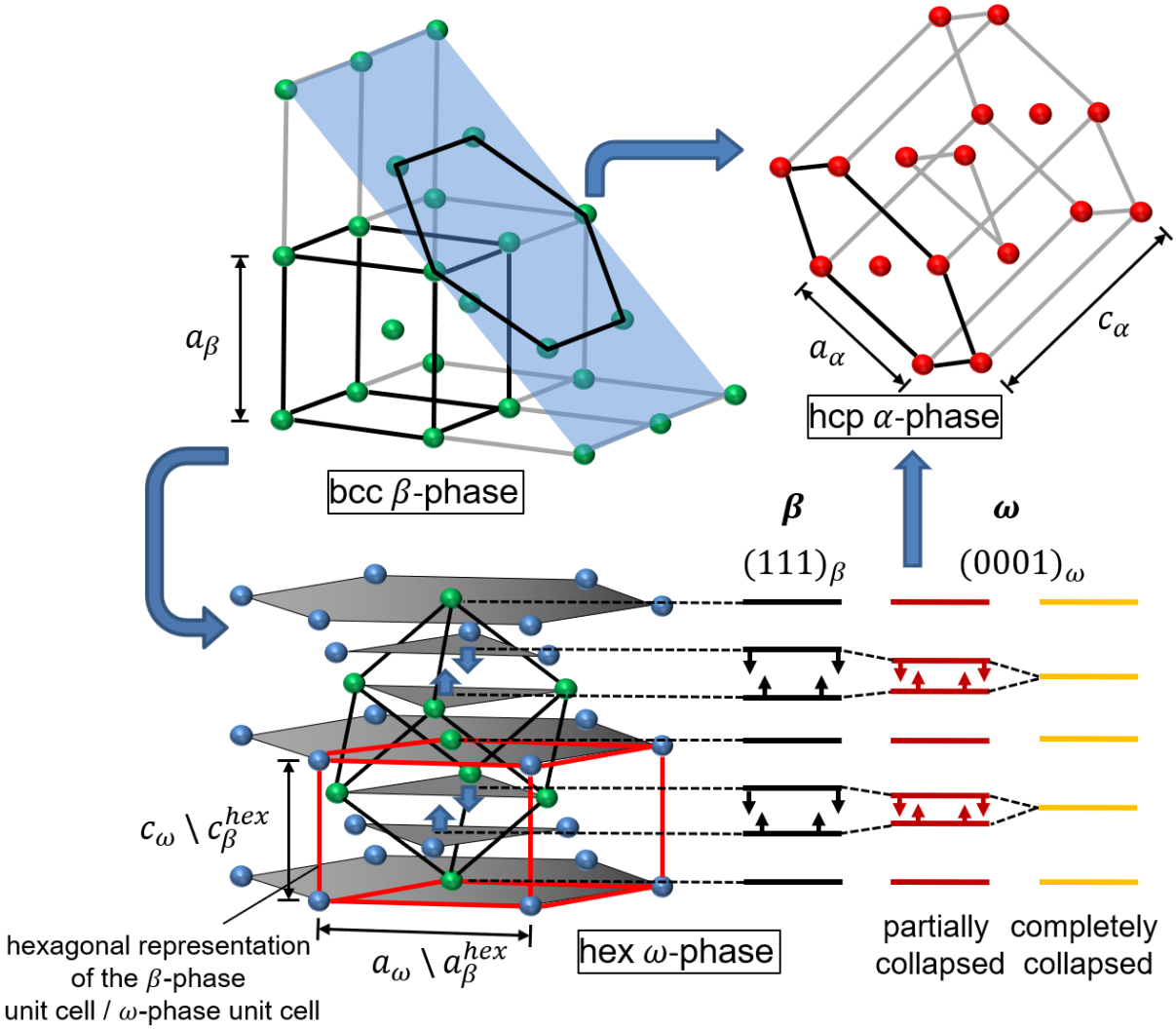

Figure 5.3: Lattice structure of bcc β-Ti (upper part, left) and its relationship to the lattice structures of the hcp α-phase (upper part, right) as well as to the lattice structure of the hexagonal ω-phase (lower part). β-to-ω-transformation can be understood as a partial/complete "collapse" of two neighbouring $[111]_\beta$-lattice planes into each other, as indicated by the arrows.[3]According to the close relationship between the β- and ω-phase, the hexagonal representation of the β-phase unit cell has been marked in red (lower part, left), which corresponds to the ω-phase unit cell, but without any collapse of [111]-lattice planes.

Which ω-formation mode takes place mainly depends on the overall alloy composition and on whether diffusion events can be included to happen or not. Distinction is made between the

[3]Note: In contrast to the hcp unit cell of the α-phase which is commonly assumed to be oriented as given by $\{110\}_\beta||\{0001\}_\alpha$ with respect to the β-phase matrix, the hexagonal ω-phase unit cell is commonly

- *athermal* formation mode, which is encountered during quenching, when undershooting the so-called athermal transformation temperature T_{ath} (see Fig.5.4(b), blue). Diffusion events can be excluded to be involved here due to the short time scales of quenching.

- *isothermal* formation mode which makes ω-particles nucleate and grow upon ageing at temperatures even far above T_{ath}, i.e., $T > T_{ath}$ (see Fig.5.4(b), green). Diffusion is known to play a decisive role here, i.e., the ageing temperature has to be notably larger than ambient temperature $T >> T_{amb.}$.

- *diffusionless-isothermal* formation mode, which has been discovered in the Ti-V-alloy system and explained just recently[88,92]. This kind of transformation has been found to happen upon isothermal ageing in the phase field slightly above T_{ath}, but at temperatures close to room temperature, i.e. $T \gtrsim T_{ath}$ and $T \approx T_{amb.}$, where again diffusion can hardly occur (see Fig.5.4(b), red).

For the sake of conciseness, ω-phase formed by the respective modes is addressed in the following as ω_{ath}-, ω_{iso}- and ω_{DI}-formation, whereby it is clear that there is only one kind of ω-phase.

In the contrary to phase formation processes taking place in e.g. aluminium alloys, where the precipitation stages are known to show well-determined compositions, the composition of ω-phase particles is known to evolve gradually after their formation. That means, their composition is similar to that of their parent β-phase in the beginning with the particles ejecting β-stabiliser into the surrounding matrix over the time period of ageing.

Athermal ω-phase formation:

As indicated by extensive diffuse streaking in diffraction diagrams, ω-phase inevitably forms when undershooting the athermal transformation limit T_{ath} even upon the most rapid quenching from solution annealing temperatures (see Fig.5.4,(a), formation mode in dark blue).

assumed to be oriented as given by $\{111\}_\beta||\{0001\}_\omega$ causing a difference in the number of atoms per unit cell and the size ratio of the hexagonal lattice parameters a and c to be opposite.

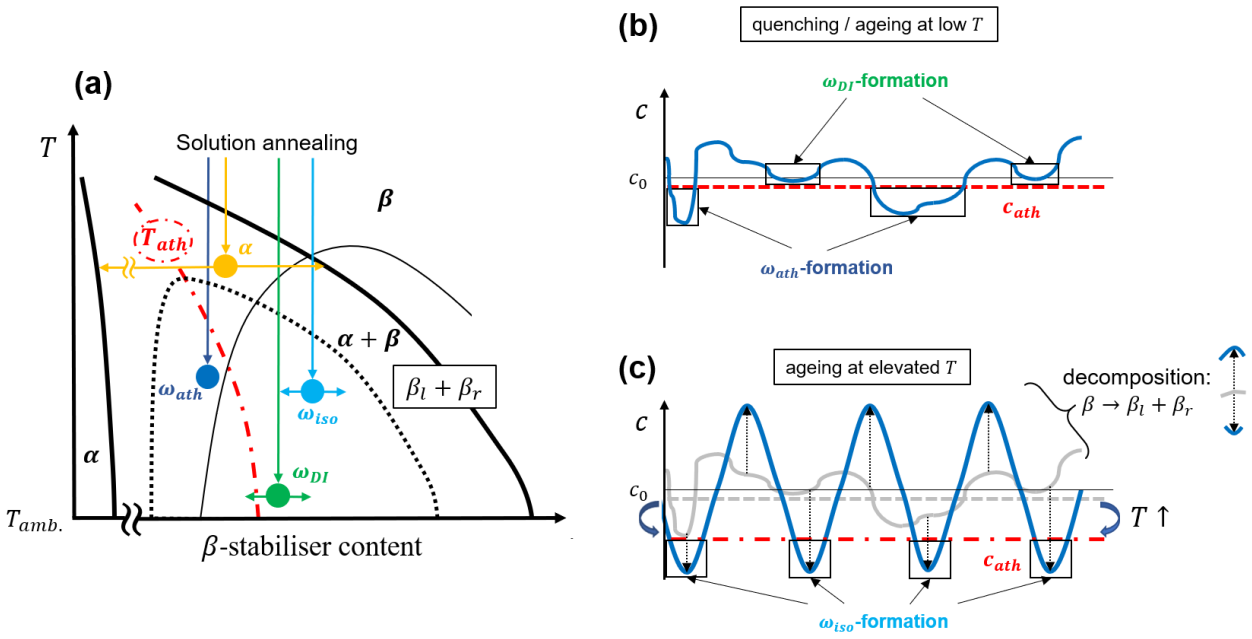

Figure 5.4: Localisation of the ω-formation modes in a schematic phase diagram and their explanation by means of compositional profiles. (a) When undershooting the athermal transformation limit T_{ath} during quenching, athermal ω-transformation happens (dark blue). When ending up in the phase field slightly above T_{ath} close to $T_{amb.}$ after quenching, ω_{DI}-formation happens during subsequent ageing (green). When ending up in the phase field far above T_{ath} at temperature, where notable diffusion is able to occur, and an underlying decomposition process is at work (black contour line), ω_{iso}-formation is favoured during subsequent ageing, which may eventually transform to the α-phase. Above the ω-formation range, α-phase is known to be formed instantaneously after quenching. (b) Possible compositional profile present during quenching/at low temperature ageing with the regions ready for ω_{DI}- and ω_{ath}-phase formation marked, determined by the position of c_{ath} (compositional limit corresponding to T_{ath}). (c) Change of the same compositional profile by an underlying decomposition process enabling ω_{iso}-formation. For increasing ageing temperatures, the critical concentration c_{ath} for athermal ω-formation is known to decrease, which means that V-lean regions of the original compositional profile are not ready for ω-transformation anymore. However, due to the increasing temperatures, an underlying decomposition process is found to provide regions lean enough in vanadium, i.e., with concentrations lower than c_{ath}, which are able to transform to ω.

Correspondingly, T_{ath} can be considered as the temperature, where half of the sample could potentially undergo ω_{ath}-transformation[92]. Since diffusion events can be excluded to contribute to this formation mode due to the short time scales, it is commonly termed as athermal in line with pre-martensitic transformations.

ω_{ath}-particles are found to be quite small with less than a few nanometres in size[93]. They

are known to inherit the concentration of their parent β-phase and contain partially collapsed neighbouring lattice plane pairs causing the diffuse streaking[94,95] (see Fig.5.3, lower part). The average degree of lattice plane collapse is known to increase with decreasing temperature and/or lower β-stabiliser content[96].

ω_{ath}-transformation of the β-phase is connected with a local softening of the longitudinal short-wavelength $\frac{2}{3}[111]_{\beta}$-phonon mode, which is potentially caused by lattice tensions and a locally reduced β-stabiliser content[92]. Regions with a locally reduced β-stabiliser content are unavoidably present due to quenching in concentration fluctuations, which are naturally found at solution annealing temperatures (see Fig.5.4,(b)). In this context, quenching to temperatures below T_{ath} is equivalent to these regions getting unstable because of undershooting the critical concentration corresponding to T_{ath} (red "c_{ath}"-line in Fig.5.4,(b)), where now, the aforementioned phonons are able to trigger this kind of transformation. As a result, certain accumulations of partially collapsed lattice plane pairs are stabilised permanently after this initial collapse, since they represent energetically favourable arrangements with respect to their electronic structure and morphology[97].

Isothermal ω-phase formation:

The formation of ω_{iso}-particles takes place during isothermal ageing in the phase field above T_{ath}, where diffusion can occur notably, but the direct β-to-α-transformation is yet not energetically favoured (see Fig.5.4(a), formation mode in light blue). The size of ω-phase particles formed by this kind of transformation mode is in the range of several 10 nm[98], where their shape is either ellipsoidal, spheric or cubic and may change upon ageing[99]. Diffuse ω-reflections, which are present in the beginning, develop into sharp peaks indicating a steady increase in the average degree of lattice plane collapse, which is accompanied and most likely connected to a steady ejection of β-stabiliser atoms from the ω-particles into the surrounding β-phase matrix replacing them by Ti-atoms[100,101].

Although this kind of *decomposition process* has been proven to happen by several investigation methods, there is some ongoing discussion about the precise nature of ω_{iso}-formation

and -evolution. Besides the possibility of growing from ω_{ath}-particles if present after quenching, commensurate ω_{iso}-phase is found to form by growing from a kind of incommensurate pre-phase which is termed "embryonic"[102]. Even if having been postulated more than half a century ago[103], no conclusive studies exist concerning the atomic structure and composition these embryonic particles so far.

It is assumed, that an underlying spinodal decomposition process of the β-phase matrix is steadily producing β-stabiliser lean regions, which represent potential sites for the formation of embryonic ω-phase (see Fig.5.4(c)). Uncertainty exists also about the evolution of embryonic ω-phase particles upon ageing: A first model assumes embryonic ω-particles to quickly grow in volume but not substantially changing their chemistry till reaching a certain size, where the transformation to commensurate ω_{iso}-phase is considered to occur, followed by a quick decrease in β-stabiliser content[86]. A second model assumes a gradual decrease of the β-stabiliser content going along with the completion of the lattice plane collapse. This mode has been denoted as a mixed-mode displacive-diffusive transformation[104,105].

Diffusionless isothermal (DI)-ω-phase formation:

The so-called diffusionless isothermal ω-formation mode has been discovered to take place upon isothermal ageing in the Ti-V-alloy system in the phase field slightly above T_{ath} close to $T_{amb.}$ (see Fig.5.4(a), formation mode in green). Because this kind of formation is proceeding at temperatures around $T_{amb.}$, diffusion can be excluded to be involved[106]. Again, as in case of ω_{ath}-formation, the longitudinal short-wavelength $\frac{2}{3}[111]_{\beta}$-phonon mode experiences local softening in β-stabiliser lean regions. These regions are, however, not unstable enough to transform already during quenching, but only during subsequent ageing[88,92], since they lay slightly above the critical concentration for the transformation corresponding to T_{ath} (red line in Fig.5.4,(b)). In contrast to ω_{ath}-formation, the surroundings of local β-stabiliser lean regions are more stable because the alloy lies as a whole in the phase field above T_{ath}. As a consequence, the degree of local softening is found to decrease, which is equivalent to a strong increase in the ω/β-interface energy to be overcome in the course of nucleation, causing the

DI-ω-formation mode to not proceed during quenching, but bit by bit during isothermal ageing. ω_{DI}-formation is predicted to occur only in a narrow phase field. It should neither be observed at temperatures substantially lower than $T_{amb.}$ (with the alloy being still in the phase field close to but above T_{ath}) since the ω-lean regions are not in resonance with the phonons inducing the collapse as shown by internal friction measurements[92,107]. At temperatures substantially larger than $T_{amb.}$, but with the alloy again being in the phase field close to T_{ath}, the ω/β-interface energy has been found to have strongly increased impeding this mode of ω-formation to proceed.

α-phase formation:

Independent of the preceding mechanism having led to its formation, ω-phase is found to directly transform to the equilibrium α-phase (see Fig.5.3) within time spans accessible at elevated temperatures[86]. At even higher temperatures, direct transition from unstable β-phase present after quenching to the α-phase may be found to occur (see Fig.5.4(a), formation mode in orange).

It is well-known, that the α-phase forms via a nucleation and growth process from existing ω-phase particles, where the exact characteristics of both processes, however, seem to be strongly dependent on the precise alloy composition. In systems featuring comparably low misfit in between β-stabiliser lean ω-phase and the surrounding β-phase matrix, α-phase nucleates either inside ω-particles[108], at a certain distance from them[109], or at the ω/β-interface[110]. Which locations are preferred is likely to vary with the presence of certain (minor) alloying elements. In case of high misfit alloys including the Ti-V-samples investigated hereinafter, α-phase is found to nucleate at the ω/β-interface[99]. Upon their growth, α-phase particles are known to absorb the ω-phase, forming small platelets accompanied by a further ejection of β-stabiliser into the surrounding β-matrix[86]. In this context, oxygen being located at the ω/β-interface is known to facilitate α-phase formation or even making it possible at all.

5.1.3 The Ti-V-alloy system

Vanadium is one typical, if not the most important β-stabiliser used for alloying, since it is part of the most commonly used Ti-6Al-4V-alloy. Although Ti-V-alloys without other alloying elements are only used rarely, it is important to know about such more "simple" systems in order to ensure a proper basis for the understanding of more complicated alloying systems. Concerning the Ti-V-phase diagram, confusion regarding its exact shape has consisted over decades (see Fig.5.5, dashed red lines and black solid line). This was found to be caused by oxygen impurities in particular, which are an inevitable component in commercial Ti-alloys, since titanium, independent of whether being in its α- or β-phase, possesses a strong affinity and large solubility for oxygen[111]. In general, oxygen is known to increase both the β- and the α-transus-temperature. The most prominent difference, however, is the miscibility gap caused by the mono-eutectic reaction $\beta \rightarrow \beta_l + \beta_r$, i.e., the decomposition of the β-phase into V-lean regions β_l and V-rich regions β_r, which is stable in case of oxygen additions being present (red-dashed lines in Fig.5.5) and metastable otherwise (black solid lines). The phase lines drawn in solid black have been obtained by Lindwall and co-workers by applying the "CALculation of PHAse Diagrams method" (CALPHAD)[87]. Since real samples, as the ones investigated hereinafter contain always a certain amount of oxygen, the red-dashed phase diagram in Fig.5.5 is more appropriate to be used.

The phase diagram shown in this figure is an equilibrium phase diagram, so no information concerning metastable phases could normally be obtained from it. For this purpose, the athermal transformation limit T_{ath} as determined for the Ti-V-system by Tane and co-workers[88], featuring a finite oxygen content, has been drawn into Fig.5.5 (dash-dotted red line). Additionally, the nominal compositions of the samples investigated hereinafter (black vertical line, "21 at%V") as well as of samples important for the subsequent discussion (black vertical line, "19 at%V") have been marked. In this context, exact knowledge about the position of T_{ath} is important in order to decide about the positions of the phase fields, where the different kinds of ω-formation mechanisms will be observed in an alloying system.

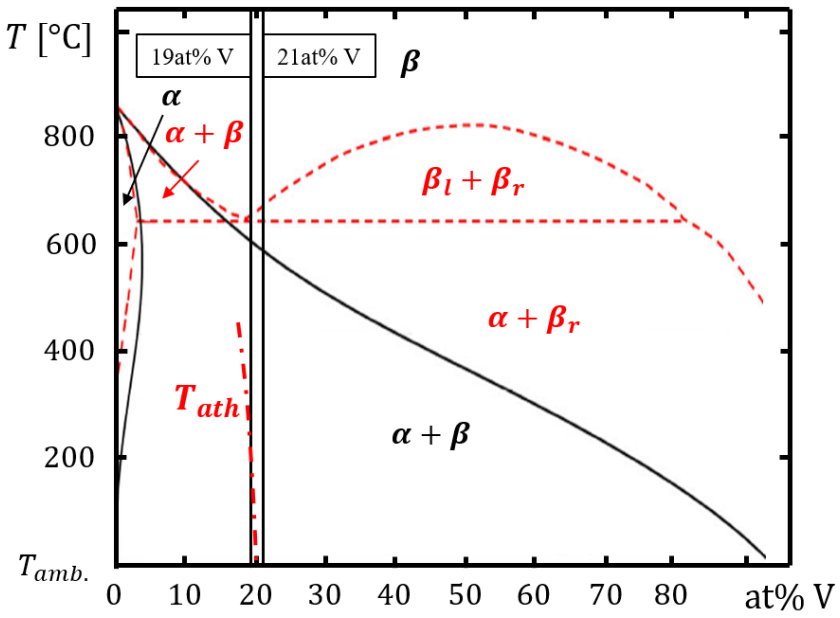

Figure 5.5: Phase diagram of the Ti-V alloy system according to[87]. The black solid lines outline the phase diagram predicted for zero oxygen content. The red dashed lines represent the phase diagram of the alloy system comprising a finite oxygen content as found in commercial Ti-alloys. Here, the phase diagram constitutes a phase field, where decomposition into V-lean and V-rich β-phase regions is favoured. Additionally, the limiting curve for athermal transformation T_{ath} (dash-dotted red curve, as determined by Tane and co-workers[88] for the TiV-alloy system) as well as compositions of 19 at%V and 21 at%V (vertical black lines) have been drawn into the graph.

In Sect.5.1.2, the conditions for the different ω-formation modes to take place have been described. In this specific case, upon quenching to temperatures larger than $T_{amb.}$, the alloy stays in the phase field above T_{ath}, so ω_{ath}-formation will not happen during quenching. This is indicated by the vertical black line for the nominal alloy composition in Fig.5.5 not intersecting T_{ath}. Since after quenching to $T_{amb.}$, the alloy is in a state in the phase field directly above T_{ath}, the preconditions for the ω_{DI}-formation are fulfilled, which forms from β_Q, the quenched-in β-phase, according to

$$\beta_Q \rightarrow \beta_r + \omega_{DI}. \tag{5.1}$$

Since in general, ω-phase ejects V-atoms into the surrounding matrix exchanging them by

Ti-atoms, the β-phase matrix gets enriched and is thus denoted as β_r.[4] By quenching to temperatures markedly exceeding $T_{amb.}$, i.e., to temperatures around and higher than 300 °C, the conditions for ω_{DI}-formation are not fulfilled anymore. Since notable diffusion is able to occur at these temperatures, instead, the decomposition process of the β-phase matrix is found to proceed. Thus, the conditions for ω_{iso}-formation are met, which may eventually transform to the α-phase according to

$$\beta_Q \rightarrow \beta_l + \beta_r \rightarrow \omega_{iso} + \beta_r (\rightarrow \alpha + \beta_r). \tag{5.2}$$

5.2 Motivation

There exists only a minute number of publications, where continuous kinetic measurements concerning ω-formation and ω-to-α-transformation, are described. In the by far largest part of publications, statements are derived from snapshots recorded by direct imaging techniques and results from indirect methods logically deducing, what happens in between, but what is likely to be one reason for the partly contradictory results.
The motivation to perform the measurements presented hereinafter can thus be summarised as follow:

- Opening up dilatometry as a method of choice to investigate ω-phase formation and ω-to-α-transformation.
- Investigation of the ω-phase formation kinetics taking place during isothermal ageing, especially close to $T_{amb.}$, where ω_{DI} as a new kind of ω-formation mechanism was found recently.
- Investigation of ω-to-α-transformation by dilatometry.

[4] Note: V-enriched β-phase, β_r, is generated, on the one hand, by the underlying decomposition process $\beta \rightarrow \beta_l + \beta_r$ and, on the other hand, by ω-phase formation, where the ω-phase particles are known to eject V-atoms into the surrounding matrix exchanging them by Ti-atoms.

- Clarification of the influence of oxygen on both ω-phase formation and ω-to-α transformation kinetics.

5.3 Experimental

Two TiV-samples comprising a nominal composition of 21 at% V, but with different oxygen contents have been investigated. In order to produce these samples, two sets of starting materials have been prepared by arc-melting and tilt-casting: (i) 99.9 wt% purity Ti and 99.7 wt% purity V with no regard to the oxygen content, (ii) 99.999 wt% high purity Ti and 99.7 wt% purity V with an oxygen content lower than 0.1 at%. Mixing the respective starting materials together, the final composition of the alloys prepared have been determined by inductively coupled plasma-optical emission spectrometry (ICP-OES, IRIS Advantage DUO, Thermo Fisher Scientific Inc., USA) with respect to Ti and V, and, with respect to their oxygen content, by an oxygen/nitrogen elemental analyser (TC-436, LECO Corp., USA). The samples for the dilatometer were prepared to have cylindrical shape comprising a nominal diameter of 5.6 mm and a length of 20.0 mm. The production of the samples and their analysis with respect to their exact compositions has already been described elsewhere [107]. The grain structure of the samples turned out to be just discernible with the naked eye and can thus be assumed to amount to the fraction of a millimetre.

The sample produced from the less pure components has been analysed to possess 20.9 at%V with about 1 at%O, which is a common oxygen content for titanium alloys. Hereinafter, it will be termed as Ti20.9V and addressed as "the sample with a regular oxygen content". The sample produced from the high-purity components has been analysed to possess a composition of 21.3 at%V with only about one tenth of the oxygen content compared to the first one, amounting to 0.1 at%O. Correspondingly, it will be termed as Ti21.3V(HP) and be referred to as "the sample with strongly reduced oxygen content". Right after their production, the samples were subjected to a solution treatment at 800 °C for 2 h at a pressure of $1.0 \cdot 10^{-5}$ mbar, followed by quenching in ice water. This was done in order to avoid any

irreversible processes disturbing the investigations of phase formation processes taking place at ageing temperatures substantially lower than 800 °C, as they are described hereinafter.
Dilatometric measurements have been performed for various ageing temperatures in the range of 41 °C to 450 °C in case of the Ti20.9V-sample as well as in the range of 100 °C to 450 °C in case of the Ti21.3V(HP)-sample under high vacuum conditions ($1.0 \cdot 10^{-5}$ mbar) using the laser dilatometer described above (see Sect.3.1). Prior to each measurement, the samples have been solution annealed in situ at 880 °C until length did not change anymore suggesting the sample to be fully in the β-phase, which took at least 45 min. Direct quenching to the respective ageing temperatures has been performed in a He-gas stream yielding a quenching rate of approximately 35 $\frac{\mathrm{K}}{\mathrm{s}}$. After every second measurement, an ageing measurement at 300 °C has been performed. By checking its congruency with the preceding ageing measurements recorded at this temperature, any device-related errors, long-term effects or irreversible changes of the sample could be excluded.

5.4 Results

In this section, the data obtained are presented and described qualitatively in detail. A quantitative analysis and the derivation of tools allowing to perform it, are given in the following section.
By dividing the measured absolute length changes ΔL by the sample length L_0, relative length changes $\Delta L/L_0$ are obtained, which are independent of the original sample length and thus appropriate for comparison. Considering the length changes occurring as a consequence of phase formation or transformation processes, their comparison enables a first assessment with respect to different phase regions. Such assessment is based on the fact, that, in general, the formation of different phases will show length changes different in size and sign and that the length changes appearing are roughly proportional to the phase fraction formed.
Following this procedure, Fig.5.6 shows $\Delta L/L_0$ recorded for both samples investigated for all ageing temperatures in the range up to 350 °C for time spans up to 10^5 s ($\sim$ 28 h).

Length changes are found to be negative. This indicates the formation of one and the same phase but at varying extent or manifestation, probably as a consequence of different ageing temperatures. Fig.5.7 shows $\Delta L/L_0$ for all ageing temperatures in the range of 300 °C to

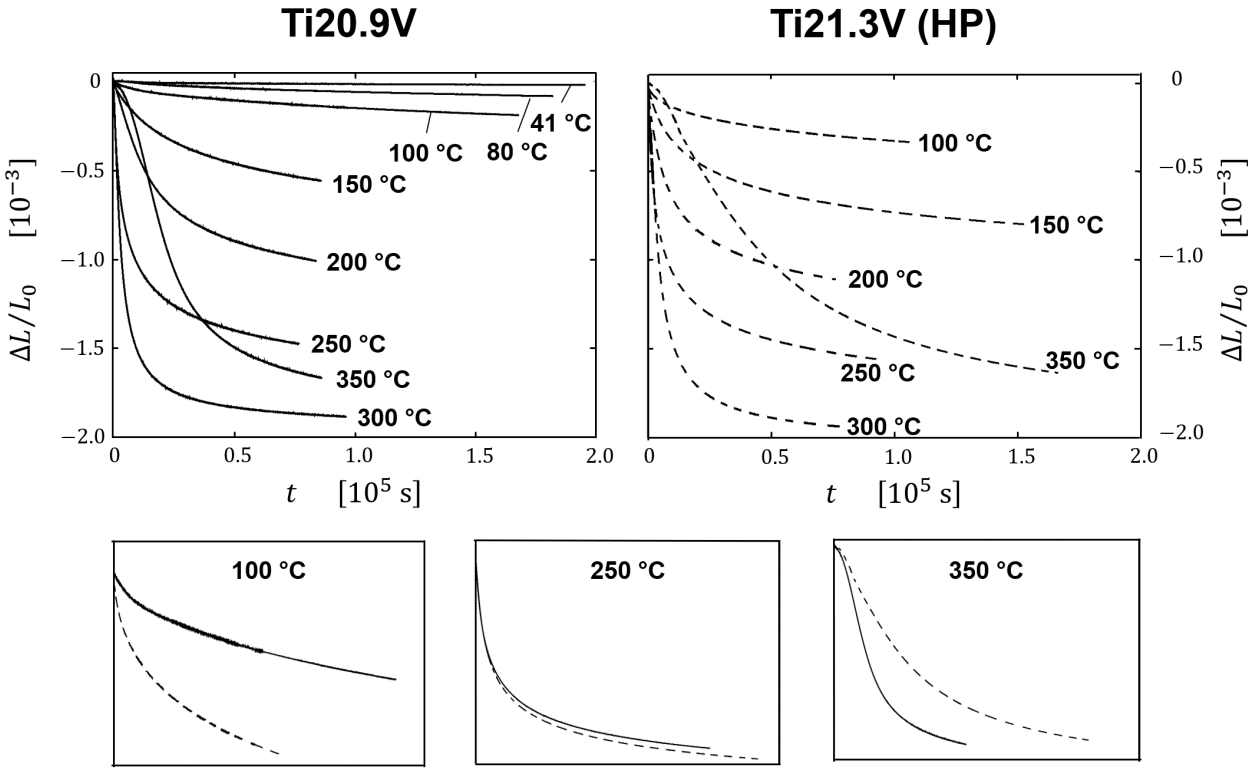

Figure 5.6: Relative length change $\Delta L/L_0$ measured over time t upon isothermal ageing at various temperatures in the range till 350 °C of the sample with a regular oxygen content (left, full lines, Ti 20.9V) and the sample with a strongly reduced oxygen content (right, dashed lines, Ti 21.3V(HP)). To allow better comparison and make differences in kinetics more obvious, the curves for both samples are shown together for three selected temperatures (100 °C, 250 °C, 350 °C) in the panels in the lower part of the chart.

450 °C again for time spans up to 10^5 s, where the negative length changes are moderated or even followed by positive ones which are likely to be caused by the transformation of the first phase to a second one.

Taking a closer look, the maximum absolute relative length change at first grows for both samples along with increasing ageing temperature in the range till 350 °C, i.e. till 250 °C or 300 °C. In case of ageing at 350 °C, however, it is clearly reduced again compared to the measurements at 300 °C. As can be determined by scaling the curves roughly to their

respective maximum value, correspondingly, the time constants are decreasing till 300 °C and increasing likewise again for the ageing temperature of 350 °C.

As illustrated by the graphs in the lower part of Fig.5.6, kinetics for the sample with reduced oxygen content (dashed lines) seem to be accelerated at temperature lower than 250 °C, i.e., larger relative length changes are obtained at shorter time scales. At 250 °C, the curves agree again quite well in time constant and maximum relative length change reached, whereas at 350 °C, kinetics seem to be accelerated for the sample with regular oxygen content (solid lines).

As becomes evident by comparing the shape of the curves at different temperatures, it changes from an approximately exponential decay at low temperatures, where the slope is largest at the beginning of the isothermal treatment diminishing over time to a shape, where the slope is largest in the intermediate section of the measurement (see measurements at 100 °C and 350 °C in Fig.5.6), i.e., there seems to be a (small) initial plateau region.

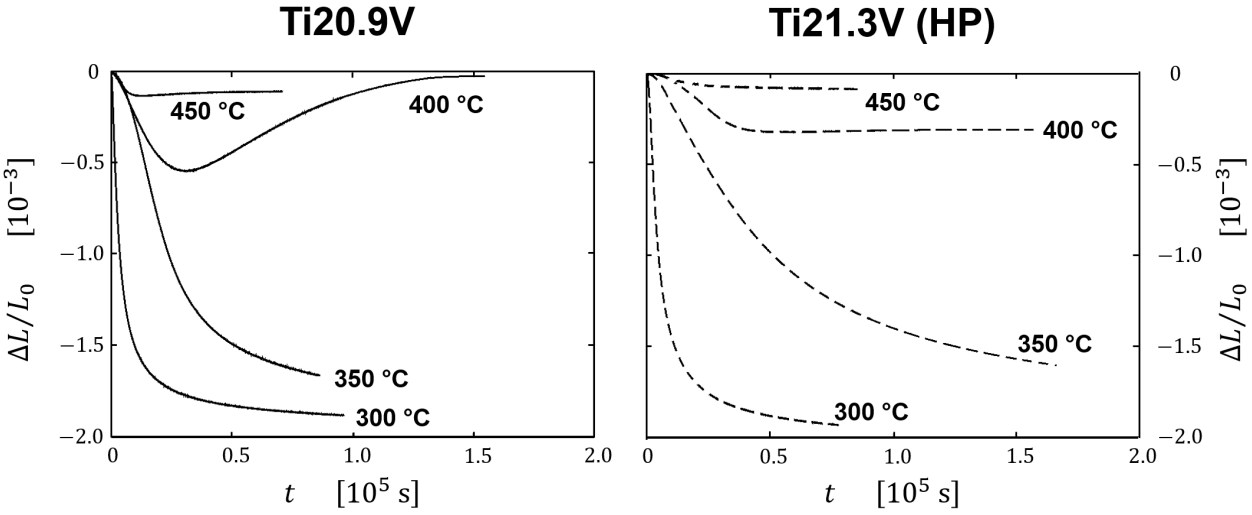

Figure 5.7: Relative length change $\Delta L/L_0$ measured over time t upon isothermal ageing at various temperatures exceeding 300 °C of the sample with a regular oxygen content (left, full lines, Ti 20.9V) and the sample with a strongly reduced oxygen content (right, dashed lines, Ti 21.3V(HP)).

In Fig.5.7, the measurements obtained for ageing at 300 °C and 350 °C are shown again together with the measurements obtained for 400 °C and 450 °C. Here, the most obvious

feature certainly is the strong positive length change following the preceding negative one upon ageing at 400 °C for the sample with a regular oxygen content, indicating some kind of consecutive reaction, as mentioned above. This reaction may appear even at 450 °C, but appears much less pronounced. Interestingly, no distinct positive length change following the negative one is observed in case of the sample with a strongly reduced oxygen content, but nevertheless, the strong length decrease seems to be clearly moderated. Additionally, the aforementioned plateau region in the beginning does also appear in case of ageing at temperatures above 350 °C and seems to be more strongly pronounced in case of the samples with reduced oxygen content.

Speaking generally, the length changes recorded are remarkable for at least two reasons: First, notable length changes are measured even at ageing temperatures close to $T_{amb.}$, which is not evident a priory since all thermally activated processes as, e.g., diffusion being suppressed at such low temperatures. Second, the length changes are huge, i.e., the maximum relative length change of about $2 \cdot 10^{-3}$ measured for samples with a length of 2 cm corresponds to 40 μm, which is the thermal expansion to expect upon *heating* the very sample for about 250 °C.

5.5 Data analysis

This section consists of three parts: In order to give a proper interpretation of the dilatometric measurement curves obtained, formulae are derived in the first part (Sect.5.5.1) enabling the length changes appearing on the macroscopic scale to be understood as a consequence of concomitant changes happening on the microscopic scale. In the second part (Sect.5.5.2), the applicability of the formulae derived is verified. This is done calculating the length changes to be expected based on data concerning the changes occurring on the microscopic scale from literature and comparing them to the measured length changes. Finally, in the third part (Sect.5.5.3), the formulae derived are used in order to qualitatively and quantitatively analyse the measurements obtained in detail.

5.5.1 Modelling the length changes upon decomposition, ω-phase formation and ω-to-α-transformation

As described in Sect.5.1.3, the processes to be observed during ageing are ω_{DI}-phase formation at ageing temperatures close to $T_{amb.}$, ω_{iso}-phase formation with a preceding decomposition process at elevated ageing temperatures, and, at even higher temperatures, ω-formation and subsequent ω-to-α-transformation.

In order to give a proper quantitative and qualitative interpretation of the measurements obtained, formulae have to be derived for the length changes to be expected accompanying these phase formation or transformation phenomena. This is done by applying the common approximation $\frac{\Delta L}{L_0} \approx \frac{1}{3}\frac{\Delta V}{V_0}$ (see Sect.2.3). The applicability of this approximation is justified, on the one hand, since the maximum length changes observed under isothermal conditions are in the range of 10^{-3} and thus by several orders of magnitude smaller than the sample length of 2 cm, and, on the other hand, since also the grain size is small compared to its dimensions making the sample appear isotropic. $\Delta V/V_0$ is deduced in the following by considering changes in the atomic volumina occurring upon structural transformation.

The relative length changes to be expected are calculated by assuming ...

- ... the whole sample to be initially in the same phase with a composition of c_0 everywhere featuring an average atomic volume v_0,
- ... several phases to be formed with phase fractions x_{pi} and corresponding average atomic volumina v_{pi} replacing the phase state of the sample in its initial state,
- ... and the average atomic volumina v_{pi} of the phases to be functions of the average local vanadium content $c_{V,pi}$ and of temperature T.

Summing up the relative volumetric changes caused by the freshly formed phases with respect

to the initial atomic volume weighted by their respective phase fractions yields:

$$\frac{\Delta L}{L_0} \approx \frac{1}{3}\frac{\Delta V}{V_0} = \frac{1}{3}x_{p1}\frac{v_{p1}(c_{V,p1},T)-v_0}{v_0} + \frac{1}{3}x_{p2}\frac{v_{p2}(c_{V,p2},T)-v_0}{v_0} + ... \ . \tag{5.3}$$

Since the absolute particle number and the overall V-concentration c_0 remain unchanged by the phase formation processes, there are two conditions which have to be fulfilled, concerning, on the one hand, the phase fractions and, on the other hand, the phase fractions in combination with the respective concentrations:

$$x_{p1} + x_{p2} + ... = 1, \tag{5.4a}$$

$$x_{p1}\, c_{V,p1} + x_{p2}\, c_{V,p2} + ... = c_0. \tag{5.4b}$$

These rather general considerations shall be applied in the following to the specific phase formation and transformation processes known to occur in the samples investigated.
The relative length changes presented in Figs.5.6 and 5.7 are counted from the state which is present right after quenching. Here, the sample is fully in the β-phase which is thus designated as β_Q. Its compositional profile is rather homogeneous comprising only minute concentration fluctuations which have been introduced by quenching from solution annealing temperatures, where such compositional variations occur naturally. For the purpose of modelling, the samples are assumed to show a homogeneous concentration profile everywhere in the beginning, i.e. the V-concentration amounts to 21 at%V at any point.[5] The atomic volume in this configuration is designated as $v_{\beta,0}$. With respect to the phase state being present after an arbitrary time period of ageing, three cases are considered in the following, which may appear concurrently:

i. Mere decomposition: $\beta_Q \rightarrow \beta_l + \beta_r$, with the atomic volumina $v_{\beta\text{-lean}}$ and $v_{\beta\text{-rich}}$, corresponding mole fractions $x_{\beta\text{-lean}}$ and $x_{\beta\text{-rich}}$ as well as average concentrations of

[5] The approximation of a completely homogeneous compositional profile is justified in detail in the next section.

$c_{V,\beta\text{-lean}}$ and $c_{V,\beta\text{-rich}}$ of the phases present upon ageing.

ii. ω-phase formation: $\beta_Q \rightarrow \omega + \beta_r$, with the atomic volumina v_ω and $v_{\beta\text{-rich}}$ and corresponding phase fractions x_ω and $x_{\beta\text{-rich}}$ as well as average concentrations $c_{V,\omega}$ and $c_{V,\beta\text{-rich}}$ of the phases present upon ageing. The preceding decomposition process as happening in case of ω_{iso}-formation is discussed separately in (i.).

iii. ω-to-α-transformation: $\beta_r + \omega \rightarrow \beta_r + \alpha + \omega$, with the atomic volumina $v_{\beta\text{-rich}}$, v_ω and v_α and the corresponding phase fractions $x_{\beta\text{-rich}}$, x_ω and x_α as well as average concentrations $c_{V,\omega}$ and $c_{V,\beta\text{-rich}}$ of the phases present upon ageing. The V-concentration of α-phase particles is known to be rather close to zero[112,113], so $c_{V,\alpha} = 0$ is assumed in the following.

In order to calculate the atomic volumina of the phases appearing, their lattice constants are used, which are a function of the local V-content and of temperature. Fig.5.8 shows the lattice constants a_ω and c_ω of hexagonal ω-phase (blue) together with $a_\beta^{hex} = \sqrt{2}a_\beta$ and $c_\beta^{hex} = \frac{\sqrt{3}}{2}a_\beta$ (see Fig.5.3), i.e., the lattice constants of bcc β-phase (black) in hexagonal representation, which are used for the sake of a better comparability. The dependence of the β-phase lattice constants on the V-content has been drawn according to a linear relation provided by Aurelio and co-workers[114], which has been developed based on a rather comprehensive collection of lattice constants data concerning the Ti-V-system. Again based on the lattice constant data compiled by Aurelio and co-workers[114], the curves for lattice constants of the ω-phase have been inserted. Additionally, the lattice constants of the α-phase, which appear as points on the y-axes because of the virtual insolubility of vanadium in it, have been added (red arrows, according to[115]). The specific values and expressions for the lattice constants are further discussed in the following.

All lattice constants presented in Fig.5.8 have been obtained at $T_{amb.}$. Since ageing is performed mainly at temperatures exceeding $T_{amb.}$, however, thermal expansion has to be included in order to obtain the lattice constants at varying ageing temperatures, in particular,

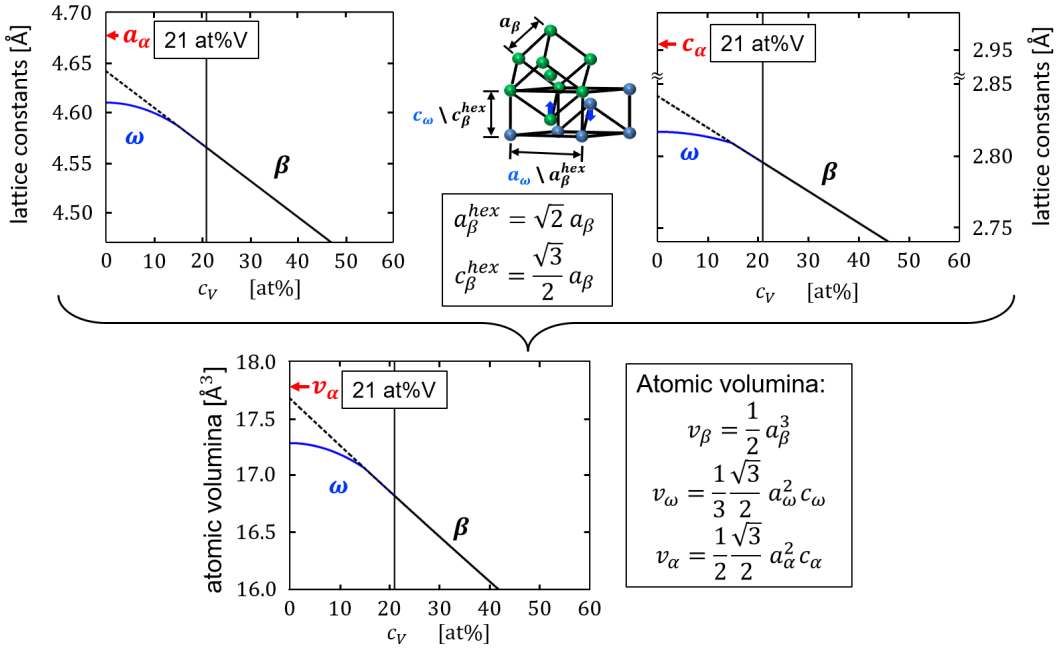

Figure 5.8: Dependence of the lattice constants and based on them of the volumina on the V-content at $T_{amb.}$ for the different phases appearing in the Ti 21at%V-alloy, i.e., the bcc β-phase according to[114], hexagonal ω-phase according to[114] and hcp α-phase according to[115]. In order to ensure comparability of the lattice constants, that ones of bcc β are plotted in hexagonal representation according to the illustration of the lattice structures in the middle (see also Fig.5.3). The atomic volumina have been calculated by using the formulae in the box in the lower part of this figure. Since the α-phase possesses no solubility for vanadium, its lattice constants and atomic volume are given by points on the y-axes of the plots.

since it slightly varies dependent on the local V-content. An expression for the thermal expansion coefficient of pure titanium has been derived based on the data provided by Hidnert in the range of $0 - 625\,^{\circ}\mathrm{C}$[116], reading

$$\alpha_{Ti}(T) = 8.45 \cdot 10^{-6} + 5.93 \cdot 10^{-9}\, T. \tag{5.5a}$$

For pure vanadium, an expression has been derived based on the data provided by Kozlovskii and co-workers in the range of $0 - 726\,^{\circ}\mathrm{C}$[117], reading

$$\alpha_{V}(T) = 8.73 \cdot 10^{-6} + 3.42 \cdot 10^{-9}\, T. \tag{5.5b}$$

Furthermore, by applying Vegard's rule[118], a factor $\gamma(c_V, T)$ to be multiplied with the lattice constants accounting for the thermal expansion as a function of the local V-content is obtained,

$$\gamma(c_V, T) = 1 + (1 - c_V) \cdot \int_{T_{amb.}}^{T} \alpha_{Ti}(\tilde{T})\, \mathrm{d}\tilde{T} + c_V \cdot \int_{T_{amb.}}^{T} \alpha_V(\tilde{T})\, \mathrm{d}\tilde{T}, \tag{5.6}$$

which has to be used when performing any calculations for temperature other than $T_{amb.}$.

Mere decomposition according to (i.):

As described above, decomposition of the β-phase into V-lean and V-rich regions is obligatory for subsequent ω_{iso}-phase formation and is thus important to be discussed with respect to potential length changes produced. The lattice constant a_β of the β-phase (and thus also a_β^{hex} and c_β^{hex}) are known to vary linearly with the local V-content (see Fig.5.8). Speaking more specifically, a_β increases with decreasing V-content according to the relation[114]

$$a_\beta(c_V, T)[\text{Å}] = \gamma(c_V, T) \cdot \left\{3.282 - 2.57 \cdot 10^{-3} \cdot c_V[\text{at\%}]\right\}, \tag{5.7}$$

where the factor $\gamma(c_V, T)$ (Eq.5.6) has been added to account for the effects of thermal expansion. According to this relation and to the volumetric calculations presented in Fig.5.8, lower part, V-lean regions expand and V-rich regions contract around them.

In the case of mere decomposition taking place, Eq.5.3 turns into

$$\begin{aligned}\left(\frac{\Delta L}{L_0}\right)_{\text{decomp.}} &\approx \frac{1}{3} \cdot \left(\frac{\Delta V}{V_0}\right)_{\text{decomp.}} \\ &= \frac{1}{3} \cdot x_{\beta\text{-lean}} \left(\frac{v_{\beta\text{-lean}}(c_V, T)}{v_{\beta,0}} - 1\right) + \frac{1}{3} \cdot (1 - x_{\beta\text{-lean}}) \left(\frac{v_{\beta\text{-rich}}(c_V, T)}{v_{\beta,0}} - 1\right) \\ &= \left(\frac{\Delta L}{L_0}\right)_{\beta\text{-lean}} + \left(\frac{\Delta L}{L_0}\right)_{\beta\text{-rich}},\end{aligned} \tag{5.8}$$

where in between phase fractions and concentrations, the two relations analogous to the

Eqs.5.4 hold:

$$x_{\beta\text{-lean}} + x_{\beta\text{-rich}} = 1 \tag{5.9a}$$

and

$$c_{V,\beta\text{-lean}} \cdot x_{\beta\text{-lean}} + c_{V,\beta\text{-rich}} \cdot x_{\beta\text{-rich}} = c_0. \tag{5.9b}$$

In order to calculate the atomic volumina by using the lattice constants,

$$v_\beta = \frac{1}{2} a_\beta^3(c_V, T) \tag{5.10}$$

is applied, where the pre-factor 1/2 accounts for the number of atoms per β-phase unit cell. To get an impression of the relative length changes which are to be expected upon such decomposition processes taking place, Eq.5.8 in combination with Eqs.5.7, 5.9 and 5.10 are used to calculate the length changes in dependence of the β_l-fraction $x_{\beta\text{-lean}}$ for different degrees of decomposition, i.e., different values for $c_{V,\beta\text{-lean}}$ in the range of $10 - 18\,\text{at}\%$. The results are presented in Fig.5.9 (black curves). As can be seen, the relative length changes are slightly positive in each case, where only for fractions of V-lean regions substantially larger than 50 % (vertical dotted line), the length changes get really visible. Nevertheless, the relative length changes measured get visibly larger for a larger degrees of decomposition.

To sum up, as an important result, **mere decomposition of the β-phase leads to tiny positive length changes.**

In order to be able to grasp the most important aspects of the decomposition process, Fig.5.10 shows a schematic illustration of it, which breaks down the different contributions to the overall length changes.

ω-phase formation according to (ii.):

As described, ω-phase formation is encountered in two different modes for the alloy investigated. Firstly, ω_{iso}-formation is found to be at work at elevated temperature, where an

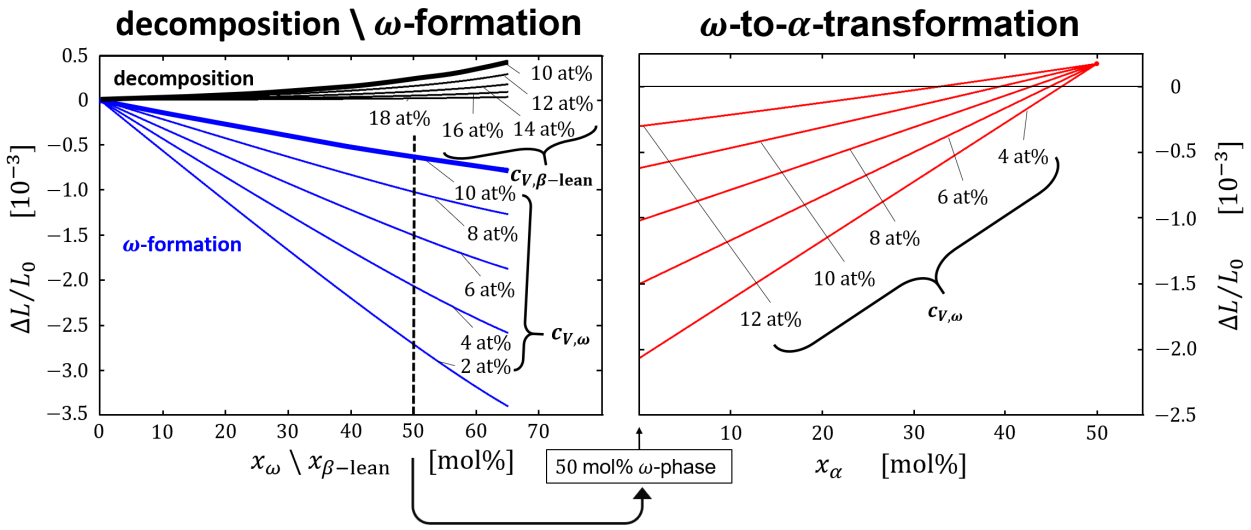

Figure 5.9: (a) Relative length changes calculated for mere decomposition and ω-phase formation in dependence of the phase fractions of V-lean β-phase regions $x_{\beta\text{-lean}}$ and ω-phase particles x_ω, respectively. The calculations have been performed for different degrees of decomposition, i.e., V-content of the V-lean β-phase regions $c_{V,\beta\text{-lean}}$ and ω-phase particles $c_{V,\omega}$, respectively. The results have been obtained by combining Eq.5.8 with Eqs.5.7, 5.9 and 5.10 in case of mere decomposition as well as by combining Eq.5.12 with Eqs.5.11, 5.13, 5.14 and 5.10 in case of ω-phase formation. For the sake of better comparability, the curves for mere decomposition and ω-formation to equal concentrations $c_{V,\beta\text{-lean}} = c_{V,\omega} = 10\,\text{at\%}$ are plotted in bold type. (b) Relative length changes calculated for ω-to-α-transformation in dependence of the α-phase fraction x_α formed, where the initial state consists of 50 mol% ω-phase at different V-concentrations $c_{V,\omega}$ surrounded by a β-phase matrix. The calculations have been performed by applying Eq.5.16 in combination with Eqs.5.15, 5.17, 5.14 and 5.10. All calculations have been performed at $T_{amb.}$.

ongoing spinodal decomposition process generates V-lean regions which transform into ω-phase particles. On the other hand, ω_{DI}-formation is found to happen at ageing temperatures close to $T_{amb.}$, where quenched-in V-lean regions are less stable due to the low temperatures and gradually transform into the ω-phase without preceding decomposition (see Sect.5.1.2). Even if the specific formation mechanisms vary, this has no influence on the length changes caused by the transformation of a certain fraction of the β-phase to the ω-phase. As can be seen in Fig.5.8, the lattice constants of hexagonal ω-phase evolve gradually from that of the β-phase (in hexagonal representation) and eventually fall below them for decreasing V-concentrations. For concentrations lower than approximately 15 at%V, the ω-phase lattice

constants start to deviate markedly from that of the β-phase and are given by:

$$a_\omega(c_V, T)[\text{Å}] = \gamma(c_V, T)\left\{4.6100 - 1.0250 \cdot 10^{-4} \cdot c_V^2[\text{at\%}]\right\} \tag{5.11a}$$

and

$$c_\omega(c_V, T)[\text{Å}] = \gamma(c_V, T)\left\{2.8170 - 0.3544 \cdot 10^{-4} \cdot c_V^2[\text{at\%}]\right\}. \tag{5.11b}$$

Both expressions have been obtained by fitting the data given by [114] using a quadratic function which has been found to reproduce their behaviour satisfactorily well. Again, in order to account for the thermal expansion of the lattice, the factor $\gamma(c_V, T)$ (Eq.5.6) has been multiplied.

Upon their formation, ω-phase particles are known to get leaner in vanadium and the surrounding β-phase matrix to enrich in vanadium in contrast. This is equivalent to the β-phase contracting around the ω-phase particles. The ω-phase particles, however, do not expand as strongly as V-lean β-phase regions would do, hence the contraction of the β-phase matrix surpasses the expansion of ω-phase particles in this case, as becomes also clear from the volumetric calculations presented in the lower part of Fig.5.8

In this particular case, Eq.5.3 turns into:

$$\begin{aligned}\left(\frac{\Delta L}{L_0}\right)_{\omega-\text{form.}} &\approx \frac{1}{3} \cdot \left(\frac{\Delta V}{V_0}\right)_{\omega-\text{form.}} \\ &= \frac{1}{3} \cdot x_\omega \left(\frac{v_\omega(c_V, T)}{v_{\beta,0}} - 1\right) + \frac{1}{3} \cdot x_{\beta\text{-rich}} \left(\frac{v_{\beta\text{-rich}}(c_V, T)}{v_{\beta,0}} - 1\right) \\ &= \left(\frac{\Delta L}{L_0}\right)_\omega + \left(\frac{\Delta L}{L_0}\right)_{\beta\text{-rich}}.\end{aligned} \tag{5.12}$$

In between phase fractions and concentrations, the two relations analogous to Eq.5.4 hold:

$$x_\omega + x_{\beta\text{-rich}} = 1 \tag{5.13a}$$

and

$$c_{V,\omega} \cdot x_\omega + c_{V,\beta\text{-rich}} \cdot x_{\beta\text{-rich}} = c_0. \tag{5.13b}$$

The average volume of atoms in the β-phase is calculated according to Eq.5.10. The average volume of atoms in the hexagonal ω-phase is calculated by applying

$$v_\omega(c_V, T) = \frac{1}{3} \cdot \frac{\sqrt{3}}{2} a_\omega^2(c_V, T) c_\omega(c_V, T), \tag{5.14}$$

where the factor 1/3 is again because of the number of atoms per ω-unit cell.

As before, the relative length changes which are to be expected upon ω-phase formation, have been calculated by applying Eq.5.12 in combination with Eqs.5.11, 5.13, 5.14 and 5.10 in dependence of the ω-phase fraction and for different average V-concentrations $c_{V,\omega}$ in the range of $2 - 10$ at%. The results are presented in Fig.5.9 together with the ones obtained for mere decomposition at equal phase fractions of V-lean region. As can be seen in this figure, the relative length changes to be expected upon ω-formation are in each case strongly negative surpassing by far the length changes caused by mere decomposition in value, where the absolute values increase with decreasing final V-concentration of the particles.

The difference in between mere decomposition and ω-phase formation becomes most prominent, when looking at the curves plotted bold in Fig.5.9, left. Here, the length changes to be expected for both processes have been calculated by assuming both, the V-lean β-phase regions and the ω-phase regions formed to possess a V-content of 10 at%. In this context, however, it must be mentioned that decomposition is unlikely to provide regions with such low V-contents, but these regions will rather transform to the ω-phase.

To sum up, as a further important result, **ω-phase formation leads to strong negative length changes**.

In order to be able to grasp the most important aspects of ω-phase formation, Fig.5.10 shows a schematic illustration of it, which breaks down the different contributions to the overall length changes.

As was explained in Sect.5.1.2 (paragraph "Isothermal ω-phase formation"), ω_{iso} formation requires preceding decomposition to take place, before ω-phase formation is able to start in regions sufficiently depleted in vanadium. Hence, by combining the results derived for mere decomposition and ω-phase formation, ω_{iso}-formation should result in an initial plateau-region caused by decomposition followed by strong negative length changes due to ω-formation.

ω-to-α-transformation according to (iii.):

At elevated ageing temperatures, ω-phase particles are known to transform to the α-phase, at least under the condition of a sufficiently large oxygen content being present, as can be deduced, e.g., from DSC-measurements[107]. To get an idea of the length changes accompanying this kind of transformation process, another formula is derived in the following by applying the same procedure as in the two previous cases.

As mentioned above, α-phase possesses only insignificant solubility for vanadium. As a consequence, the lattice constants are independent of the V-content, but do change only as a function of temperature due to thermal expansion according to

$$a_\alpha(T) = \gamma(c_V = 0, T) \cdot 2.95111\,\text{Å} \tag{5.15a}$$

and

$$c_\alpha(T) = \gamma(c_V = 0, T) \cdot 4.68433\,\text{Å}, \tag{5.15b}$$

where $\gamma(c_V = 0, T)$ is basically the thermal expansion of pure titanium to be used for the α-phase particles. The lattice constants used in this expressions are the ones measured at by Wood at 25 °C for α-Ti[115].

As starting configuration, V-lean ω-phase particles at phase fraction x_ω and V-content $c_{V,\omega}$ surrounded by V-enriched β-phase matrix at phase fraction $x_{\beta\text{-rich}}$ and V-content $c_{V,\beta\text{-rich}}$ are assumed to be present. By counting the length changes again from the state present after quenching (β-phase, smooth compositional profile), such a starting configuration is

involved with strong negative lengths (see Fig.5.9, left part, blue curves). The formula to be derived here describes the length changes occurring upon a growing fraction of α-phase particles originating from the ω-phase particles being present in the beginning. Since the ω-phase commonly contains still several at % vanadium, but more or less no vanadium can be dissolved in the α-phase, the remaining V-atoms in the ω-phase particles are ejected into the β-phase matrix when transforming to α. As a consequence, the surrounding β-phase contracts even more, when its V-content increases. However, since the lattice constants of the α-phase particles surpass even that of the fully decomposed β-phase quite in the contrary to the ones of the ω-phase (see Fig.5.8), the negative length changes due to ω-phase formation are likely to be withdrawn and even the zero line to be exceeded, which becomes also evident by looking at the volumetric calculations in Fig.5.8, lower part.
In this particular case, Eq.5.3 turns into:

$$\begin{aligned}\left(\frac{\Delta L}{L_0}\right)_{\omega\text{-to-}\alpha\text{-transform.}} &\approx \frac{1}{3}\cdot\left(\frac{\Delta V}{V_0}\right)_{\omega\text{-to-}\alpha\text{-transform.}} \\ &= \frac{1}{3}\cdot x_\alpha\left(\frac{v_\alpha(c_V,T)}{v_{\beta,0}}-1\right)+\frac{1}{3}\cdot(x_\omega-x_\alpha)\left(\frac{v_\omega(c_V,T)}{v_{\beta,0}}-1\right) \\ &+\frac{1}{3}\cdot x_{\beta\text{-rich}}\left(\frac{v_{\beta\text{-rich}}(c_V,T)}{v_{\beta,0}}-1\right) \\ &= \left(\frac{\Delta L}{L_0}\right)_\alpha+\left(\frac{\Delta L}{L_0}\right)_\omega+\left(\frac{\Delta L}{L_0}\right)_{\beta\text{-rich}},\end{aligned} \tag{5.16}$$

where in between phase fractions and concentrations, the two relations

$$x_\omega + x_\alpha + x_{\beta\text{-rich}} = 1 \tag{5.17a}$$

and

$$c_{V,\omega}\cdot(x_\omega - x_\alpha) + c_{V,\beta\text{-rich}}\cdot(1-x_\omega) = c_0 \tag{5.17b}$$

hold, analogous to Eq.5.4. The average volume of atoms in the β-phase is calculated by

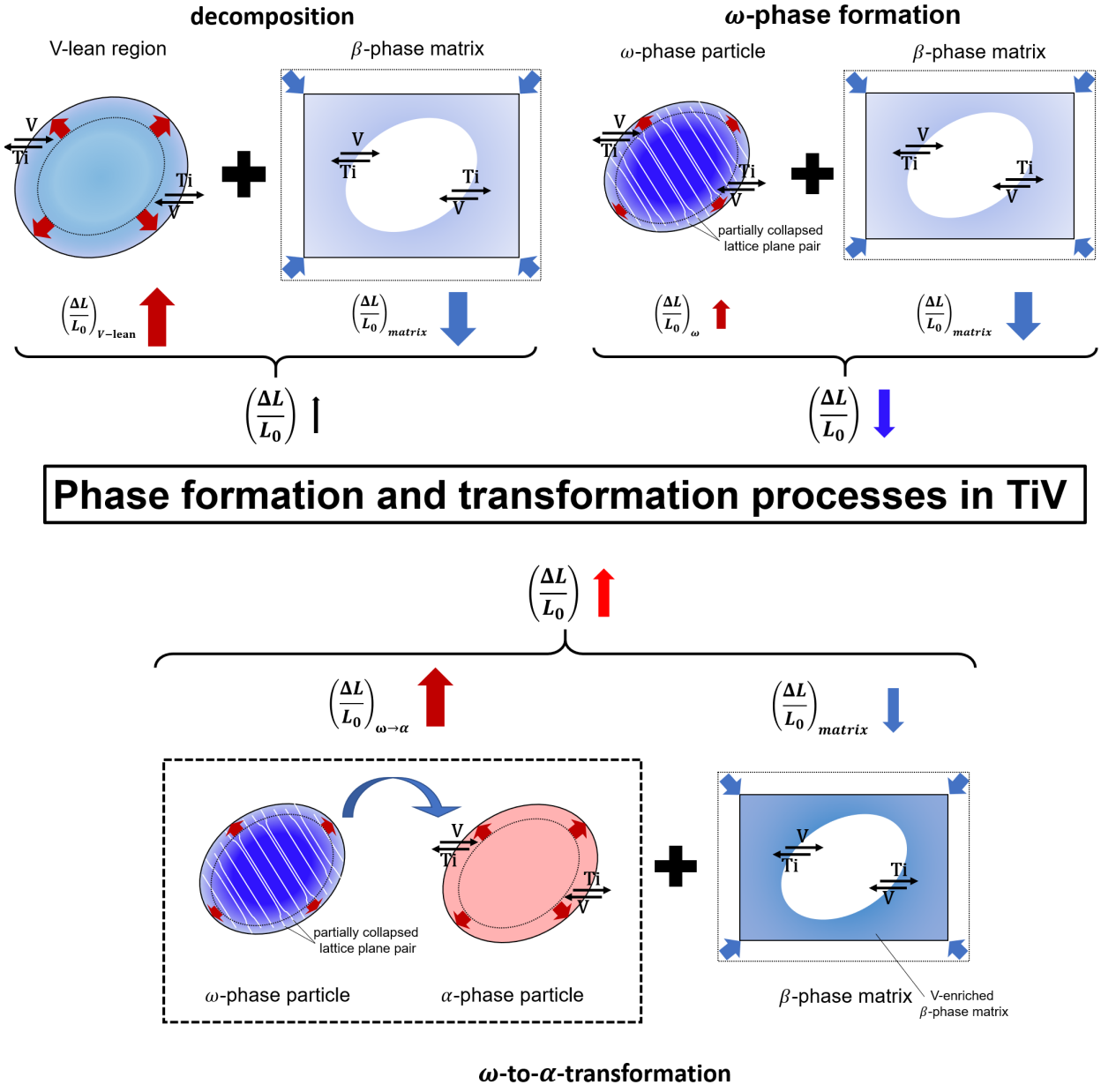

Figure 5.10: Schematic illustration summarising the compositional and corresponding volumetric changes occurring upon mere decomposition of the β-phase (upper part, left), ω-phase formation (upper part, right) and ω-to-α-transformation (lower part) exemplified at a respective phase region (ellipse) and its surrounding matrix. Volumetric expansion is indicated by arrows in dark red, volumetric contraction by arrows in dark blue. The drawings have been created based on the general information about the the phases appearing in the TiV-alloy system as given in Sect.5.1.2, Figs.5.8 and 5.9, and on the statements derived in this section (Sect.5.5.1, framed text fields). The relative length changes $\Delta L/L_0$ corresponding to the overall volumetric changes associated with the different processes happening have been broken down in qualitative manner into the proportions of the phase region and its surrounding matrix according to Eqs.5.8, 5.12 and 5.16. In case of mere decomposition and ω-phase formation (upper part), the relative length changes are counted from a state featuring β-phase with a homogeneous composition everywhere. Accordingly, in case of ω-to-α-transformation, the relative length changes are counted from a state, where V-lean ω-phase particles are present in a V-enriched matrix.

applying Eq.5.10. The average volume of atoms in the hexagonal ω-phase as well as in the hcp α-phase are calculated by applying Eq.5.14, but where in case of the hcp α-phase, the pre-factor amounts to 1/2 and not to 1/3. This is due to the different number of atoms per unit cell.

The relative length changes to be expected upon ω-to-α-transformation have been calculated by applying Eq.5.16 in combination with Eqs.5.10, 5.14, 5.15 and 5.17 in dependence of the α-phase fraction already formed and for different degrees of decomposition of the ω-phase present in the beginning, i.e., different $c_{V,\beta}$. The results are shown in Fig.5.9, right part. Here, the initial state has been assumed to consist of 50 % ω-phase with various V-contents $c_{V,\omega}$, which is a typical fraction of ω-phase formed during ageing in the entire temperature range investigated as will be discussed further in the following.

As can be seen, the relative length changes to be expected upon ω-to-α-transformation are in each case strongly positive, when counting them from the initial state, where 50 % ω-phase are present. This means, upon ω-to-α-transformation, the strong negative length changes appearing due to ω-phase formation are withdrawn and the length changes eventually even surpassing the zero line (see Fig.5.9, right part, upper corner). Although the starting lengths are different according to the calculations having been performed for various initial V-contents $c_{V,\omega}$ of the ω-phase particles, the curves all end up on the same point. This is due to the same phase state being present in each case here, i.e., all ω-phase particles have been transformed to the α-phase.

Thus, all in all, mere and immediate α-phase formation, i.e., without preceding ω-formation, results in slight positive length changes with respect to the state right after quenching, where the material is found to be fully in the β-phase, as suggested by the length changes surpassing the zero line. This is also corroborated by the lattice constants and specific volume of the α-phase (see Fig.5.8, red arrows) exceeding those of the fully decomposed β-phase.

To sum up, as third important result, **ω-to-α-transformation results in strong positive length changes, when counting them from a state, where only ω-phase particles are present.**

As mentioned previously, in order to make the characteristics of the three processes described in this section easier to grasp, the corresponding microscopic changes and associated volumetric changes have been summarised and are schematically drawn in Fig.5.10.

5.5.2 Validation and approximations

In order to quantitatively check the model introduced in the last section, data concerning the phase state, i.e., phase fractions and V-concentration of β-, ω- and α-phase for a certain ageing temperature and time span are required. With these pieces of information, the length changes accompanying the formation of such phase state could be calculated by applying the formulae derived in the last section. By comparing these calculated length changes to the measured ones, the validity of the formulae could be confirmed. However, only minute data exists, since alloys featuring such high V-concentrations as the ones investigated are not of interest for applications in industry making studies concerning these alloys scarce. Furthermore, the determination of the concentrations of ω-phase particles is a rather challenging task due to their nanometre size and requires the most advanced analysis techniques.

There are no complete sets of phase fractions and concentrations available for samples featuring the nominal V-concentration of 21 at%, but there are some sets available for samples featuring V-concentrations of 19 at%, which are presented in Tab.5.1 [119,120]. The results listed there have been obtained from isothermal ageing measurements at 300 °C, which seems to be somewhat like a standard investigation temperature, with only one exception, where a measurement has been performed at 375 °C. At both temperatures, only ω_{iso}-formation is known to be at work, but no transformation of the ω-phase to the α has been observed for the time spans investigated.

In the publications consulted, only the V-contents $c_{V,\omega}$ and $c_{V,\beta}$ of ω- and β-phase are given, which are present after ageing for a time span t_{ageing} at ageing temperature T_{ageing}. Besides these concentrations, the fractions for both phases x_ω and x_β are necessary to perform

Table 5.1: Measurement results from literature concerning the V-concentrations of β-phase $c_{V,\beta}$ and ω-phase $c_{V,\omega}$ as obtained for samples with nominal compositions of Ti 19 at%V as a function of ageing time t_{ageing} and temperature T_{ageing} according to Hendrickson (*) [119] and Choudhuri and co-workers (**) [120]. By applying Eqs.5.13, the phase fractions x_β and x_ω have been calculated from the data provided. By further applying Eq.5.12 in combination with Eqs.5.10, 5.11 and 5.14, the relative length changes $(\Delta L/L_0)_{calc}$ caused by ω-formation have been calculated, which are depicted together with two dilatometric measurements in Fig.5.11. All calculated values are written in bold type.

T_{ageing}[°C]	t_{ageing}	$c_{V,\omega}$ [at %]	$c_{V,\beta}$ [at %]	x_ω [mol %]	x_β [mol %]	$(\Delta L/L_0)_{calc}$ [10^{-3}]
300*	0	–	20.1 ± 0.74	28	72	–
300*	1 min	–	20.4 ± 2.1	–	–	–
300*	10 min	5.4 ± 1.2	21.0 ± 0.3	$\mathbf{13.8 \pm 3.5}$	$\mathbf{86.2 \pm 3.5}$	$\mathbf{-0.60 \pm 0.17}$
300**	10 min	5.4 ± 1.0	23.4 ± 1.0	$\mathbf{24.4 \pm 5.6}$	$\mathbf{75.6 \pm 5.6}$	$\mathbf{-0.68 \pm 0.19}$
300*	1 h	5.5 ± 1.6	21.6 ± 0.4	$\mathbf{16.4 \pm 3.7}$	$\mathbf{83.6 \pm 3.7}$	$\mathbf{-0.58 \pm 0.03}$
300**	1 h	5.8 ± 1.0	22.7 ± 1.0	$\mathbf{21.9 \pm 5.9}$	$\mathbf{78.1 \pm 5.9}$	$\mathbf{-0.64 \pm 0.12}$
300*	64 hrs	5.4 ± 0.9	32.0 ± 0.7	$\mathbf{48.9 \pm 3.0}$	$\mathbf{51.1 \pm 3.0}$	$\mathbf{-1.71 \pm 0.20}$
300**	64 hrs	5.3 ± 1.0	33.0 ± 1.0	$\mathbf{49.1 \pm 2.2}$	$\mathbf{50.8 \pm 2.2}$	$\mathbf{-1.84 \pm 0.05}$
300*	256 hrs	4.5 ± 0.3	34.2 ± 0.4	$\mathbf{52.2 \pm 2.2}$	$\mathbf{47.8 \pm 2.2}$	$\mathbf{-1.96 \pm 0.28}$
300**	256 hrs	4.9 ± 1.0	35.0 ± 1.0	$\mathbf{52.4 \pm 1.6}$	$\mathbf{48.6 \pm 1.6}$	$\mathbf{-2.08 \pm 0.04}$
375*	15 hrs	4.5 ± 0.2	29.5 ± 0.3	$\mathbf{42.1 \pm 1.1}$	$\mathbf{57.9 \pm 1.1}$	$\mathbf{-1.64 \pm 0.02}$

length change calculations according to the model for ω-phase formation. These phase fractions were calculated from the concentrations by applying Eqs.5.13 and have been added to Tab.5.1 (values written in bold type). Based on this, the relative length changes to be expected have been calculated by applying Eq.5.12 in combination with Eqs.5.10, 5.11 and 5.14 and have also been inserted into Tab.5.1 (last column) and plotted into Fig.5.11.

Since there is no information about the oxygen content of the samples investigated in these publications, an oxygen content common for Ti-alloys is assumed to be present comparable to the one of the Ti 20.9V-sample investigated in this work. Hence, length change values calculated based on the literature data are plotted together with the 300 °C- and the 350 °C-curve obtained for the Ti 20.9V from Fig.5.6. Here, the 350 °C-curve is used for comparison with the calculated length change based on literature data for ageing at 375 °C, since no measurement has been taken for 375 °C. The curve for 400 °C is unsuitable for comparison

owing to α-phase formation.

As can be seen from Fig.5.11, the length changes calculated scatter markedly, which is due to the uncertainties of the V-concentrations of ω- and β-phase. However, especially the

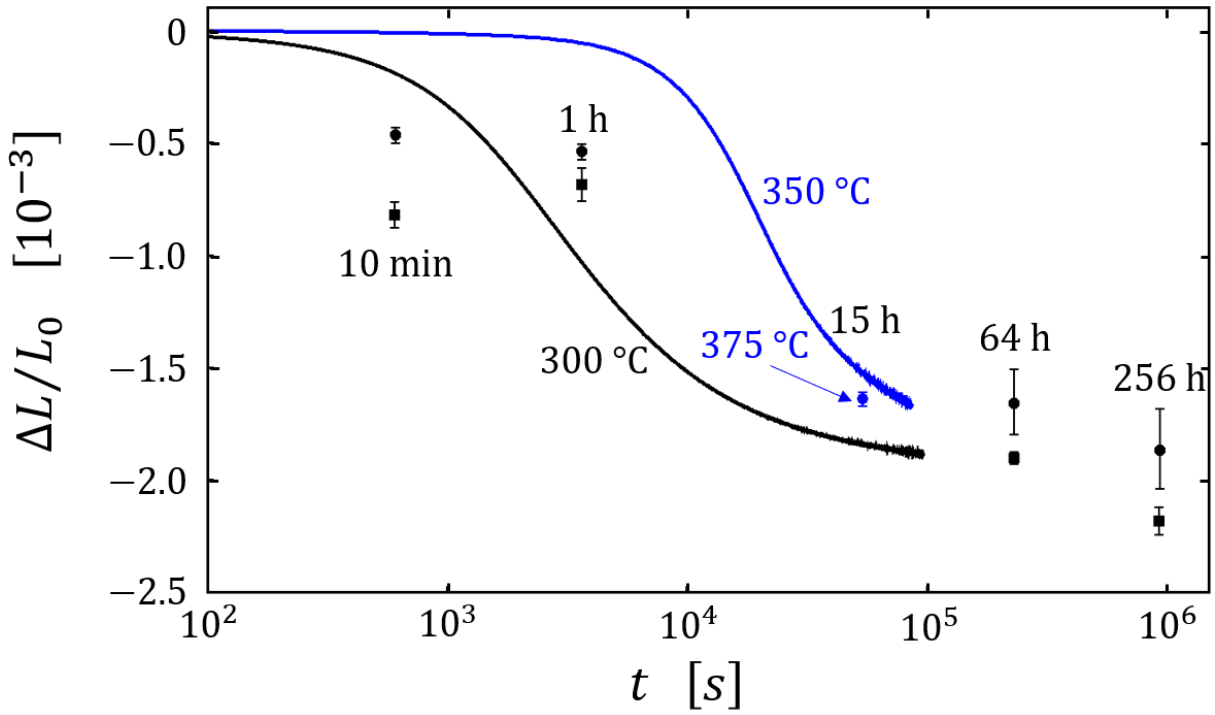

Figure 5.11: Dilatometric measuring curves from Fig.5.6 of the sample with regular oxygen content upon ageing at 300 °C and 350 °C plotted on logarithmic time scale, together with length change values calculated based on data from literature as given in Tab.5.1, last column. The filled circles have been obtained by calculating the length changes based on the data given by Hendrickson[119] and filled squares by calculating the length changes according to the data provided by Choudhuri and co-workers[120].

calculated values for larger ageing times agree satisfactorily well with the measured curve. The calculated values for shorter times differ a bit. At first, they are larger, which is not astonishing due to the presence of ω_{ath}-phase particles in the beginning[120]: As described in Sect.5.1.2 (paragraph "Athermal ω-phase formation"), ω_{ath}-particles are already formed during quenching, when undershooting the athermal transformation limit T_{ath}. As can be deduced from Fig.5.5, this is the case for Ti19V at temperatures somewhere around 300 °C, but not so for Ti21V, even when quenching down to $T_{amb.}$. In fact, the presence of ω_{ath}-particles right after quenching is supported by the data given in Tab.5.1 (first line), where

ω-phase has been found to be there at $t = 0$, i.e., right at the beginning of isothermal ageing. ω_{ath}-particles are known to possess V-contents which are only slightly deviating from that of the surrounding matrix. Thus, according to the calculations shown in Fig.5.9 (left part, ω-phase formation in blue), ω_{ath}-formation itself does not lead to large length changes. During the first period of subsequent ageing, i.e., during the first 10 min, however, the particles may serve as nuclei for ω_{iso}-particles which are known to eject vanadium quite fast into the surrounding matrix after their formation [119,120]. In doing so, notable length changes are to be expected (see again Fig.5.9, left part, ω-phase formation in blue). In case of Ti21V, in the contrary, missing ω_{ath}-formation decelerates ω_{iso}-formation meaning lower phase fractions getting formed at equal times, thereby explaining the deviations of the length changes calculated for Ti19V from the measured ones for Ti21V at 10 min.

In case of Ti19V, V-ejection into the surrounding matrix upon the transformation of ω_{ath}- to ω_{iso}-particles is likely to produce notable length changes during the first period of ageing, i.e. 10 min, but to slow down kinetics when compared to the Ti21V in the further period of ageing, i.e. for periods of 1 h. This can be reasoned by faster V-ejection into the surrounding matrix caused by accelerated ω_{iso}-formation in Ti19V, which hampers the formation of further nuclei. This is due to the fact, that the V-content of the matrix is increased, but ω-phase nucleates in V-lean regions, so its formation is retarded in case of Ti19V compared to Ti21V. This observation is likely to explain the fact, that calculated values for 1 h lay above the present measuring curve, which reflects a lower ω_{iso}-phase fraction in case of Ti19V in this time period.

Furthermore, although obtained upon ageing for 15 h at a slightly higher temperature of 375 °C, the calculated values correspond quite well again with the curve obtained upon ageing at 350 °C, where the discussed initial effects are likely to play no role anymore.

To sum up, also in view of the uncertainties and the fact that the actual alloy possesses a somewhat larger overall V-concentration, **the values predicted by the length change model for ω-phase formation agree satisfactorily well with the measuring curve at least at 300 °C and higher temperatures.**

Approximations:

In the wake of the derivation of the formulae in Sect.5.5.1, a homogeneous compositional profile featuring a constant V-concentration of 21 at% at any point has been assumed to be present in the initial state right after quenching (see Fig.5.4, (b)). In contrast to this assumption, however, compositional variations naturally occurring at solution annealing temperatures get quenched-in. Since such a state is already associated with length changes, when counting it from a homogeneous compositional profile (see Sect.5.5.1, paragraph "mere decomposition" and "ω-phase formation"), it is important to assess the extent of error introduced by this assumption.

In order to estimate the hypothetical length changes accompanying compositional fluctuations with respect to a homogeneous profile, the characteristics of the compositional variations have to be known, i.e., their size and deviation of their composition from the average one. From APT-measurements at the samples investigated in this work performed by Tane and co-workers[88], concentration variations are known to appear normally distributed around the nominal alloy composition in small cubes of 1.5 nm edge length. Here, regions ready for ω-phase formation should be at least twice or four times as large in order to make it take place[86]. In case of solution annealing at 800 °C and 1000 °C (this work: 880 °C), only around 5 % of these cubes are known to possess concentrations equal or less than 15 at%.

Based on these information, in order to get an upper limit for the error introduced by assuming a homogeneous compositional profile, the length changes caused by both, ω-phase formation and mere decomposition each at a phase fraction of $x_\omega = x_{\beta\text{-lean}} = 2.5\,\text{mol}\%$ with an average composition of $c_{V,\omega} = c_{V,\beta\text{-lean}} = 12\,\text{at}\%$ are calculated by applying Eqs.5.8 and 5.12 (see also Fig.5.10). The processes are found to produce relative length changes of $-1.64 \cdot 10^{-5}$ and $3.22 \cdot 10^{-6}$, respectively, which is still more than one and two orders of magnitude smaller compared to the smallest length changes measured, which are found to be in the range of -10^{-4} for the lowest ageing temperatures (see Figs.5.6 and 5.7).

Thus, it can be concluded that, by assuming a smooth compositional profile, no decisive error is introduced to the calculation of amplitudes.

5.5.3 Application of the length change models

In the following, the formulae derived in Sect.5.5.1 for the relative length changes associated with the various phases formation processes in the Ti21V-system are used for an in-depth analysis of the kinetic data. In doing so, special focus is laid on...

- ... identifying the phase regions of the ω_{DI}-, ω_{iso}- and α-phase,
- ... discussing the overall kinetics and the influence of oxygen on it,
- ... calculating the final V-content of the ω-particles present after long term ageing.

Identification of phase regions:

As derived in the last section, mere decomposition, ω-phase formation and ω-to-α-transformation should result in slight positive, strong negative and strong positive length changes, respectively. In view of ω-phase formation, two formation modes are known to appear in case of the samples investigated, i.e., ω_{DI}- and ω_{iso}-formation. In contrast to ω_{DI}-formation, ω_{iso}-formation is known to require preceding decomposition. Assuming decomposition to occur markedly mostly in the first stage of the ageing treatment, i.e. right after quenching, the slight positive length changes accompanying decomposition (see Fig.5.9, left part, black lines) get superimposed with the negative ones caused by the formation of ω-phase particles (see Fig.5.9, left part, blue lines). Since initially there is only a small number of ω-phase particles, the length changes are not as negative as in the second stage of the ageing treatment, where most ω-phase particles have already formed and are just getting lean in vanadium contributing the major portion of the negative length changes. So, all in all, the decomposition process known to be obligatory to happen as part of ω_{iso}-formation should result in an initial plateau region with respect to the length changes. In Figs.5.6 and 5.7, such plateau regions become clearly visible in case of ageing at 350 °C, 400 °C and 450 °C

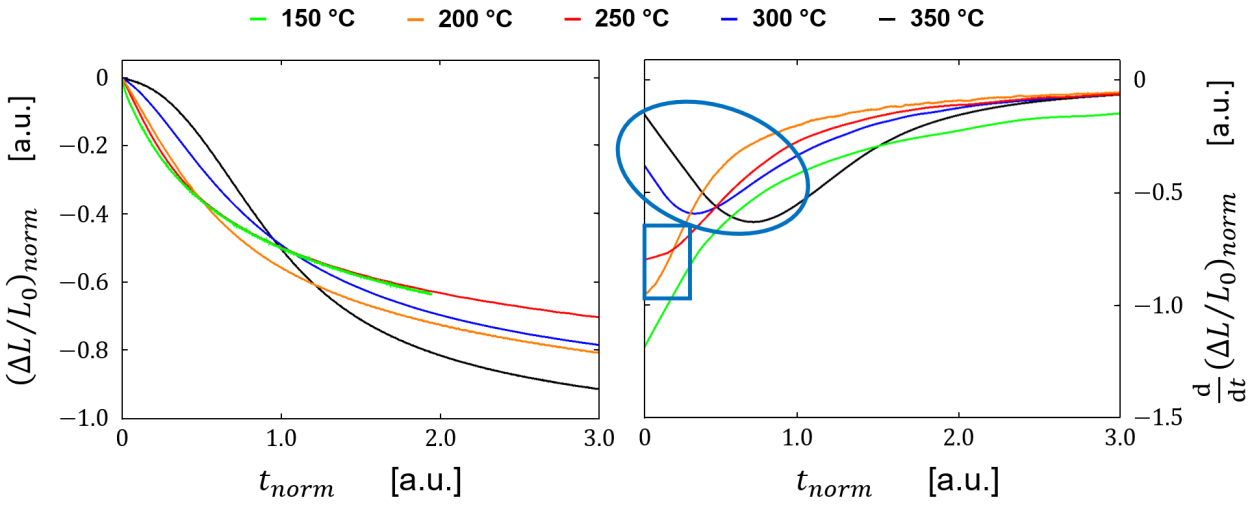

Figure 5.12: Left: Dilatometric measurements for the sample with a regular oxygen content for several ageing temperatures. The curves are the same as the ones depicted in Fig.5.6, but time as well as length changes have been normalised by making use of the time constants and maximum length changes as determined in the following section by kinetic modelling (see Tab.5.3, column 1 and 2). Right: Derivative of the curves presented in the left graph. The blue rectangle and ellipse are used to highlight certain features of the derivative curves.

for both samples right after quenching indicating decomposition.

As described in Sect.5.1.2, V-lean regions loose stability with decreasing temperature, i.e., there is less decomposition necessary for ω-formation to start at these regions[92]. Hence, the initial plateau region should become smaller for decreasing temperature being equivalent to a transition from the ω_{iso}-formation mode to the ω_{DI}-formation mode (see Fig.5.4, left). Since this transition is continuous, the question arises how to determine the limiting temperature in between both formation modes.

Fig.5.12 left shows the dilatometric measurements obtained for ageing temperatures in the range of 150 °C to 350 °C exemplary for the sample with a regular oxygen content as presented in Fig.5.6, but at normalised time and length. In order to obtain normalised time and length values, time constants as well as the extrapolated final maximum length changes from Tab.5.3 (see below) are used. This way of depicting the measurements has been chosen in order to help identifying a potential plateau region appearing right after quenching, which is otherwise only hardly visible due to the strongly different time and length scales of the dilatometric measurements. By looking at the measurements scaled this way, a small initial

plateau region gets even visible in case of ageing at 300 °C (blue). However, in order to decide, where the boundary in between ω_{DI} and ω_{iso}-formation should be drawn, the derivative of the curves has found to be an unmistakable indicator (see Fig.5.12, right).
Here, the tiny positive length changes caused by initial decomposition reduce the strong negative length changes caused by ω-phase formation a bit, manifesting itself in an intensified bending towards the y-axis as observed in case of ageing at 200 °C and 250 °C (blue rectangle in Fig.5.12, right), when being compared to ageing at 150 °C. For ageing at 300 °C and 350 °C, even a minimum can be seen, which is caused by the same mechanism (blue ellipse in Fig.5.12, right). Since neither a minimum or bending is observed for ageing at 150 °C suggesting decomposition not to be involved at all at this temperature, the boundary in between ω_{DI} and ω_{iso}-formation is set to lay in between 150 °C and 200 °C. Similar graphs can be drawn for the dilatometric measurements obtained for the sample with reduced oxygen content (not shown here). Even in this case, the transition from the ω_{DI}- to the ω_{iso}-formation mode is found to take place in between 150 °C and 200 °C.
According to these explanations, the phase regions of ω_{DI}- and ω_{iso}-formation are indicated in Fig.5.13 in green and light blue, respectively, and the preceding decomposition obligatory for ω_{iso}-formation in dark blue. Concerning the ω-to-α-transformation, this process has been shown to be connected with a strong length increase, when starting from the negative length values caused by previous ω-phase formation (see Fig.5.9, right part). Such length increase becomes clearly visible for ageing of 400 °C and in a reduced manner at 450 °C in case of the sample with a regular oxygen content indicating this reaction to take place (see Fig.5.13, light red). For the sample with a reduced oxygen content, the length increase observed in case of ageing at 400 °C is hardly visible and no length increase at all appears in case of ageing at 450 °C indicating α-phase formation to occur strongly reduced. This statement is discussed in detail later. The phase regions, where ω-to-α-transformation occurs are marked in Fig.5.13 in light red.

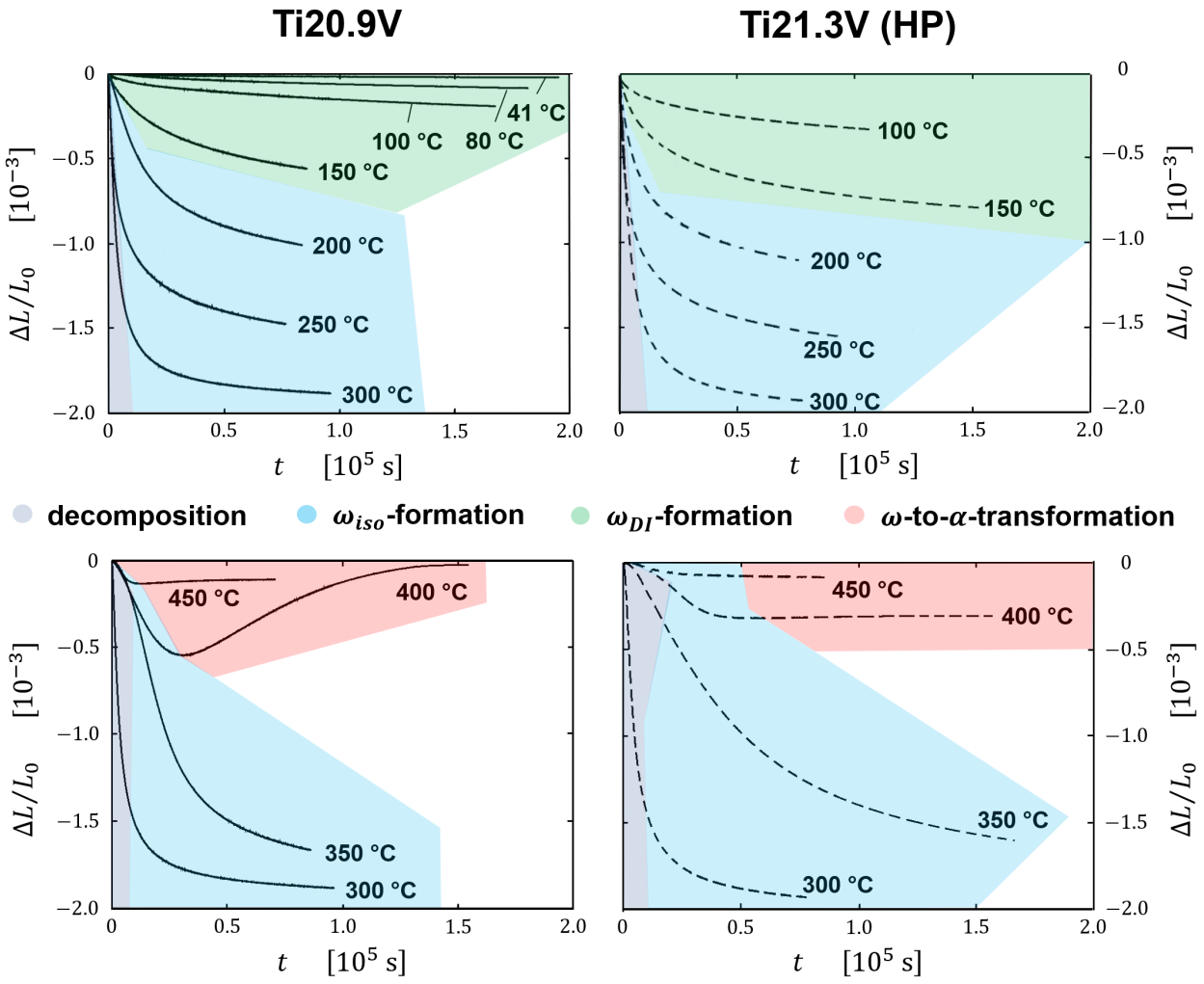

Figure 5.13: Dilatometric measurements as shown in Figs.5.6 and 5.7 for the sample with regular oxygen content (left) and the sample with strongly reduced oxygen content (right). Based on the formulae derived in Sect.5.5.1 and according to the explanations in this section (Sect.5.5.3), the phase regions (time, temperature), where decomposition, ω_{DI}-, ω_{iso}- and α-phase formation take place have been roughly determined and are highlighted by different colours.

As an important result, based on the formulae derived in Sect.5.5.1 for the length changes to be expected upon mere decomposition, ω-formation and ω-to-α-transformation, **the temperature ranges and ageing time periods, where ω_{DI}-, ω_{iso}- and α-formation take place can easily be determined.**

Overall kinetics: evolution of the V-content of ω_{DI}-particles:

Even if the phase regions (time, temperature) for the different formation process are roughly the same (see Fig.5.13), there are some dissimilarities of the measurements obtained at the same ageing temperature but for different samples as well as for different ageing temperatures obtained for the same sample, which need a closer inspection.

As mentioned in Sect.5.4, the measurements conducted in the temperature range between 41 °C and 150 °C are astonishing per se, since all thermally activated processes are reduced to a minimum here, but length changes in the range of -10^{-4} to -10^{-3} do appear (see Fig.5.13, upper part). The formation *mechanism* of ω_{DI}-phase which is known to be at work here, has recently been explained by Tane and co-workers (see [88,92]) and described in Sect.5.1.2. However, there is only little information concerning the compositional *evolution* of the ω_{DI}-phase particles after their formation mainly due to their minute sizes of only a few nanometres making them quite difficult to be investigated. As has been deduced in Sect.5.5.1 (paragraph "ω-phase formation"), negative length changes appearing upon ω-phase formation are due to the ejection of V-atoms from the ω-phase particles into their surroundings exchanging them by Ti-atoms. Since thermally activated processes can be ruled out to take place, there must be a large tendency for ω-phase particles to eject vanadium into the surrounding matrix upon their formation.

As is found in some publications [98,103], the chemistry change upon the formation of ω_{iso}-particles is happening quite fast after their nucleation. This assumption is supported by the data given in Tab.5.1, where the average concentration of the ω-phase is only 10 min after the start of the measurement already close to their obvious final concentration. In this

context, the question appears, in what way the compositional changes of ω_{DI}-phase particles are happening close to $T_{amb.}$, i.e., fast or slowly compared to the time constant of the overall dilatometric measurements. Again based on the shape of the curves, it must be followed that the chemistry changes during low temperature ageing proceed comparably fast independent of the oxygen content, similar to the case of ω_{iso}-formation. This statement becomes clear, when assuming, as a counterexample, that the number of regions where ω-formation takes place decreases over time, but the chemistry change to happen comparably slow. This would result again in kind of an initial plateau region, since the number of ω-phase particles grows to a maximum before notable reduction in the V-content is the process at work. An initial plateau region, however, is not observed for low temperature ageing (see Fig.5.12, ageing at 150 °C).

Thus, as a further important result, **even the reduction of the V-content of ω_{DI}-phase particles must proceed fast compared to the overall time constant of the dilatometric measurement, independent of the oxygen content.**

Overall kinetics: influence of oxygen on ω_{DI}-formation:

As outlined in Sect.5.1.2, the relaxation strength of the lattice planes collapsing as a first step of ω_{DI}-phase formation is known to be strongly reduced at low oxygen contents. This means, arrangements of collapsed lattice planes which are found to happen particularly in V-lean regions, are more likely to be stabilised serving as nuclei for ω_{DI}-particles and make thus ω_{DI}-formation to proceed faster. As a result, ω-formation should be accelerated at low temperature in case of samples with a low oxygen content. By comparing the dilatometric measurements recorded upon ageing at 100 °C and 150 °C for both samples, this is just what is observed in case of of the measurements presented in Fig.5.13. Here, markedly larger length changes occur after ageing for equal time periods in case of the sample with reduced oxygen content. Furthermore, since the ω-phase particles present have been stated to lower their V-concentration quite fast independent of the oxygen content, the larger length changes

upon ageing in the sample with reduced oxygen content yields evidence for a larger number of ω-particles nucleating per time period. This is in perfect agreement with previous observations[107].

Besides the influence of oxygen on ω_{DI}-formation, differences in the oxygen content are also known to affect the ω_{iso}-formation. In fact, it is known that ω_{iso}-formation is retarded at decreased oxygen contents. As described in Sect.5.1.3, CALPHAD-calculations suggest that the miscibility gap of the Ti-V-system completely disappears at zero oxygen content or vice versa, the decomposed version of the Ti-V-system to be only stable, if a certain amount of oxygen is present[87]. Accordingly, one could expect equal degrees of decomposition to appear on larger time scales at reduced oxygen content thereby retarding subsequent ω-formation. This conclusion gets supported especially by the measurements obtained for ageing at 350 °C in Fig.5.13 (lower part), where the initial plateau regions appears enlarged and the whole kinetics seem to be retarded, meaning a reduced number of omega-phase particles is formed at equal time scales.

As can be concluded by just comparing the dilatometric measurements of samples with different oxygen contents, **at lower oxygen contents nucleation is facilitated thereby accelerating ω_{DI}-formation and decomposition is slowed down thereby retarding ω_{iso}-phase formation.**

This is also in good agreement with what is known from literature[99].

Overall kinetics: characteristics of ω-to-α-transformation:

Upon ageing the sample with a regular oxygen content at 400 °C, the length changes increase after decreasing even approaching the zero line meaning the more or less all ω-phase particles formed get transformed to α-phase particles (see Fig.5.9, blue lines left and red lines right). The dilatometric measurement recorded for the same sample in case of ageing at 450 °C (see Fig.5.13, lower part left), however, seems to equilibrate at notable negative length changes suggesting that not all ω-particles present get transformed to α-phase particles. This is an

interesting fact since due to general thermodynamic principles, phase transformations should appear accelerated at increased temperatures, but not be suppressed.

In the following, the formation rate of α-phase particles is assumed to be a function of temperature and composition of the ω-phase particles they are originating from. Since the α-phase is known to possess only a minute V-content, formation should get accelerated by a decreasing V-content of the ω-particles, because then, a reduced amount of V-atoms has to be ejected yet into the surroundings in order to perform ω-to-α-transformation. Furthermore, increasing temperature should promote α-formation.

Based on these considerations, a possible hypothesis to explain the strongly reduced α-formation at low oxygen contents would be the following: At the ageing temperature of 450 °C, α-phase particles get formed quite fast from the small number of ω-phase particles present in the beginning, yet showing relatively high V-contents. Upon α-phase formation, almost all V-atoms have to be ejected into the surrounding matrix, thereby stabilising the matrix in its β-phase. Hence, because of vanadium being induced into the β-phase, the formation of further ω-phase particles or their transformation to α-phase particles is suppressed. In the contrary, upon ageing at 400 °C, ω-phase particles may transform not until the V-content of ω-phase particles is lower than in case of ageing at 450 °C. Consequently, the formation of further ω-phase particles is not suppressed as strongly as in the case, where only a reduced number of ω-phase particles is present, but which have already transformed to α-phase particles at equal time scales. A further reason could be lattice tensions caused by α-phase particles, which hamper ω-phase formation in their surroundings.

To sum up, **the only partial transformation of ω-phase particles found at elevated temperatures could be entirely understood just by kinetic considerations concerning the ω-to-α-transformation.**

V-content of ω-particles after long-term ageing:

The resulting length changes due to ω-formation, i.e., upon ageing in the temperature range

till 350 °C, are a function of the phase fraction of ω-phase particles as well as of their (average) composition. This is due to the fact, that in contrast to the case of precipitation phase e.g., in Al-alloys, which are formed with their more or less final composition, ω-phase particles gradually change their composition after their formation. As a consequence, the phase fraction as well as the average composition have to be known in order to calculate the accompanying length changes, as exemplary performed for the data presented in Tab.5.1. Conversely, it would be desirable to obtain both quantities, i.e. phase fraction and average composition, based on length change measurements, what is, however, not possible, since either one of them has to be known and there is only very few data available.

In this context, at least the state after long term ageing has been characterised with respect to the ω-phase fraction present. This phase fraction is used in the following together with the final maximum length changes to obtain the average ω-phase composition in this final state. In doing so, since length was still (slightly) changing in most cases, when the dilatometric measurements had been stopped, the maximum length changes had to be obtained by extrapolating the measurements. This is done by performing kinetic modelling as discussed in the following section. The extrapolated maximum length changes used hereinafter are listed in Tab.5.3.

Investigations of the phase structure after 10 d-ageing at room temperature reveal a phase fraction of about 67 mol% of the ω-phase being present. This phase fraction has been deduced based on HAADF-STEM images taken by Tane and co-workers [88], where β- and ω-phase regions have been identified by filtering using the respective reflection spots. The final ω-phase fraction upon ageing at 300 °C approximately amounts to only 50 mol% (see Tab.5.1). Since the extrapolated final length changes decrease for decreasing temperature (see Tab.5.3), the ω-particles present after low-temperature ageing must possess higher V-concentrations in the final state (see Fig.5.9, left part, calculated length changes due to ω-formation in blue for various V-contents and phase fractions).

Based on these information, the final ω-phase fraction for all ageing temperatures in between $T_{amb.}$ and 300 °C can be assumed to be somewhere in the range between 50 mol% − 67 mol%.

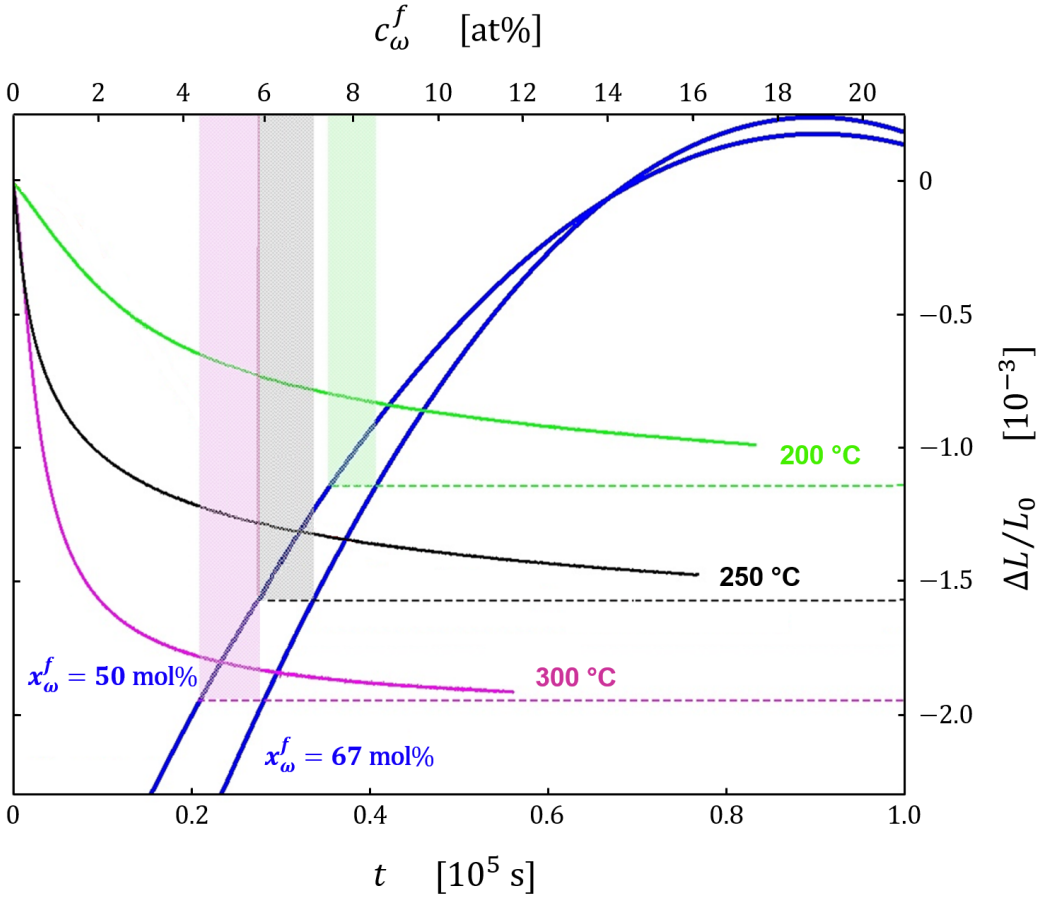

Figure 5.14: Blue curves: Length changes calculated for ω-phase fractions of 50 mol% and 67 mol% which are most likely to appear upon ageing, calculated in dependence of the ω-phase V-concentration according to Eq.5.12 (upper x-axis). A selection of dilatometric measurements has been drawn into the diagram as well (the lower x-axis is the time axis). The intersection points of the predicted maximum length changes appearing upon ageing (dashed lines, taken from Tab.5.3) define the range of concentrations, ω-phase particles ought to possess finally in order to generate the corresponding length changes.

By solving Eq.5.12 for $c_{V,\omega}$ and by inserting this range of phase fractions as well as the extrapolated values for the final length changes, the potential range of the final V-concentration of the ω-phase particles can be calculated.

In Fig.5.14, the calculation is performed in a somewhat graphical manner exemplary for the sample with a regular oxygen content for a couple of selected temperatures. In doing so, again the measurements for ageing at 200 °C in light green, at 250 °C in black and at 300 °C in purple are shown, where the predicted respective maximum length changes reached after long term ageing is drawn into the graph as dashed lines (length plotted against time

Table 5.2: Final V-contents $c_{V,\omega}^{f,50}$ and $c_{V,\omega}^{f,67}$ of the ω-phase particles upon long-term calculated by taking the predicted maximum length changes A obtained by kinetic modelling (see Tab.5.3), assuming the final ω-phase fractions to lay in the range 50 mol% to 67 mol% and by applying Eq.5.12.

	Ti20.9V			Ti21.3V (HP)		
T_{ageing} [°C]	A [10^{-3}]	$c_{V,\omega}^{f,50}$ [mol%]	$c_{V,\omega}^{f,67}$ [mol%]	A [10^{-3}]	$c_{V,\omega}^{f,50}$ [mol%]	$c_{V,\omega}^{f,67}$ [mol%]
41	-0.09	14.0	14.1	–	–	–
80	-0.36	12.1	12.5	–	–	–
100	-0.71	10.1	10.9	-0.80	9.6	10.5
150	-0.88	9.2	10.2	-1.02	8.6	9.6
200	-1.14	8.0	9.2	-1.27	7.5	8.7
250	-1.57	6.3	7.7	-1.61	6.2	7.5
300	-1.88	5.2	6.8	-1.98	4.9	6.4

(lower x-axis); values taken from Tab.5.3). Additionally, the length changes for ω-phase fractions in the range between 50 mol% − 67 mol% have been calculated as a function of the V-concentration of the particles and have been added into Fig.5.14. In doing so, the intersection points of these curves with the predicted maximum length changes determine the compositional range the ω-phase particles are likely to possess.

By applying this procedure, the final V-compositions $c_{V,\omega}^{f,50}$ and $c_{V,\omega}^{f,67}$ of the ω-phase particles present after long term ageing have been calculated for all measurements in the temperature range up till 300 °C for 50 mol% − 67 mol%. The results are summarised in Tab.5.2. In this context, it must be mentioned, that the experimental determination of V-concentration of the ω-phase particles is a challenging task already for the somewhat larger ω-particles obtained by ageing at elevated temperatures. Information about the V-concentrations of ω-phase formed at low ageing temperatures, however, has not been accessible so far due to the minute size of the particles and potentially small compositional variations with respect to the surrounding matrix there.

As a last important result, **the formulae derived above can easily be used to calculate either the ω-phase fraction phase fraction or the average V-content when knowing the other based on the length changes measured.**

5.6 Kinetic modelling of length changes appearing upon ω-phase formation

The last section dealt with finding formulae establishing a connection in between the microscopic changes happening upon phase formation processes and the accompanying macroscopic length changes. In case of ω-formation, the length changes measured at a certain time are found to depend on both the ω-phase fraction as well as the current average concentration of the ω-phase particles. Thus, when knowing about one of these quantities the other one can be calculated. This, however, is problematic insofar, since there is barely any knowledge about both quantities at the same time available in literature.

In this regard, the final states with respect to phase fraction and composition of the ω-particles, achieved upon ageing at different temperatures are interesting, since they represent unique states and allow to draw conclusions about how far ω-phase formation has progressed. Besides important quantities as activation energies and ω-formation rates, which are indispensable ingredients for any computational research on the mechanical properties and predictions concerning other representatives of the Ti-V-alloy class, kinetic modelling of the dilatometry data is used in the following to predict the maximum length changes reached during ageing. This becomes necessary, since during the most measurements the final state cannot be reached due to the obvious large time constants of ω-formation.

Due to the different nature of ω-phase formation compared to an ordinary nucleation and growth reaction, however, it is not evident a priori, whether the traditional approach of applying kinetic models developed to describe nucleation and growth reactions will work in this case and, if so, whether a suitable interpretation of the model parameter can be given. Based on the statements derived in the last section, however, it can be reasoned, that the macroscopic length changes should be similar to these caused by a traditional nucleation and growth process even if the nature of the microscopic processes is different:

- *Concerning nucleation:* The decomposition preceding the ω_{iso}-formation, independent whether driven by or causing embryonic ω-formation, has been shown to cause negligible length changes. This behaviour is quite similar to, e.g., the precipitation sequences found to happen upon ageing in Al-alloys, where metastable clusters are initially formed, which shows no measurable length changes. Despite serving as nuclei for a subsequent precipitation phase, these clusters cause no notable length changes[33,121]. Although the temporal behaviour of the formation rate of an underlying decomposition process may be different to that of the second phase of a precipitation sequence, this fact does not limit the applicability of traditional kinetic models, which are tailored to describe any behaviour of the nucleation rate over time, i.e., if it is decreasing, increasing or remains constant over time[122].

- *Concerning growth:* When speaking of nuclei growth, e.g., in Al-alloys, this corresponds to the generation of additional precipitation phase fraction, where the overall length changes being observed turns out to be a combined effect of matrix and precipitation phase[12,33]. The situation appears similar in case of ω-phase formation, where the biggest difference is, that the length changes are not exclusively caused by the generation of new precipitation phase fraction but rather by (rapid) decomposition of the existing one. From the perspective of macroscopic length changes, however, this makes no difference.

To conclude, it seems to be justified to apply the traditional kinetic models ready to describe nucleation and growth processes also in case of ω-phase formation and evolution. In doing so, the nucleation rate can be equated with the production rate of embryonic ω-particles throughout the ageing process. Furthermore, the growth of the ω-phase particles can be understood as happening not only by the formation of new ω-phase particles, but as a volumetric expansion of the yet existing ω-phase particle caused by the exchange of V-atoms with Ti-atoms from the surroundings (see Fig.5.10). In fact, the combined effect of ω-phase particle expansion and contraction of the surrounding matrix does actually result

in a volumetric contraction as discussed previously (see Sect.5.5.1, "ω-phase formation").

5.6.1 Choosing an adequate kinetic model

From a purely mathematical perspective, it is not essential in case of *isothermal* measurement data, which kinetic model is chosen in order to receive proper formation rates and activation energies[123], as long as good fitting is ensured. Accordingly, the rather general kinetic model

$$\frac{\mathrm{d}\alpha(t)}{\mathrm{d}\alpha_{ext}} = (1-\alpha(t))^{1+c} \tag{5.18a}$$

proposed by Lee and co-workers[124] and worked up by Starink[125] is used. Here, $\alpha(t)$ is the phase fraction of an arbitrary phase, which is found to have yet been transformed at a time t and must not be confused with the α-phase from the previous sections. α_{ext} denotes the extended volume and set to $\alpha_{ext} = (k(T)\cdot t)^{n_g}$ according to the extended volume concept[126]. The integrated form reads (for $c \neq 0$):

$$\alpha(t) = 1 - \left[\frac{(k(T)\cdot t)^{n_g}}{c^{-1}} + 1\right]^{-c^{-1}}. \tag{5.18b}$$

Furthermore, $k(T)$ is the temperature dependent transformation rate, n_g is a parameter akin the Avrami-exponent –one may call it a *generalised* Avrami-exponent– and c is the so-called impingement parameter, whose specific value makes the main difference in between common kinetic models.

This rather general model has been applied in the following to selected representative dilatometric measurements to get a first clue of an adequate but "simpler" kinetic model to be applied. Here, simpler alludes to a reduction of fitting parameters.

In doing so, the kinetic model produced by setting $c = 1$ is found to be appropriate, which is also called the Austin-Rickett kinetic model[127]:

$$\frac{\mathrm{d}\alpha(t)}{\mathrm{d}\alpha_{ext}} = (1-\alpha(t))^{2} \tag{5.19a}$$

$$\alpha = 1 - \left[\frac{1}{(k(T) \cdot t)^{n_{AR}} + 1} \right]. \tag{5.19b}$$

The much more well-known JMAK-kinetic model is obtained by setting $c = 0$ in Eq.5.18a. From a purely mathematical point of view, the Austin-Rickett- and JMAK-kinetic models turn out to be quite similar. In case of the JMAK-kinetic model, the phase formation or transformation rate which is denoted as $\dot{\alpha}$ hereafter, is directly proportional to $(1 - \alpha)$, where this is the fraction, which has not yet transformed. For the Austin-Rickett kinetic model, solely the proportionality between the transformation rate and the fraction not yet transformed gets changed to a quadratic relationship, i.e., $\dot{\alpha}$ is proportional to $(1-\alpha)^2$. Due to this quadratic relationship, instead of the rate decreasing linearly with the fraction not yet transformed, the rate decreases stronger in the beginning and weaker towards the end, what is equivalent to a larger impingement parameter. This approach describes the situation better compared to the JMAK-model as discussed below.

As does the JMAK-kinetic model, the Austin-Rickett kinetic model covers all ways the nucleation may proceed upon (phase) formation or transformation reactions. Zero nucleation rate means, all particles are present from the beginning and there are no nuclei formed during the ageing process, increasing and decreasing nucleation rate means, the number of nuclei formed per unit time enhances or diminishes, respectively. Furthermore, an exponent similar to n, which is called Avrami-exponent in the JMAK-kinetic model, does appear in the Austin-Rickett-kinetic model, which can be interpreted analogously with respect to kind (diffusion-controlled/interface-controlled/mixed mode) and dimensionality of the growth reaction [122].

5.6.2 Application of the Austin-Rickett kinetic model

As shown in the following, the Austin-Rickett-kinetic model provides good fitting of the dilatometric data obtained at all temperatures investigated and for both samples. In addition to the temperature-dependent rate k and the exponent n, the maximum length change to appear as well as an initial y-distance f_0 is passed to the model in order to catch length

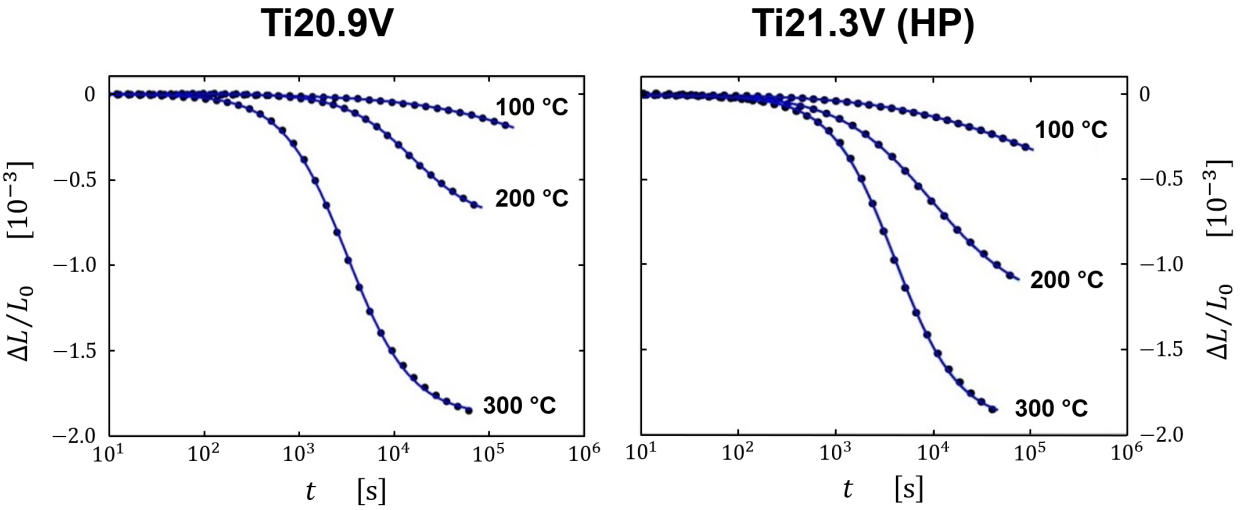

Figure 5.15: Dilatometric measurements (black filled circles) and fit curves (blue) obtained by applying the fit function Eq.5.20 on the data presented in Fig.5.6 for some selected ageing temperatures for the sample with a regular oxygen content (left) and the sample with strongly reduced oxygen content (right). Time has been plotted logarithmically in order to make the quality of the regression apparent.

fluctuations at the beginning thus improving the quality of the fit. The fit function thus reads:

$$f(t) = A \cdot \left\{ 1 - \frac{1}{(k \cdot t)^{n_{AR}} + 1} \right\} + f_0. \tag{5.20}$$

Fig.5.16 shows a selection of dilatometric measurements for both samples (black dots) together with the best fitting curve found (blue lines) obtained by applying the MatLab routine "nlinfit" to the data. In order to assess the quality of the fit, the measurements are depicted on logarithmic scale. Even here, the accordance between kinetic data and fitting curve turns out to be quite satisfactorily. The fit parameters obtained are listed in Tab.5.3.

5.6.3 Discussion of the fitting results

Before pursuing the interpretation of the fitting parameters obtained, the application of the Austin-Rickett kinetic model is discussed against the background of the apparent necessity to use a kinetic model featuring a stronger *impingement* than the JMAK-kinetic model. Such deviations of the impingement parameter may appear, if some of the idealisations assuming

Table 5.3: Results from fitting the Austin-Rickett kinetic model (Eq.5.20) to the dilatometric measurements obtained for both samples in the temperature range up till 350 °C, where ω-phase formation has been proven to be the only process to take place. Some examples of the fitting function applied to the dilatometric data are depicted in Fig.5.15. n_{AR} depending on temperature is shown in Fig.5.16,(a). The maximum relative length change A have been used together with the temperature-dependent rates to create the TTT-diagram in Fig.5.16,(b)

	Ti20.9V			Ti21.3V (HP)		
T_{ageing} [°C]	A [10^{-3}]	k [s^{-1}]	n_{AR}	A [10^{-3}]	k [s^{-1}]	n_{AR}
41	−0.09	$7.21 \cdot 10^{-7}$	0.51	–	–	–
80	−0.36	$9.89 \cdot 10^{-7}$	0.68	–	–	–
100	−0.71	$1.02 \cdot 10^{-6}$	0.87	−0.80	$8.44 \cdot 10^{-6}$	0.57
150	−0.88	$2.26 \cdot 10^{-5}$	0.83	−1.02	$4.19 \cdot 10^{-5}$	0.81
200	−1.14	$6.31 \cdot 10^{-5}$	1.20	−1.27	$1.03 \cdot 10^{-4}$	0.92
250	−1.57	$2.28 \cdot 10^{-4}$	1.28	−1.61	$2.19 \cdot 10^{-4}$	0.91
300	−1.88	$3.12 \cdot 10^{-4}$	1.58	−1.98	$2.45 \cdot 10^{-4}$	1.32
350	−1.71	$4.89 \cdot 10^{-5}$	1.84	−1.84	$2.31 \cdot 10^{-5}$	1.51

in the derivation of the JMAK-kinetic model are not met anymore. A proper compilation of these requirements is given elsewhere[125]. Especially in case of ω-phase formation, two requirements can most likely be considered to get violated:

- *Impingement on objects other than neighbouring domains of the product phase is negligible*: After their formation, ω-phase particles are known to eject V-atoms into their immediate surroundings exchanging them by Ti-atoms. In doing so, the surrounding matrix is stabilised in its β-phase. As a result, the growth of ω-phase particles does not get impeded by other ω-phase particles but by the matrix material.

- *If nucleation occurs, nuclei are randomly distributed and growth rates are independent of the position in the sample*: The activation energy to perform the initial collapse in the V-lean regions, which is the first step in ω-phase formation[107], is known to be broadly distributed. This is caused, on the one hand, by differences existing in the remaining V-content of these regions, where larger V-contents are known to hamper ω-formation and, on the other hand, by large lattice tensions which are known to accompany compositional differences in the Ti-V-system. Also due to differences in the

composition of the immediate surroundings, subsequent growth may either appear more slowly or rapidly. Following these explanations, also this precondition is not fulfilled. Quantitative calculations concerning the impingement parameter as a function of the activation energies are given, e.g., in [125].

To sum up, since the preconditions of unrestricted growth of the ω-particles and a uniform activation energy for their formation are not fulfilled, stronger impingement becomes necessary, making the application of the Austin-Rickett kinetic model appear justified.

Variations of n_{AR} with temperature:

As can be seen in Fig.5.16(a), there is a steady variation of n_{AR} with temperature, i.e. n_{AR} increases from about 0.5 at 41 °C to a bit less than 2 at 350 °C, for Ti20.9V as well as for Ti20.3V(HP). For both samples, the variations of n look similar but appear shifted to higher temperatures in case of the sample with strongly reduced oxygen content. Considering n_{AR} to be equivalent to the Avrami-exponent, one way to interpret it is as being composed of three parameters a, b and c [125,128]:

$$n_{AR} = a + bc. \tag{5.21}$$

Herein, a is a parameter, whose value is determined by the behaviour of the nucleation rate over the measurement time scale. a being 1 corresponds to a constant nucleation rate, a being smaller than 1 to a decreasing one, and a being larger than 1 to an increasing one. In the special case of a being zero, no nuclei are formed during the measurement, but all nuclei are assumed to be present from the beginning. b is the dimensionality of the growth of the newly formed phase ($b \in [0, 3]$) and c is either 0.5 or 1 for *diffusion-controlled* or *interface-controlled* growth, respectively, or something in between for a mixed growth mode. Considering a new phase forming within its parent phase, diffusion-controlled growth refers to a mode, whose rate is determined by how fast the atoms necessary to form the new phase are able to diffuse to the nuclei. A typical example for this kind of growth mode is precipitate

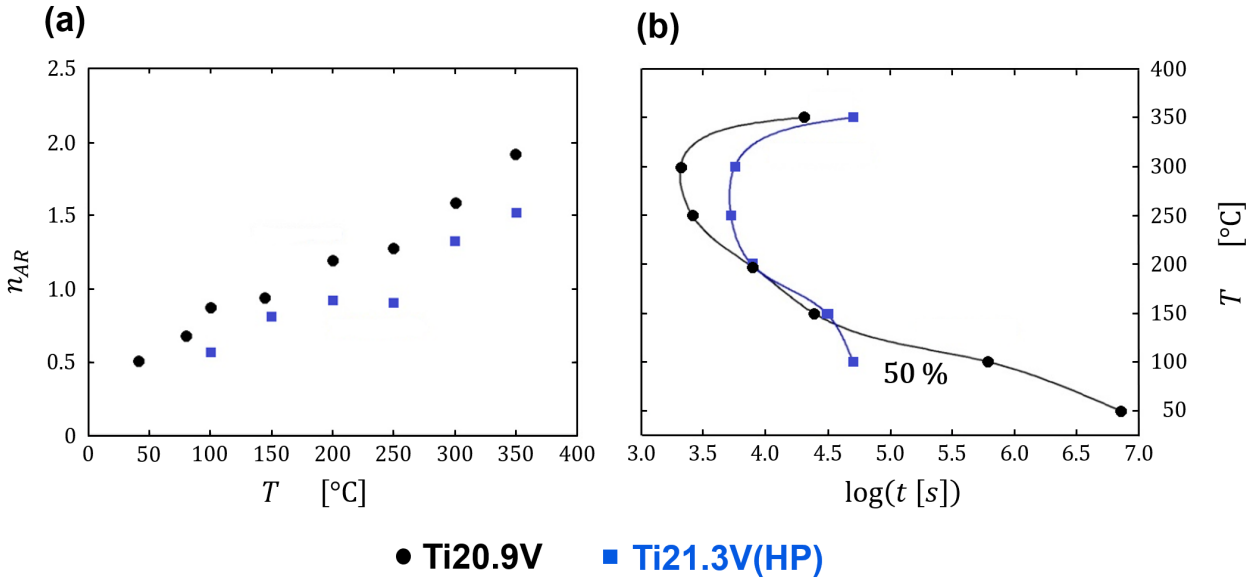

Figure 5.16: (a) Exponent n_{AR} appearing in the Austin-Rickett kinetic model (Fig.5.20) as obtained from fitting the dilatometric measurements for the Ti20.9V-sample (blue) and of the Ti20.3V(HP)-sample (black) in the temperature range, where ω-phase formation is observed. Data as listed in Tab.5.3 (b) Isothermal TTT-diagram for both samples illustrating the time necessary for 50 % of the total length change to happen calculated from the rate constants and amplitudes in Tab.5.3

formation in Al-alloys (see Sect.4.2), where the formation of a B-atoms rich β-phase takes place in an α-phase matrix[129].

Conversely, interface-controlled growth refers to a mode, whose rate is determined by how fast atoms can cross the interface between new and parent phase. Since the exchange of particles across the interface may be connected with a migration of the old interface and the creation of new one, such crossing events appear more or less energetically favourable. A typical example for this kind of growth mode are the initial stages of spinodal decomposition reactions as taking place for ageing at elevated temperatures in the Ti-V-alloy investigated in this work[129].

Bearing in mind the characteristics of ω-phase formation (see Fig.5.10), i.e. the formation within V-lean regions as well as the exchange of V-atoms by Ti-atoms from the surrounding matrix, the value of n_{AR} for the limiting cases of low as well as elevated ageing temperatures, may be explained as follows: For ageing at low temperatures, i.e. close to room temperature, lots of quenched-in V-lean regions are able to transform to the ω-phase with a decreasing

rate over time. Consequently, a has to be smaller than 1. At the same time, it is not clear, whether the nuclei formed grow slightly or at all. Thus, b may be taken as close to zero, causing n_{AR} to be the more or less equal to a. As a consequence, the assumption of n_{AR} being smaller than 1 at low temperatures appears reasonable.

For ageing at elevated temperatures, the second part of n, i.e., the product bc cannot be assumed to be close to zero. This is due to the fact, that a decomposition process has been proven to be at work here as first step in ω_{iso}-formation, which steadily generates new V-lean regions or enlarges the ones yet existing [86]. As known from literature, in the initial state the ω-phase particles appear as small ellipsoids with a size of several nanometres, where after long term ageing, particles about ten times as large are found [119]. The dimension b of growth should thus be larger than 1, but certainly smaller than 3 due to the common shape of phase structures caused by decomposition. Assuming the growth to be interface-controlled in the beginning, when the compositions of ω-phase particles and surrounding matrix are not very different, and to become mixed-mode subsequently, when the compositions notably deviate, c should amount to values close or slightly smaller than 1. Thus, the product bc attains values in the range in between 1 and 2. Together with the nucleation parameter a, which is certainly larger as in the case of low temperature but smaller than 1, because the nucleation rate is most probably decreasing upon ageing, values of $n_{AR} = 1.51$ or $n_{AR} = 1.84$ as found for ageing at 350 °C (see Tab.5.3, last column) are certainly conceivable.

Most interestingly, the n_{AR}-values obtained for both samples indicate a weakly pronounced plateau region starting at a temperature of 150 °C (see Fig.5.16). The plateau region is most probably caused by the transition of the predominate formation mechanism from the diffusionless isothermal to the diffusion-assisted isothermal one, which has been found to happen just at these temperatures (cp. Sect.5.5.3).

To sum up, based on the variation of n_{AR} with temperature (see Fig.5.16), a change in the specifics of the formation mechanism of the ω-phase upon isothermal ageing can be proposed. This change comprises an increase of the nucleation rate with temperature as well as the possibility for ω-particles to grow at elevated temperature as a consequence of an underlying

decomposition process.

Variations of n_{AR} with the oxygen content:

As can be seen from Fig.5.16, the n_{AR} values obtained for the sample with reduced oxygen content appear shifted in general up to higher temperatures but do show the same characteristics. This means that changes in the formation mechanisms occur delayed as the oxygen content is reduced. A reduction in oxygen content is known to promote the formation of ω_{DI}-phase, since the tendency for relaxation of the collapsed lattice planes, representing the first step in ω_{DI}-formation, is reduced. As a consequence, the nucleation rate is either quite high right at the beginning of the measurements or nucleation may even have took place before the actual measurement was started and is diminishing during the measurement time span. This explains the reduced values for n_{AR} and thus a found for the sample with reduced oxygen content in the low temperature regime. In the high temperature regime, oxygen is known to promote the tendency for decomposition. Since the factor bc is growing as a result of enhanced decomposition taking place, therefore also the shift of n_{AR} at elevated temperatures becomes understandable.

Isothermal TTT-diagram:

Based on the amplitudes as well as formation rates obtained from fitting, the isothermal TTT-diagram for this alloy has been created, which is displayed in Fig.5.16(b). There, the points mark a length change of 50 % of the total length change caused by ω-formation, what gives hint about the progress of the formation with respect to the phase fraction formed and degree of decomposition achieved. As can be deduced from this figure, in the temperature range from 200 °C to 350 °C, ω-formation appears to be promoted by the higher amount of oxygen. This observation can be ascribed to the fact, that ω-particles are not as stable, when a larger oxygen phase fraction is present [99], what makes ω-formation proceed faster. Additionally, oxygen is known to increase the tendency for decomposition and may thus be a reason for the slightly larger final maximum length changes observed [87].

For temperatures beneath 200 °C, there is a kind of bulge in case of the alloy with a regular oxygen content for 150 °C, which is significantly stronger, but shifted to lower temperature for the alloy with reduced oxygen content. Similar results have been obtained by DSC-measurements[107]. Here, also a larger peak shifted to lower temperatures has been found, indicating the increased formation of the ω_{DI}-phase in case of the sample with reduced oxygen content. This shift has been ascribed to nucleation being facilitated, which is equivalent to a decreased formation energy.

5.7 Summary and conclusion

β-phase decomposition and ω-phase formation:

- A first quantitative model has been derived, which establishes the connection between the macroscopic length changes appearing upon ageing at temperatures lower than 350 °C and the changes appearing on the microscopic scale, i.e., a growing fraction of ω-phase particles which get depleted in vanadium over time. Based on the dependence of β- and ω-phase lattice constants on the local V-content, the overall negative length changes can be understood as being composed of two contributions: Upon V-ejection into the surrounding matrix, the ω-phase particles themselves are swelling. This swelling, however, is surpassed by the contraction of the surrounding β-phase matrix which is known to happen upon V-uptake in return. A schematic drawing illustrating the different mechanisms contributing to the overall length change is given in Fig.5.10.

- A second quantitative model has been developed in order to explain the effects arising upon mere decomposition of the β-phase. Decomposition processes are known to occur as a first step in ω_{iso}-formation, thus differentiating it from ω_{DI}-formation, and have been found to cause slight positive length changes. Since these positive length changes are overlapped by the large negative length changes of subsequent ω-formation making

them barely visible, a procedure had to be developed in order to identify initial decomposition properly. In doing so, the derivative of the dilatometric curves has been found to be a suitable tool, where initial decomposition becomes visible as bending towards the y-axis or even a local minimum close to it. Initial decomposition has been found to come into effect for temperatures increasing 150 °C. A schematic explanation of how to understand the occurrence of the macroscopic length changes in case of mere decomposition is given in Fig.5.10.

- ω_{DI}-phase formation, which takes place at ageing temperatures close to $T_{amb.}$ has been found to proceed similar to ω_{iso}-formation, except for initial decomposition, which is missing. As could be deduced from the shape of the dilatometric curves, the freshly formed ω_{DI}-phase particles are subjected to a fast chemistry change after their formation, similar to ω_{iso}-phase particles.

- By applying the model for ω-formation, V-concentrations likely to be present after long term ageing could be calculated for all ageing temperatures investigated in the range up till 300 °C.

Kinetic modelling of the length changes accompanying ω-phase formation:

- With respect to kinetic modelling, the application of common nucleation and growth models has found to be suitable. By applying the Austin-Rickett kinetic model, which accounts for the fact of a stronger impingement needed compared to the JMAK-kinetic model, temperature dependent rates for ω-formation could be obtained enabling to draft the isothermal TTT-diagram.

- Based on the isothermal TTT-diagram, ω_{DI}-phase formation has found to proceed by far more intense in case of the sample with reduced oxygen content. ω_{iso}-phase formation, however, has been found to proceed more slowly in accordance with literature data.

ω-to-α-transformation:

- Equivalent to the model developed to estimate the length changes upon ω-phase formation, a quantitative model has been derived for the ω-to-α-transformation, again based on the changes appearing on the microscopic scale.

- In contrast to ω-phase formation, the contraction of the matrix, caused by α-phase particles ejecting all vanadium into the surrounding matrix, has been found to be compensated by the swelling of the α-phase particles. Correspondingly, ω-to-α-transformation has been found to cause strong positive length changes, when counted from a state, where ω-phase particles are already present. Analogously, when counting the length changes from the state right after quenching, where the sample is entirely in β-phase, the length changes are slightly positive.

- Based the length changes predicted, ω-to-α-transformation is found to get strongly suppressed by reducing the oxygen content. For a schematic explanation of the macroscopic length changes arising upon α-to-ω-transformation see Fig5.10.

6 | Kinetics of Vacancy Annealing

Studying the various kinds of lattice defects in crystalline materials like vacancies, dislocations and grain boundaries as well as their mutual interaction is an immensely important task, since they decisively influence all kinds of material properties in divers manner[130,131]. In the specific case of vacancies, examining them is not an easy task due their minute dimensions and, in general, low concentrations in equilibrium.

In this regard, it is not astonishing that their existence was still doubted until the middle of the 20$^{\text{th}}$ century, when Ernest Kirkendall published his pioneering works concerning interdiffusion experiments at the copper/brass-system[132,133]. Besides the necessity of their existence, these experiments gave also a clear hint about the importance of vacancies for diffusion in metallic materials. Since then, many groups have thoroughly investigated them in numerous materials and by applying various techniques with respect to their specifics as, e.g., their temperature-dependent equilibrium concentration[134], their interaction with other lattice defects like dislocation[135], their diffusion behaviour in intermetallics[136] or their volume compared to that of an occupied lattice sites[137], to name just a few.

In doing so, the work presented hereinafter deals with the annealing behaviour of vacancies. In the first part, mathematical models are derived for their annihilation at grain boundaries and dislocations under the important condition of time-linear heating and, as a model system, severely plastically deformed Ni is examined in the second part.

6.1 Basics: high pressure torsion of metallic materials

As indicated above, mathematical descriptions for the annealing behaviour of vacancies are derived for some set-ups and under certain conditions in the following. Since only the most fundamental knowledge is required concerning vacancies, no basics are given here concerning them, but some information are given about high pressure torsion (HPT) as one method to obtain severely plastically deformed (SPD) metallic materials. For a comprehensive study, which covers vacancies in all sorts of solids, reference is made here to the textbook by Cai and Nix[138].

As the designation "high pressure torsion" suggests, samples are subjected to torsional deformation under massive hydrostatic pressure in the course of this technique which is classified as one SPD method. In the course of this technique, a disc-shaped sample is positioned in between two anvils which apply large compressive forces in the range of several GPa in combination with one anvil rotating. Among all SPD techniques, in the course of HPT, the largest hydrostatic pressures can be achieved[139].

In case of pure metals, after severe plastic deformation, lots of them appear ultrafine-grained or nanocrystalline, i.e. with grain sizes smaller than 500 nm or 100 nm[140], respectively, containing an abundance of fundamental crystal defects like vacancies and dislocations, besides grain boundaries. In the special case of HPT-deformed pure metals, owed to the specifics of this treatment, the microstructure produced is strongly anisotropic. In general, grains appear cylindrically- or elliptically-shaped with a certain aspect ratio, which strongly depends on the position with respect to the disc-centre[137]. Evidently, the regions furthest from the centre experience the largest degree of torsional deformation. Correspondingly, the degree of anisotropy may be varied by cutting samples from the disc at different distances to the centre, and, additionally, the orientation of the microstructure with respect to a sample axis can be varied by cutting samples in different directions from the disc, which are designated

as radial, tangential and axial, accordingly.[1] Having initially been limited to small diameters up to 12 mm at the most, today, the production of relatively large discs of HPT-deformed metallic materials with diameters up to 60 mm is possible[139].

The different kinds of defects introduced to the material by HPT come along with a specific amount of excess volume which can be understood as the additional volume introduced to the lattice structure when compared to a sample featuring a perfect defect-free crystal lattice[22]. This *excess volume* correlated to different types of defects is a key quantity for their description and action and is thus important be be known.

Upon temperature increase, (part of) the different kinds of lattice defects may be found to rearrange or to anneal out[141,142]. Here, the method of difference dilatometry (see Sect.2.3) provides a most valuable tool, where measuring HPT-samples against defect-free samples of the same material compensates for all effects except these connected to the crystal defects, since it offers direct access to the volume changes related to the different kinds of crystal defects[22].

6.2 State of research: models for vacancy annihilation and annealing behaviour of HPT-Ni

The publication presented hereinafter deals with the creation of a mathematical model for vacancy annihilation under the important conditions of time linear-heating in a set-up, for which no model has been derived yet. Likewise, some existing models for vacancy annihilation under isothermal conditions are transformed to the conditions of time-linear heating, what is described in the first part of this section. Since especially in HPT-deformed Ni, vacancy annihilation and recrystallisation happen in clearly distinguishable temperature ranges, a corresponding model has been applied to dilatometry data in the publication as a

[1] Note: The possibility to obtain samples with different orientation of the anisotropic grains in relation to the measurement direction made it possible to directly observe the effect of vacancy relaxation, i.e., the volume of lattice vacancies compared to lattice sites occupied by atoms[137].

case study. So, the second and third part of this section deals with the annealing stages of HPT-Ni and its recrystallisation behaviour, respectively.

Models for vacancy annihilation kinetics

The heat equation, or equivalently, the diffusion equation have previously been treated for various problem settings, i.e., in its time independent as well as time dependent version and for different initial and boundary value problems as well as symmetries.

For Cartesian, cylindrical, and spherical symmetry, solutions of the differential equation have been derived previously for the time-independent (isothermal) case and by taking the boundaries as (non-)ideal sinks, which can be found, for instance, in the textbook of Crank[143]. Furthermore, Ozawa derived solutions for cylindrical and spherical symmetries under non-static conditions[144]. Solutions for the time-dependent diffusion equation, but in kind of a reverse case, where cylindrical and spherical crystallites serve as ideal sources (sinks in the publication included hereinafter) have been derived by Seidmann and Balluffi[145].

Annealing stages of HPT-Ni:

Different kinds of lattice defects like vacancies, dislocations and grain boundaries have been well-characterised based on investigations performed at pure metals, which had previously been subjected to a SPD-treatment. The measurements presented hereinafter have been obtained by performing differential dilatometry measurements at HPT-Ni-samples. Especially in the case of Ni, an abundance of lattice vacancies surpassing their equilibrium concentration is known to be stable at $T_{amb.}$ as demonstrated by investigations on quenched Ni-samples[146]. Typical sizes of the ultrafine cylindrical grains obtained by HPT for Ni-samples are found to be in the range of 100 nm to 200 nm[147].

Upon linear heating of the samples starting at such state at $T_{amb.}$, a couple of techniques allow the identification of at least two stages. By applying difference dilatometry, they become most clearly visible as two subsequent regions featuring length decreases of strongly different rates[148]. The length changes in the first region, which ranges from approximately 20 °C to

200 °C, are primarily caused by the annealing of vacancies at other lattice, what has been proven by the combination of DSC-measurements[149] with electron microscopy measurements[150]. These measurements have later been confirmed also by combined investigations of the S-parameter in the course of positron annihilation spectroscopy and dilatometry[141]. Consistent with these findings, Ni-vacancies are known to become mobile at approximately 90 °C[146]. Concerning the activation energy for vacancy diffusion in Ni, it has been found to amount to about 1 eV[151]. The second stage appearing in the temperature range larger than 200 °C, which is indicated by more steep length decrease, must be ascribed to grain growth. This has been proven by scanning electron microscopy[141]. It is thought that the two processes do the more or less not overlap.

Recrystallisation of HPT-Ni:

In order to model at least the first two stages observed as parts of the annihilation behaviour of HPT-Ni, a model for non-isothermal kinetic of recrystallisation of an ultrafine-grained microstructure is necessary in addition to those derived for the annealing kinetics of vacancies. Henderson dealt with expanding the model of isothermal recrystallisation on the basis of the JMAK-approach also to the non-isothermal case and performed also investigations concerning the range of applicability of his approach[152]. Later on, Louis and Garcia-Cordovilla refined his approach by comparing in particular the activation energies obtained by applying non-isothermal JMAK-kinetics to that determined by applying Kissinger's method in its non-isothermal version[153,154]. According to Oberdorfer and co-workers, the activation energy for recrystallisation in ultrafine-grained materials amounts to 1.2 ± 0.04 eV, where the frequency factor amounts to $K_0 = 2.4 \pm 0.7 \cdot 10^{10}\,\mathrm{s}^{-1}$[154].

6.3 Motivation

Since vacancies represent one of the most important lattice defects in crystalline material, models have been developed for their annealing behaviour and formation mechanisms by several groups for various cases.
In this context, the work presented hereinafter aimed at ...

- ... the derivation of a mathematical model for the kinetics vacancy annealing at dislocations. The dislocations are assumed to represent ideal sinks for the vacancies. Diffusion of the vacancies to the dislocations is considered to occur from the surrounding space which is modelled to be of cylindrical shape and under the important conditions of time-linear heating.

It has been proven before that annealing of vacancies at dislocations is not the major process which leads to a reduction of the vacancy concentration in HPT-Ni[137], but annealing at grain boundaries. Thus,

- ... by combining the models for the annihilation of vacancies at grain boundaries and for recrystallisation, both under the conditions of time-linear heating, model fitting of the difference dilatometry annealing curves obtained for HPT-Ni should be performed.

6.4 Experimental

A disc of ultrafine-grained nickel featuring a diamter of 30 mm and a thickness of 10 mm has been prepared by HPT using 5 revolutions at a pressure of 2.2 GPa from high-purity-Ni as base material (99.99 %). Dilatometry samples with a size of $7 \times 3 \times 3\,\mathrm{mm}^3$ have been cut from this disc, i.e., from regions with a radius larger than 5 mm distance from the centre, guaranteeing a uniform anisotropic grain structure featuring ellipsoidal grains with an aspect ration of 1.5 to 1.7 at an average length of 298 ± 4 nm of the long axis as determined by

electron microscopy. The long axes of the grains are oriented parallel to the length measurement direction.

The length change measurements have been conducted in the vertical difference dilatometer described in Sect.2.3. The HPT-sample investigated has been measured against a high-purity Ni-reference sample, which is well-annealed, coarse-grained, and defect-free, by applying a heating rate of $6\,\mathrm{K min^{-1}}$ starting at $T_{amb.}$ and up to 500 °C. The measurements were performed under Ar-gas flow.

All calculations and curve fitting with the model functions for vacancy annealing and recrystallisation have been performed with MatLab by applying the curve fitting tool "nlinfit".

6.5 Publication: Kinetics of vacancy annealing upon time-linear heating applied to dilatometry

Preamble: The article "*Kinetics of vacancy annealing upon time-linear heating applied to dilatometry*" was published in Journal of Materials Science **53** (2758-2765), November 2017[155].

With respect to modelling the annealing curves of HPT-Ni-samples by the combined kinetic models for vacancy annealing and recrystallisation, the idea has been developed and some preliminary work has been done by Christian Neubauer and Roland Würschum. The solution to the differential equation for vacancy annealing at dislocations and, in particular, the treatment of its time-dependence has been derived by the author. Modelling of the annealing curve of HPT-Ni with the fitting functions for vacancy annealing and recrystallisation as well as the design of all graphs has been done by the author. The publication has been written by Roland Würschum in collaboration with the author.

J Mater Sci (2018) 53:2758–2765

Metals

Kinetics of vacancy annealing upon time-linear heating applied to dilatometry

R. Enzinger[1], Chr. Neubauer[1], J. Kotzurek[1], W. Sprengel[1], and R. Würschum[1,*]

[1] *Institute of Materials Physics, Graz University of Technology, Petersgasse 16, 8010 Graz, Austria*

Received: 23 September 2017
Accepted: 30 October 2017
Published online: 9 November 2017

ABSTRACT

A kinetic model for the diffusion-controlled annealing of excess vacancies under the experimentally relevant, non-isothermal condition of time-linear heating is presented and applied to dilatometry. The evolution of the vacancy concentration with time is quantitatively analyzed, considering as ideal sinks either dislocations or grain boundaries of spherical- or cylindrical-shaped crystallites. The validity of the model is tested using dilatometry data that were obtained for ultrafine-grained Ni prepared by high-pressure torsion. The entire two-stage annealing curve of the dilatometric length change can be analyzed by combining the present kinetic model of vacancy annealing at grain boundaries with established non-isothermal kinetics of recrystallization.

Introduction

Dilatometry as a powerful thermo-analytical tool has recently been more and more applied to study absolute concentrations and kinetics of defects in metals [1]. The basic idea is that upon annealing-induced removal of defects which are associated with excess volume, such as vacancies, dislocations, or grain boundaries, a macroscopic shrinkage of the solid occurs in reference to a defect-free sample. In this way, the absolute concentration of lattice vacancies as well as the excess volume of grain boundaries could be determined for ultrafine-grained metals prepared by techniques of severe plastic deformation, i.e., high-pressure torsion (HPT) and equal-angular channel pressing [2–5]. Similar to differential scanning calorimetry (DSC), these measurements are often performed in the mode of time-linear heating rather than isothermally due to reasons of signal stability and strength. Moreover, various annealing processes can be scanned in one single run which is of relevance since the processes are inherently irreversible so that each sample can be used only once.

Different defect types may be distinguished by their distinct temperature regimes of annealing during linear heating which is reflected in more or less well-separated annealing stages of the irreversible length change curve $\Delta l/l(T)$. For the length change associated with the annealing of grain boundaries in the wake of crystallite growth, a kinetic model for non-isothermal heating already exists on the basis of the Johnson–Mehl–Avrami–Kolmogorov theory (JMAK) ([6, 7], see below, "Recrystallisation" section) which was applied to dilatometry data on ultrafine-grained nickel by Oberdorfer et al. [8].

Address correspondence to E-mail: wuerschum@tugraz.at

DOI 10.1007/s10853-017-1780-4

The present work aims to extend non-isothermal modeling to point defects as well, by developing a kinetic model for the diffusion-controlled annealing of excess vacancies at various types of sinks under the non-isothermal condition of time-linear heating. For ultrafine-grained crystallites, major sinks of vacancies are grain boundaries. Here, spherical- and cylindrical-shaped grains will be considered ("Annealing of vacancies at grain boundaries" section), geometries which have earlier been treated for thermal analysis of evaporation of toluene from an epoxy resin by Ozawa [9]. A major type of sink in single or coarser-grained crystals is dislocations. Following Seidmann and Balluffi [10] dealing with dislocations as sources of thermally generated vacancies, in the present work the annealing of vacancies for straight dislocations is modeled ("Annealing of vacancies at dislocations" section). In the discussion ("Discussion" section), the model is tested using ultrafine-grained HPT-deformed Ni as a case study and the model is compared to other models of vacancy kinetics in metals [11].

Modeling of annealing kinetics

In the following, kinetic models are presented for the non-isothermal annealing of lattice vacancies at dislocations ("Annealing of vacancies at dislocations" section) and at grain boundaries of spherical- or cylindrical-shaped crystallites in metals ("Annealing of vacancies at grain boundaries" section). For the sake of comparison, the kinetics of non-isothermal recrystallization is summarized in "Recrystallisation" section.

Annealing of vacancies at dislocations

The annealing kinetics of vacancies at dislocations is modeled assuming a regular array of parallel straight dislocation lines. The straight dislocation is considered as cylinder (radius a), the surface of which acts as ideal sink. Lattice vacancies within a concentrical hollow cylinder around the dislocation anneal out by diffusion toward the inner wall at the center with the cutoff radius a of the dislocation. The outer radius b of the hollow cylinder is related to the dislocation density N_d per unit area by

$$b = \frac{1}{\sqrt{\pi N_d}} \,. \tag{1}$$

Due to cylindrical symmetry, the diffusion equation for the vacancy concentration $C(r, t)$ reads:

$$\frac{\partial C}{\partial t} = D\left(\frac{\partial^2 C}{\partial r^2} + \frac{1}{r}\frac{\partial C}{\partial r}\right), \quad a < r < b \tag{2}$$

where D denotes the vacancy diffusion coefficient, r the radius, and t the time.

For taking into account non-isothermal conditions and, therefore, a time-dependent diffusion coefficient $D(t)$, we use the ansatz

$$C(r,t) = U(r)\cdot X(t)\,. \tag{3}$$

With the separation constant $-\beta^2$, this leads to the time-dependent part

$$\frac{\mathrm{d}X}{X} = -\beta^2 D(t)\mathrm{d}t\,. \tag{4}$$

For the usual case of time-independent D, the solution of Eq. (4) reads (see, e.g., the textbook of Carslaw and Jaeger [12]):

$$X(t) = \exp\left(-D\,\beta^2\,t\right). \tag{5}$$

For the spacial part $U(r)$, the Bessel differential equation of zero order is obtained from Eq. (3):

$$\frac{\mathrm{d}^2 U}{\mathrm{d}r^2} + \frac{1}{r}\frac{\mathrm{d}U}{\mathrm{d}r} + \beta^2 U = 0. \tag{6}$$

The ideal sink behavior of the dislocation gives the boundary condition at the inner cutoff radius:

$$U(r = a) = 0\,. \tag{7}$$

The outer boundary condition

$$\left.\frac{\partial U}{\partial r}\right|_{r=b} = 0 \tag{8}$$

reflects the vanishing vacancy flux through the outer border ($r = b$) of the diffusion cylinder. The solution of Eq. (6) satisfying the inner boundary condition (Eq. 7) is given by [12]

$$U(\beta r) = Y_0(\beta a)J_0(\beta r) - J_0(\beta a)Y_0(\beta r) \tag{9}$$

where J_0 and Y_0 denote Bessel functions of the first and second kind, respectively. The outer boundary condition (Eq. 8) yields a conditional equation for β

$$-J_1(\beta b)Y_0(\beta a) + J_0(\beta a)Y_1(\beta b) = 0 \tag{10}$$

that is solved by a set of discrete values $\beta = \beta_n$.

With $U(\beta_n r)$ representing the solution of Eq. (6) for $\beta = \beta_n$, a partial solution of the diffusion Eq. (2) reads $\exp(-D\,\beta_n^2\,t)\cdot U(\beta_n r)$. Due to the linearity of the diffusion equation, the general solution is given by the superposition of the partial solutions for different β_n:

$$C(r,t) = \sum_{n=1}^{\infty} A_n \exp\left(-D\,\beta_n^2\,t\right) U(\beta_n r). \tag{11}$$

The coefficients

$$A_n = \frac{\int_a^b r\,C(r,0)\,U(\beta_n r)\,\mathrm{d}r}{\int_a^b r\,U^2(\beta_n r)\,\mathrm{d}r} = \frac{N(\beta_n)}{T(\beta_n)} \tag{12}$$

are to be determined by the initial condition $C(r, 0)$.

Assuming a homogeneous initial distribution $C(r,0) = C_0$ of lattice vacancies, the numerator $N(\beta_n)$ and denominator $T(\beta_n)$ of A_n (Eq. 12) can be calculated. Taking into account properties of the Bessel functions ([13], see Appendix) and making use of Eq. (10), one obtains for the numerator

$$N(\beta_n) = -\frac{2C_0}{\pi\beta_n^2} \tag{13}$$

and after some algebra for the denominator

$$T(\beta_n) = \frac{b^2}{2}\left(Y_0(\beta_n a)J_0(\beta_n b) - J_0(\beta_n a)Y_0(\beta_n b)\right)^2 - \frac{a^2}{2}\left(Y_0(\beta_n a)J_1(\beta_n a) + J_0(\beta_n a)Y_1(\beta_n a)\right)^2. \tag{14}$$

For the sake of illustration, concentration profiles $C(r, t)$ according to the above solution (Eqs. 11, 12, 13, 14) are shown in Fig. 1 for different values of $D \times t$.

Integrating the concentration of vacancies $C(r, t)$ over the total volume of the hollow cylinder yields the fraction $\alpha(t)$ of vacancies not yet annealed out at the time t:

$$\alpha(t) = \int_a^b C(r,t)\,2\pi r\,\mathrm{d}r\,. \tag{15}$$

After insertion of Eq. (11) and integration using the properties of Bessel functions (see "Appendix") and Eq. (10), one obtains

$$\alpha(t) = \sum_{n=1}^{\infty} \frac{8}{\pi\,\beta_n^3\,T(\beta_n)} \times \exp\left(-D\,\beta_n^2\,t\right) \tag{16}$$

as a function of time t with $T(\beta_n)$ according to Eq. (14) and β_n denoting the roots of Eq. (10).

Next, we consider the non-isothermal case for which the diffusion coefficient D in general becomes

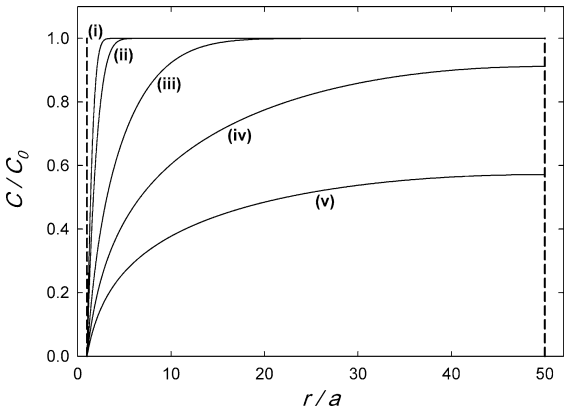

Figure 1 Cylinder-symmetrical vacancy concentration profile $C(r, t)$ for diffusion-controlled vacancy annealing at dislocations in dependence of r / a with the inner cutoff radius $a = 0.3$ nm and the outer radius of the diffusion cylinder of $b = 15$ nm (corresponding to $r/a = 50$). The curves represent different values $D \times t$ showing the evolution of the profile with time t. (i): $D \times t = (b/100)^2$, (ii): $(b/50)^2$, (iii): $(b/10)^2$, (iv): $(b/2)^2$, (v): b^2.

time-dependent. For the important experimental situation of time-linear heating with a rate h, the thermally activated diffusion coefficient reads:

$$D(t) = D_0 \exp\left(-\frac{Q}{k_B\,(T_0 + h\cdot t)}\right), \tag{17}$$

where k_B denotes the Boltzmann constant, T_0 the starting temperature, Q the activation energy of diffusion, and D_0 the pre-exponential factor. With $D(\tau)$ according to Eq. (17), the following solution is obtained for the time-dependent part (Eq. 4) of the diffusion equation:

$$X(t) = \exp\left(-\beta^2 \int_0^t D(\tau)\,\mathrm{d}\tau\right) = \exp\left(-\beta^2\,\frac{D_0\,Q}{k_B\,h}\left[\frac{\mathrm{e}^{-x'}}{x'} + \mathrm{Ei}(-x')\right]_{x_0}^{x}\right) \tag{18}$$

where $\mathrm{Ei}(x)$ denotes the exponential integral function [13] and

$$x = x'(\tau = t) = \frac{Q}{k_B\,(T_0 + h\cdot t)}, \tag{19}$$

$$x_0 = x'(\tau = 0) = \frac{Q}{k_B\,T_0}. \tag{20}$$

Irrespective of the time dependence of D, the diffusion Eq. (2) is linear with solutions given by any superposition of partial solutions for different β_n.

Moreover, the time dependence of D does not affect the boundary conditions (see Eqs. 7 and 8). Therefore, the root equation for β_n (Eq. 10) and the coefficients A_n (Eq. 12) are also valid with Eq. (18), so that for the solution for time-linear heating Eq. (16) modifies to

$$\alpha(t) = \sum_{n=1}^{\infty} \frac{8}{\pi \beta_n^3 T(\beta_n)} \times \exp\left(-\beta_n^2 \frac{D_0 Q}{k_B h} \left[\frac{e^{-x'}}{x'} + \mathrm{Ei}(-x') \right]_{x_0}^{x} \right) \tag{21}$$

with $T(\beta_n)$ and β_n according to Eqs. (14) and (10), respectively, as above. We note that the solution differs from that of Seidman and Balluffi [10] due to the different boundary and initial conditions.

Annealing of vacancies at grain boundaries

In ultrafine-grained materials, even more prevalent than vacancy annealing at dislocations, may be the annealing out of lattice vacancies at grain boundaries. Here, we consider the two important cases of spherical- and cylindrical-shaped crystallites for which the solutions of the diffusion equation for constant diffusion coefficient are given in the textbook of Crank [14]. In analogy to Eq. (16), the fraction $\alpha(t)$ of vacancies not yet annealed out at the time t reads for grain boundaries of spherical-shaped crystallites

$$\alpha(t) = \frac{6}{\pi^2} \sum_{n=1}^{\infty} \frac{1}{n^2} \exp\left(\frac{-D n^2 \pi^2 t}{a^2} \right) \tag{22}$$

and for cylindrical-shaped crystallites

$$\alpha(t) = \sum_{n=1}^{\infty} \frac{4}{a^2 \beta_n^2} \exp\left(-D \beta_n^2 t \right) \tag{23}$$

where a denotes the radius. As in the previous subsection, here the grain boundaries are considered as ideal sinks and a homogeneous initial vacancy distribution in the crystallites is assumed. For the cylindrical symmetry (Eq. 23), β_n is determined by the roots of the Bessel function

$$J_0(a\beta_n) = 0. \tag{24}$$

This textbook solution can be extended to the case of time-linear heating with time-dependent diffusion coefficient according to Eq. (17). Again, in analogy to Eq. (21), one obtains for the case of spherical crystallites

$$\alpha(t) = \frac{6}{\pi^2} \sum_{n=1}^{\infty} \frac{1}{n^2} \exp\left(-\frac{n^2 \pi^2}{a^2} \cdot \frac{D_0 Q}{k_B h} \left[\frac{e^{-x'}}{x'} + \mathrm{Ei}(-x') \right]_{x_0}^{x} \right) \tag{25}$$

and for cylindrical crystallites

$$\alpha(t) = \sum_{n=1}^{\infty} \frac{4}{a^2 \beta_n^2} \exp\left(-\beta_n^2 \frac{D_0 Q}{k_B h} \left[\frac{e^{-x'}}{x'} + \mathrm{Ei}(-x') \right]_{x_0}^{x} \right) \tag{26}$$

with β_n according to Eq. (24). We note that these solutions for spherical and cylindrical geometry in general correspond to those derived by Ozawa [9]; however, the present treatment refrains from an approximation [15] of the exponential integral function as applied earlier [9].

The computed vacancy annealing curves for the three types of sink geometries are shown in Fig. 2 using for the vacancy diffusion data exemplarily those of nickel according to literature, i.e., a pre-exponential factor $D_0 = 9.2 \times 10^{-5}$ m^2/s and an activation energy $Q = 1.04$ eV [16]. Here, $a = 100$ nm is assumed for the radii of the cylindrical or spherical crystallites. For dislocations with an inner cutoff radius $a = 0.3$ nm [10], the outer radius of $b = 21$ nm is adjusted so that the vacancy annealing at

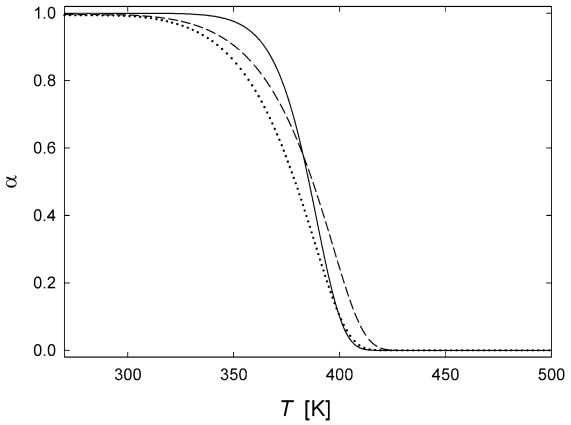

Figure 2 Fraction α of vacancies not yet annealed according to time-linear heating kinetics of diffusion-controlled vacancy annealing at the three types of ideal sinks modeled in this paper: straight dislocations (solid line, Eq. 16), grain boundaries of spherical- (dotted line, Eq. 25) and cylindrical-shaped crystallites (dash-dotted line, Eq. 26). Parameters are as follows: heating rate $h = 6$ K/min, pre-exponential factor $D_0 = 9.2 \times 10^{-5}$ m^2/s, activation energy $Q = 1.04$ eV, radius of cylindrical or spherical crystallites $a = 100$ nm (Eqs. 25 and 26), inner cutoff $a = 0.3$ nm, and outer radius $b = 21$ nm for dislocation model Eq. (16).

dislocations occurs in the same temperature regime as the annealing at grain boundaries. The value $b = 21$ nm corresponds to a dislocation density of $\rho = 7.2 \times 10^{14}$ m^{-2} (Eq. 1).

It becomes apparent that in the case of identical crystallite size the vacancy annealing at grain boundaries of spherical-shaped crystallites occurs earlier during time-linear heating compared to cylindrical-shaped crystallites (compare dotted and dashed line in Fig. 2, respectively). This reflects the reduced mean diffusion length for reaching the sinks in the case of spheres compared to cylinders. Comparing the cylindrical-symmetrical cases of vacancy annealing at grain boundaries or dislocations (dashed or full line in Fig. 2, respectively), it is worthwhile to point out that the maximum diffusion radius (here $b = 21$ nm), i.e., the distance between the dislocations, has to be much smaller than the crystallite radius ($a = 100$ nm) for obtaining vacancy annealing in the same regime of heating. This is due to the fact that the narrow inner cylindrical area which acts as sink in the case of the dislocation is much smaller than the outer cylindrical area acting as sink in the case of the grain boundary.

In the example above, a starting temperature $T_0 = 270$ K was used for the lower bound x_0 (Eq. 20). Replacing this lower bound by $x_0 \to \infty$, i.e., setting $T_0 = 0$ K, does not affect the result in this case. One should, however, consider that significant deviations may occur when the annealing stage is only slightly above T_0.[1]

Recrystallisation

In order to compare the kinetic model of vacancy annealing with experimental annealing data on extremely deformed, ultrafine-grained metals, we present for the sake of completeness the non-isothermal solution of recyrstallization kinetics. The Johnson–Mehl–Avrami–Kolmogorov (JMAK) model of recrystallization was first adapted to non-isothermal kinetics by Henderson [6]. Under conditions of time-linear heating with the rate h, Louis and Garcia-Cordovilla [7] obtained for the fraction α not yet transformed up to the time t:

$$\alpha(t) = \exp\left[-\left(\frac{K_0 Q}{k_B h}\int_x^\infty \frac{\exp(-x')}{x'^2}\,\mathrm{d}x'\right)^n\right] \tag{27}$$

with x according to Eq. (19).[2] n denotes the Avrami exponent and Q or K_0 the activation energy or the pre-exponential factor of the recrystallization rate function $K(T) = K_0 \exp(-Q/(k_B T))$, respectively (see also [8]).

To be conformal with the above solutions for vacancy annealing, we replace the upper integration limit by $x_0 = Q/(k_B T_0)$ (see Eq. 20). Similar as in the previous subsections, the integral can be expressed by the exponential integral function, yielding:

$$\alpha(t) = \exp\left[-\left(\frac{K_0 Q}{k_B h}\left[\frac{\mathrm{e}^{-x'}}{x'} + \mathrm{Ei}(-x')\right]_{x_0}^{x}\right)^n\right]. \tag{28}$$

As above, using the lower bound $x_0 \to \infty$ is justified as long as the recrystallization stage lies well above T_0.

Discussion

The present model is particularly well suited for quantitatively analyzing dilatometry data of materials prepared by severe plastic deformation, such as high-pressure torsion [17]. These materials may contain a high-abundant concentration of lattice vacancies as well as a high number of grain boundaries associated with the submicron crystallite size. HPT-Ni is an attractive model system, since lattice vacancies in Ni are stable at ambient temperature and become mobile at temperatures around 360 K [16] below the recrystallization stage which starts at about 470 K [2]. Therefore, with respect to the measurement, the length change associated with the annealing out of vacancies is well separated from the length change which occurs due to the removal of grain boundaries (GBs) upon crystallite growth (Fig. 3). Also, the model assumptions apply well for this case since the crystallite size remains constant during diffusion-mediated vacancy annealing and the character of the GB sinks may be considered as

[1] In the present example, using as lower bound $T_0 = 0$ K instead of 270 K gives rise to deviations in the 5%-range when the middle of the annealing stage is shifted down to 296 K by reducing Q from 1.04 to 0.78 eV.

[2] Note: Unlike to the cited paper of Louis and Garcia-Cordovilla [7], here α is defined as the material fraction *not yet* transformed in order to be consistent with the definition of α in "Annealing of vacancies at dislocations" and "Annealing of vacancies at grain boundaries" sections as the fraction of vacancies not yet annealed out.

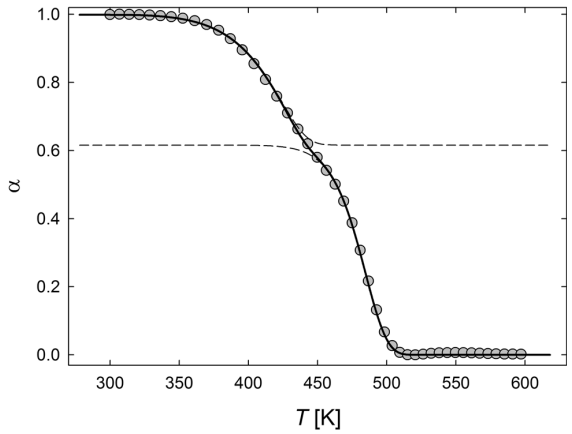

Figure 3 Two-stage dilatometer annealing curve of HPT-Ni in dependence of temperature T upon heating at a rate h of 6 K/min. Comparison of experimental data (dot) with the combined models of vacancy annealing at GBs of cylindrical crystallites (first stage) and subsequent recrystallization (second stage). α: fraction not yet annealed out or transformed (Eqs. 26,28); relative length change $\Delta l/l = 2.7 \times 10^{-4}$ for both stages. Model parameter for vacancy stage (Eq. 26): $Q = 1.04$ eV [16], $D_0 = 2.3 \times 10^{-5}$ m^2/s. Model parameter for recrystallization stage (Eq. 28): $n = 1.1$, $Q = 1.2$ eV, $K_0 = 1.8 \times 10^{10}$ 1/s. Common model parameters: relative fraction of vacancy (recrystallization) stage: 0.38 (0.62); mean crystallite radius $a = 100$ nm with a Gaussian distribution of width $\sigma = 25$ nm taking crystallite radii in steps of 5 nm over a width of 2σ (i.e., between 75 and 125 nm). Solid line: sum of the two model curves; dashed lines: model curves for each of the two stages.

stable during this annealing process due to the high sink density.

Figure 3 shows the experimental two-stage variation of the dilatometer length change of HPT-Ni [18] along with an analysis according to the present model. The model represents a superposition of vacancy annealing at GBs with subsequent recrystallization. Since HPT-Ni has an anisotropic structure with elongated grain shape [2, 5], the solution for the cylinder-symmetrical case (Eq. 26) was used for modeling. The crystallite size was deduced from scanning electron microscopy approximating the size distribution by a Gaussian function with the values as quoted in the caption of Fig. 3. Apart from the activation energy of vacancy migration, the model parameters were obtained from fitting the experimental two-stage curve; these parameters are summarized in the figure caption as well. It is apparent from Fig. 3 that the experimental data can be described perfectly by the present model. The relative fractions of both stages are given by the clearly discernible transition between the two substages. The activation energy of 1.2 eV obtained for the recrystallization stage is the same as that deduced earlier from Kissinger analysis of the shift of the stage with the heating rate [8].

Although the presented modeling of vacancy annealing kinetics was stimulated by our experimental studies on HPT metals, the application of this model is by far not restricted to this type of materials. In fact, the model is suitable for other issues of vacancy annealing as well, for instance, for the analysis of annealing of excess vacancies which are obtained by quenching of vacancies formed at high temperatures in thermal equilibrium.

Finally, the presented model on vacancy annealing at different types of sinks will be compared with that reported by Fischer et al. [11]. The model developed by Fischer et al. [11] is based on non-equilibrium Onsager's thermodynamic [19] and treats the generation and annihilation of vacancies at sources and sinks from the view point of continuum mechanics in a general manner taking into account mechanical driving forces and the role of bulk viscosity. Similar to the present model, ideal behavior of the vacancy sinks (dislocations, grain boundaries) is supposed. Whereas for the general case, the resulting differential equations are to be solved numerically, for isothermal conditions only analytical solutions are derived for vacancy annealing at dislocations and GBs of spherical crystallites from which the time evolution of the vacancy concentration can be determined implicitly.

Compared to ref. [11], the present direct ansatz based on atomistic diffusion yields closed-form expressions right for the practical important non-isothermal case of time-linear heating. In addition to dislocations and GBs of spherical crystallites, also GBs of cylindrical crystallites were considered as sinks. As exemplarily shown for the test case of HPT-Ni, these solutions can be combined with JMAK kinetics of recyrstallization and allow a comparison with experimental data in a straightforward manner. Despite its simplicity, our model is considered to capture the most relevant features of vacancy annealing. It should be pointed out that this model of vacancy annealing is not restricted to dilatometry, but may be applied to other techniques of thermal analysis as well, such as differential scanning calorimetry.

Acknowledgements

Open access funding provided by Austrian Science Fund (FWF). This work was financially supported by the Austrian Science Fund (FWF): P25628-N20.

Appendix

The following formulae for Bessel functions [13] are used in "Annealing of vacancies at dislocations" section

$$J_1(z)Y_0(z) - J_0(z)Y_1(z) = \frac{2}{\pi z} \tag{29}$$

$$\int_a^b r J_0(\beta r)\,\mathrm{d}r = \frac{1}{\beta}\left(b J_1(\beta b) - a J_1(\beta a)\right) \tag{30}$$

$$\int_a^b r J_0^2(\beta r)\,\mathrm{d}r = \frac{b^2}{2}\left(\left[J_1(\beta b)\right]^2 + \left[J_0(\beta b)\right]^2\right) - \frac{a^2}{2}\left(\left[J_1(\beta a)\right]^2 + \left[J_0(\beta a)\right]^2\right) \tag{31}$$

$$\int_a^b r J_0(\beta r)Y_0(\beta r)\,\mathrm{d}r = \frac{b^2}{2}\left(J_0(\beta b)Y_0(\beta b) + J_1(\beta b)Y_1(\beta b)\right) - \frac{a^2}{2}\left(J_0(\beta a)Y_0(\beta a) + J_1(\beta a)Y_1(\beta a)\right) \tag{32}$$

with

$$\int z J_n(az)\,Y_n(az)\,\mathrm{d}z = \frac{z^2}{4}\left(2J_n(az)Y_n(az) - J_{n-1}(az)Y_{n+1}(az)\right) \tag{33}$$

$$J_{-n}(z) = (-1)^n J_n(z) \tag{34}$$

For Y_0 or Y_n equations analogous to Eq. (30) or (34) hold, respectively.

References

[1] Sprengel W, Oberdorfer B, Steyskal EM, Würschum R (2012) Dilatometry—a powerful tool for the study of defects in ultrafine-grained metals. J Mater Sci 47:7921–7925. doi:10.1007/s10853-012-6460-9

[2] Steyskal EM, Oberdorfer B, Sprengel W, Zehetbauer M, Pippan R, Würschum R (2012) Direct experimental determination of grain boundary excess volume in metals. Phys Rev Lett 108:055504

[3] Oberdorfer B, Setman D, Steyskal EM, Hohenwarter A, Sprengel W, Zehetbauer M, Pippan R, Würschum R (2014) Grain boundary excess volume and defect annealing of copper after high-pressure torsion. Acta Mater 68:189–195

[4] Kotzurek J, Steyskal EM, Oberdorfer B, Hohenwarter A, Pippan R, Sprengel W, Würschum R (2016) Direct measurement of vacancy relaxation by dilatometry. Appl Phys Lett 109:021906

[5] Kotzurek J, Sprengel W, Krystian M, Simic S, Pölt P, Hohenwarter A, Pippan R, Würschum R (2017) Structural anisotropy in equal-channel angular extruded nickel revealed by dilatometric study of excess volume. Int J Mater Res (formerly Z Metallkd) 108:81–88

[6] Henderson DW (1979) Thermal analysis of non-isothermal crystallization kinetics in glass forming liquids. J Non Cryst Solids 30:301–315

[7] Louis E, Garcia-Cordovilla C (1984) On the determination of kinetic parameters through the peak temperature method for differential scanning calorimetry. J Therm Anal 29:1139–1150

[8] Oberdorfer B, Steyskal EM, Sprengel W, Pippan R, Zehetbauer M, Puff W, Würschum R (2011) Recrystallization kinetics of ultrafine-grained Ni studied by dilatometry. J Alloys Comp 509:S309–S311

[9] Ozawa T (1973) Non-isothermal kinetics of diffusion and its application to thermal analysis. J Therm Anal 5:563–576

[10] Seidman DN, Balluffi RW (1965) Sources of thermally generated vacancies in single-crystal and polycrystalline gold. Phys Rev 139:A1824–A1840

[11] Fischer F, Svoboda J, Appel F, Kozeschnik E (2011) Modeling of excess vacancy annihilation at different types of sinks. Acta Mater 59:3463–3472

[12] Carslaw HS, Jaeger JC (1986) Conduction of heat in solids. Clarendon Press, Oxford

[13] Olver FWJ et al (2010) NIST handbook of mathematical functions. Cambridge University Press, Cambridge

[14] Crank J (1975) The mathematics of diffusion. Clarendon Press, Oxford

[15] Doyle CD (1965) Series approximations to the equation of thermogravimetric data. Nature 207:290–291

[16] Ehrhart P, Ullmaier H (1991) New Series III/25, Atomic Defects in Metals, Landolt-Börnstein, Vol. 25, Springer

[17] Pippan R, Scheriau S, Taylor A, Hafok M, Hohenwarter A, Bachmaier A (2010) Saturation of fragmentation during severe plastic deformation. Ann Rev Mater Res 40:319–343
[18] Steyskal EM (2010) Untersuchung freier Volumen in submikrokristallinem Nickel mit der Methode der Dilatometrie, Master Thesis, Graz University of Technology
[19] Svoboda J, Fischer F, Fratzl P, Kroupa A (2002) Diffusion in multi-component systems with no or dense sources and sinks for vacancies. Acta Mater 50:1369–1381

6.6 Summary and conclusion

As a missing piece, a model for vacancy annihilation inside cylindrically-shaped grains has been developed for the important conditions of time-linear heating. Dislocations in the centre of those grains representing ideal sinks have been assumed to act as annihilation sites. In order to illustrate their annealing behaviour, the spacial distribution of the not-yet-annealed fraction of vacancies in the surroundings of the dislocations has been drawn for several points in time for the model derived and in comparison with models for vacancy annihilation at grains boundaries of different symmetries.

As a second part, a combined model of vacancy annealing at grain boundaries and of recrystallisation has been successfully applied to the dilatometric annealing curves of HPT Ni-samples. The fitting parameters, i.e., activation energies for vacancy diffusion and recrystallisation, agree excellently with the ones known from literature.

7 | Concluding Remarks

High-precision isothermal dilatometry has been most successfully applied within this doctoral thesis to study the formation processes of secondary phases in an Al-Mg-Si-alloy and in a Ti-V-alloy. Since the presence of secondary phases decisively influences the mechanical properties of these alloy systems, the thorough examination of their formation processes is indispensably important and constitutes the basis for further improving their mechanical performance.

In both systems, these formation processes are found to take place via several metastable intermediate phases, what makes their analysis a more challenging task. Here, especially the combination of high-precision dilatometry measurements with mathematical models for the length changes to be expected upon the formation of the metastable phases turns out to be an unbeatable tool to investigate them in detail. Conclusions can be drawn, inter alia, about such important features as the phase regions of their appearance, the order of their formation, their lattice structure and composition as well as their formation rates and formation energies.

In this context, it has to be mentioned, that based on the descriptions within this thesis, the procedure of how to exploit dilatometric measurements with respect to all these quantities concerning metastable phases should be easily transferable to other alloy systems.

Bibliography

[1] F. Ostermann. *Anwendungstechnologie Aluminium.* Springer-Verlag, 3rd edition (2015).

[2] W. A. Monteiro. *Light metal alloys applications.* BoD–Books on Demand, 1st edition (2014).

[3] F. Schmid, P. Dumitraschkewitz, T. Kremmer, P. J. Uggowitzer, R. Tosone and S. Pogatscher. Enhanced aging kinetics in Al-Mg-Si alloys by up-quenching. *Commun. Mater.*, **2** (2021) 1.

[4] W. Miller, L. Zhuang, J. Bottema, A. Wittebrood, P. De Smet, A. Haszler and A. Vieregge. Recent development in aluminium alloys for the automotive industry. *Mater. Sci. Eng. A*, **280** (2000) 37.

[5] A. Heinz, A. Haszler, C. Keidel, S. Moldenhauer, R. Benedictus and W. Miller. Recent development in aluminium alloys for aerospace applications. *Mater. Sci. Eng. A*, **280** (2000) 102.

[6] C. Zener. Contributions to the theory of beta-phase alloys. *Phys. Rev.*, **71** (1947) 846.

[7] M. Niinomi and M. Nakai. Titanium-based biomaterials for preventing stress shielding between implant devices and bone. *Int. J. Biomater.*, **2011** (2011).

[8] F. Prima, J. Debuigne, M. Boliveau and D. Ansel. Control of omega phase volume fraction precipitated in a beta titanium alloy: Development of an experimental method. *J. Mater. Sci. Lett.*, **19** (2000) 2219.

[9] S. Sikka, Y. Vohra and R. Chidambaram. Omega phase in materials. *Prog. Mater. Sci.*, **27** (1982) 245.

[10] H. Fizeau. Ueber die Ausdehnung starrer Körper. Zweite Abhandlung. *Ann. Phys.*, **211** (1868) 372.

[11] G. Weidmann. Messungen mit dem Abbe'schen Dilatometer. *Ann. Phys.*, **274** (1889) 453.

[12] E. Hengge, R. Enzinger, M. Luckabauer, W. Sprengel and R. Würschum. Quantitative volumetric identification of precipitates in dilute alloys using high-precision isothermal dilatometry. *Philos. Mag. Lett.*, **98** (2018) 301.

[13] H. M. Semnani and H. Degischer. Precipitation in AlCu4.3 and AlCu4Mg alloys studied by dilatometry and calorimetry. *Kov. Mater.-Metall. Mater.*, **49** (2011) 369.

[14] M. E. Brown. *Introduction to thermal analysis: Techniques and applications*, volume 1. Springer Science & Business Media (2001).

[15] O. Engler and J. Hirsch. Texture control by thermomechanical processing of AA6xxx Al–Mg–Si sheet alloys for automotive applications - a review. *Mater. Sci. Eng. A*, **336** (2002) 249.

[16] W. H. Fietz, K. Grube and H. Leibrock. Dilatometry under high pressure. *Int. J. High Press. Res.*, **19** (2000) 373.

[17] G. Parker. *Encyclopedia of materials: Science and technology*. Elsevier, 1st edition (2001).

[18] E. Pereloma and D. V. Edmonds. *Phase transformations in steels: Fundamentals and diffusion-controlled transformations.* Elsevier, 1st edition (2012).

[19] D. C. Wallace. Thermal expansion and other anharmonic properties of crystals. *Phys. Rev.*, **139** (1965) A877.

[20] C.-É. Guillaume. *Nobel Lecture: L'invar et l'élinvar.* Lüdin (1974).

[21] N. Bekkedahl. Volume dilatometry. *J. Res. NIST*, **43** (1949) 145.

[22] W. Sprengel, B. Oberdorfer, E.-M. Steyskal and R. Würschum. Dilatometry: A powerful tool for the study of defects in ultrafine-grained metals. *J. Mater. Sci.*, **47** (2012) 7921.

[23] R. Küchler, T. Bauer, M. Brando and F. Steglich. A compact and miniaturized high resolution capacitance dilatometer for measuring thermal expansion and magnetostriction. *Rev. Sci. Instrum.*, **83** (2012) 095102.

[24] G. Schmiedeshoff, A. Lounsbury, D. Luna, S. Tracy, A. Schramm, S. Tozer, V. Correa, S. Hannahs, T. Murphy, E. Palm et al. Versatile and compact capacitive dilatometer. *Rev. Sci. Instrum.*, **77** (2006) 123907.

[25] R. Küchler, A. Wörl, P. Gegenwart, M. Berben, B. Bryant and S. Wiedmann. The world's smallest capacitive dilatometer, for high-resolution thermal expansion and magnetostriction in high magnetic fields. *Rev. Sci. Instrum.*, **88** (2017) 083903.

[26] M. Luckabauer, W. Sprengel and R. Würschum. A high-stability non-contact dilatometer for low-amplitude temperature-modulated measurements. *Rev. Sci. Instrum.*, **87** (2016) 075116.

[27] A. Karamanov, B. Dzhantov, M. Paganelli and D. Sighinolfi. Glass transition temperature and activation energy of sintering by optical dilatometry. *Thermochim. Acta*, **553** (2013) 1.

[28] M. Jankula, P. ŠÍN, R. PODOBA and J. ONDRUŠKA. Typical problems in push-rod dilatometry analysis. *JSBCM*, **65** (2013).

[29] M. Okaji. Absolute thermal expansion measurements of single-crystal silicon in the range 300–1300 K with an interferometric dilatometer. *Int. J. Thermophys.*, **9** (1988) 1101.

[30] N. Koga. Ozawa's kinetic method for analyzing thermoanalytical curves. *J. Therm. Anal. Calorim.*, **113** (2013) 1527.

[31] S. Vyazovkin. Kissinger method in kinetics of materials: things to beware and be aware of. *Molecules*, **25** (2020) 2813.

[32] B. Milkereit, H. Froeck, C. Schick and O. Kessler. Continuous cooling precipitation diagram of cast aluminium alloy Al-7Si-0.3Mg. *Trans. Nonferrous Met. Soc. China*, **24** (2014) 2025.

[33] R. Enzinger, E. Hengge, W. Sprengel and R. Würschum. High-precision isothermal dilatometry as tool for quantitative analysis of precipitation kinetics: case study of dilute al alloy. *J. Mater. Sci.*, **54** (2019) 5083.

[34] S. Vyazovkin and C. A. Wight. Isothermal and non-isothermal kinetics of thermally stimulated reactions of solids. *Int. Rev. Phys. Chem.*, **17** (1998) 407.

[35] P. Gill, S. Sauerbrunn and M. Reading. Modulated differential scanning calorimetry. *J. Therm. Anal. Calorim.*, **40** (1993) 931.

[36] Y. Kraftmakher. Modulation calorimetry and related techniques. *Phys. Rep.*, **356** (2002) 1.

[37] N. Burley. Nicrosil/Nisil Type N Thermocouples. *J. Meas. Control.*, (1989) 130.

[38] B. Edlén. The refractive index of air. *Metrologia*, **2** (1966) 71.

[39] K. Birch and M. Downs. Correction to the updated Edlén equation for the refractive index of air. *Metrologia*, **31** (1994) 315.

[40] T. D. Kelly, G. R. Matos, D. A. Buckingham, C. A. DiFrancesco, K. E. Porter, C. Berry et al. Historical statistics for mineral and material commodities in the united states. *US Geological Survey Data Series*, **140** (2010) 01.

[41] M. Merklein and M. Geiger. New materials and production technologies for innovative lightweight constructions. *J. Mater. Process. Technol.*, **125** (2002) 532.

[42] T. Dursun and C. Soutis. Recent developments in advanced aircraft aluminium alloys. *Mater. Des.*, **56** (2014) 862.

[43] J. Hirsch, B. Skrotzki and G. Gottstein. *Aluminium alloys: the physical and mechanical properties*, volume 1. John Wiley & Sons, 1st edition (2008).

[44] A. Biswas, D. J. Siegel, C. Wolverton and D. N. Seidman. Precipitates in Al–Cu alloys revisited: Atom-probe tomographic experiments and first-principles calculations of compositional evolution and interfacial segregation. *Acta Mater.*, **59** (2011) 6187.

[45] T. Sheppard. *Extrusion of aluminium alloys*. Springer Science & Business Media, 1st edition (1999).

[46] J. G. Kaufman. *Introduction to aluminum alloys and tempers*. ASM International, 1st edition (2000).

[47] V. S. Zolotorevsky, N. A. Belov and M. V. Glazoff. *Casting aluminum alloys*, volume 12. Elsevier Amsterdam, 2nd edition (2007).

[48] H. Wiedersich. Hardening mechanisms and the theory of deformation. *J. Min. Met. Mater. Soc.*, **16** (1964) 425.

[49] European Aluminium Association. *The Automotive Manual: Materials–Designation System*. European Aluminium Association (2002).

[50] B. Milkereit, N. Wanderka, C. Schick and O. Kessler. Continuous cooling precipitation diagrams of Al–Mg–Si alloys. *Mater. Sci. Eng. A*, **550** (2012) 87.

[51] M. Werinos, H. Antrekowitsch, T. Ebner, R. Prillhofer, P. J. Uggowitzer and S. Pogatscher. Hardening of Al–Mg–Si alloys: Effect of trace elements and prolonged natural aging. *Mater. Des.*, **107** (2016) 257.

[52] D. A. Porter and K. E. Easterling. *Phase transformations in metals and alloys.* CRC press, 3rd revised edition (2009).

[53] H. Zoller and A. Ried. Metallurgical aspects in the development of AlMgSi alloys with a low sensitivity to quenching. *Int. J. Mater. Res.*, **62** (1971) 354.

[54] J. Banhart, C. S. T. Chang, Z. Liang, N. Wanderka, M. D. Lay and A. J. Hill. Natural aging in Al-Mg-Si alloys – a process of unexpected complexity. *Adv. Eng. Mater.*, **12** (2010) 559.

[55] M. Murayama, K. Hono, M. Saga and M. Kikuchi. Atom probe studies on the early stages of precipitation in Al–Mg–Si alloys. *Mater. Sci. Eng. A*, **250** (1998) 127.

[56] M. Van Huis, J. Chen, M. Sluiter and H. Zandbergen. Phase stability and structural features of matrix-embedded hardening precipitates in Al–Mg–Si alloys in the early stages of evolution. *Acta Mater.*, **55** (2007) 2183.

[57] V. Fallah, B. Langelier, N. Ofori-Opoku, B. Raeisinia, N. Provatas and S. Esmaeili. Cluster evolution mechanisms during aging in Al–Mg–Si alloys. *Acta Mater.*, **103** (2016) 290.

[58] M. Liu, J. Čížek, C. S. Chang and J. Banhart. Early stages of solute clustering in an Al–Mg–Si alloy. *Acta Mater.*, **91** (2015) 355.

[59] P. H. Ninive, A. Strandlie, S. Gulbrandsen-Dahl, W. Lefebvre, C. D. Marioara, S. J. Andersen, J. Friis, R. Holmestad and O. M. Løvvik. Detailed atomistic insight into the β" phase in Al–Mg–Si alloys. *Acta Mater.*, **69** (2014) 126.

[60] M. Murayama and K. Hono. Pre-precipitate clusters and precipitation processes in Al–Mg–Si alloys. *Acta Mater.*, **47** (1999) 1537.

[61] G. Tao, C. Liu, J. Chen, Y. Lai, P. Ma and L. Liu. The influence of Mg/Si ratio on the negative natural aging effect in Al–Mg–Si–Cu alloys. *Mater. Sci. Eng. A*, **642** (2015) 241.

[62] M. Zandbergen, Q. Xu, A. Cerezo and G. Smith. Study of precipitation in Al–Mg–Si alloys by atom probe tomography I. Microstructural changes as a function of ageing temperature. *Acta Mater.*, **101** (2015) 136.

[63] S. Andersen, H. Zandbergen, J. Jansen, C. Træholt, U. Tundal and O. Reiso. The crystal structure of the β" phase in Al–Mg–Si alloys. *Acta Mater.*, **46** (1998) 3283.

[64] C. D. Marioara, S. Andersen, H. Zandbergen and R. Holmestad. The influence of alloy composition on precipitates of the Al–Mg–Si system. *Metall. Mater. Trans. A*, **36** (2005) 691.

[65] K. Matsuda, T. Naoi, S. Ikeno, Y. Uetani, T. Sato and A. Kamio. High resolution energy-filtering transmission electron microscopy for equilibrium β-phase in an Al–Mg–Si alloy. *Scr. Mater.*, **41** (1999) 4.

[66] F. J. Ehlers, S. Dumoulin and R. Holmestad. 3D modelling of β" in Al–Mg–Si: Towards an atomistic level ab initio based examination of a full precipitate enclosed in a host lattice. *Comput. Mater. Sci.*, **91** (2014) 200.

[67] P. Dumitraschkewitz, P. J. Uggowitzer, S. S. Gerstl, J. F. Löffler and

S. Pogatscher. Size-dependent diffusion controls natural aging in aluminium alloys. *Nat. Commun.*, **10** (2019) 1.

[68] C.-S. Tsao, C.-Y. Chen, U.-S. Jeng and T.-Y. Kuo. Precipitation kinetics and transformation of metastable phases in Al–Mg–Si alloys. *Acta Mater.*, **54** (2006) 4621.

[69] R. Vissers, M. v. van Huis, J. Jansen, H. Zandbergen, C. Marioara and S. Andersen. The crystal structure of the β' phase in Al–Mg–Si alloys. *Acta Mater.*, **55** (2007) 3815.

[70] S. Andersen, C. Marioara, A. Frøseth, R. Vissers and H. Zandbergen. Crystal structure of the orthorhombic U2-Al4Mg4Si4 precipitate in the Al–Mg–Si alloy system and its relation to the β' and β" phases. *Mater. Sci. Eng. A*, **390** (2005) 127.

[71] C. Marioara, H. Nordmark, S. Andersen and R. Holmestad. Post-β" phases and their influence on microstructure and hardness in 6xxx Al–Mg–Si alloys. *J. Mater. Sci.*, **41** (2006) 471.

[72] K. Matsuda, Y. Sakaguchi, Y. Miyata, Y. Uetani, T. Sato, A. Kamio and S. Ikeno. Precipitation sequence of various kinds of metastable phases in Al-1.0 mass% Mg2Si-0.4 mass% Si alloy. *J. Mater. Sci.*, **35** (2000) 1 179.

[73] A. Geisler and J. Hill. Analyses and interpretations of X-ray diffraction effects in patterns of aged alloys. *Acta Crystallogr.*, **1** (1948) 238.

[74] K. Matsuda, S. Ikeno, K. Terayama, H. Matsui, T. Sato and Y. Uetani. Comparison of precipitates between excess Si-type and balanced-type Al–Mg–Si alloys during continuous heating. *Metall. Mater. Trans. A*, **36** (2005) 2007.

[75] L. Hadjadj, R. Amira, D. Hamana and A. Mosbah. Characterization of precipitation and phase transformations in Al–Zn–Mg alloy by the differential dilatometry. *J. Alloys Compd.*, **462** (2008) 279.

[76] N. A. Belov, D. G. Eskin and A. A. Aksenov. *Multicomponent phase diagrams: applications for commercial aluminum alloys*. Elsevier, 1st edition (2005).

[77] K. Momma and F. Izumi. Vesta 3 for three-dimensional visualization of crystal, volumetric and morphology data. *J. Appl. Crystallogr.*, **44** (2011) 1272.

[78] C. Leyens and M. Peters. *Titanium and titanium alloys: fundamentals and applications*. John Wiley & Sons, 1st edition (2003).

[79] M. Kaur and K. Singh. Review on titanium and titanium based alloys as biomaterials for orthopaedic applications. *Mater. Sci. Eng. C*, **102** (2019) 844.

[80] J. C. Williams and R. R. Boyer. Opportunities and issues in the application of titanium alloys for aerospace components. *Metals*, **10** (2020) 705.

[81] M. Jackson and K. Dring. A review of advances in processing and metallurgy of titanium alloys. *Mater. Sci. Technol.*, **22** (2006) 881.

[82] J. Williams, B. Hickman and H. Marcus. The effect of omega phase on the mechanical properties of titanium alloys. *Metall. Trans.*, **2** (1971) 1913.

[83] M. Lai, T. Li, F. Yan, J. Li and D. Raabe. Revisiting ω phase embrittlement in metastable β titanium alloys: Role of elemental partitioning. *Scr. Mater.*, **193** (2021) 38.

[84] A. Devaraj, V. V. Joshi, A. Srivastava, S. Manandhar, V. Moxson, V. A. Duz and C. Lavender. A low-cost hierarchical nanostructured beta-titanium alloy with high strength. *Nat. Commun.*, **7** (2016) 1.

[85] J. Zhang, C. C. Tasan, M. Lai, A.-C. Dippel and D. Raabe. Complexion-mediated martensitic phase transformation in Titanium. *Nat. Commun.*, **8** (2017) 1.

[86] T. Li, D. Kent, G. Sha, L. Stephenson, A. Ceguerra, S. Ringer, M. Dargusch and J. Cairney. New insights into the phase transformations to isothermal ω and ω-assisted α in near β-Ti alloys. *Acta Mater.*, **106** (2016) 353.

[87] G. Lindwall, P. Wang, U. R. Kattner and C. E. Campbell. The effect of oxygen on phase equilibria in the Ti-V system: impacts on the AM processing of Ti alloys. *J. Min. Met. Mater. Soc.*, **70** (2018) 1692.

[88] M. Tane, H. Nishiyama, A. Umeda, N. L. Okamoto, K. Inoue, M. Luckabauer, Y. Nagai, T. Sekino, T. Nakano and T. Ichitsubo. Diffusionless isothermal omega transformation in titanium alloys driven by quenched-in compositional fluctuations. *Phys. Rev. Mater.*, **3** (2019) 043604.

[89] P. Frost, W. Parris, L. Hirsch, J. Doig and C. Schwartz. Isothermal transformation of titanium-chromium alloys. *Trans. Am. Soc. Met.*, **46** (1954) 231.

[90] Y. Vohra, E. Menon, S. Sikka and R. Krishnan. High pressure studies on a prototype omega forming alloy system. *Acta Metall.*, **29** (1981) 457.

[91] S. Banerjee and P. Mukhopadhyay. *Phase transformations: Examples from titanium and zirconium alloys.* Elsevier, 1st edition (2010).

[92] N. L. Okamoto, S. Kasatani, M. Luckabauer, R. Enzinger, S. Tsutsui, M. Tane and T. Ichitsubo. Evolution of microstructure and variations in mechanical properties accompanied with diffusionless isothermal ω transformation in β-titanium alloys. *Phys. Rev. Mater.*, **4** (2020) 123603.

[93] S. Banerjee, R. Tewari and P. Mukhopadhyay. Coupling of displacive and replacive ordering. *Prog. Mater. Sci.*, **42** (1997) 109.

[94] D. De Fontaine. Mechanical instabilities in the bcc lattice and the beta to omega phase transformation. *Acta Metall.*, **18** (1970) 275.

[95] D. De Fontaine, N. Paton and J. Williams. The omega phase transformation in titanium alloys as an example of displacement controlled reactions. *Acta Metall.*, **19** (1971) 1153.

[96] J. Williams, D. De Fontaine and N. Paton. The ω-phase as an example of an unusual shear transformation. *Metall. Trans.*, **4** (1973) 2701.

[97] M. Li and X. Min. Origin of ω-phase formation in metastable β-type Ti-Mo alloys: cluster structure and stacking fault. *Sci. Rep.*, **10** (2020) 1.

[98] M. K. Koul. *Transformation and deformation studies in titanium alloys.* Ph.D. thesis, Massachusetts Institute of Technology (1968).

[99] B. Hickman. The formation of omega phase in titanium and zirconium alloys: A review. *J. Mater. Sci.*, **4** (1969) 554.

[100] S. Nag, A. Devaraj, R. Srinivasan, R. Williams, N. Gupta, G. Viswanathan, J. Tiley, S. Banerjee, S. Srinivasan, H. Fraser et al. Novel mixed-mode phase transition involving a composition-dependent displacive component. *Phys. Rev. Lett.*, **106** (2011) 245701.

[101] A. Devaraj, S. Nag, R. Srinivasan, R. Williams, S. Banerjee, R. Banerjee and H. Fraser. Experimental evidence of concurrent compositional and structural instabilities leading to ω precipitation in titanium–molybdenum alloys. *Acta Mater.*, **60** (2012) 596.

[102] M. Hida, E. Sukedai and H. Terauchi. Microscopic approaches to isothermal transformation of incommensurate omega phase zones in Ti-20wt% Mo alloy studied by XDS, HREM and EXAFS. *Acta Metall.*, **36** (1988) 1429.

[103] J. E. Gragg. The omega phase in titanium-vanadium alloys. *Master Thesis*, (1964).

[104] T. Duerig, G. Terlinde and J. Williams. Phase transformations and tensile properties of Ti-10V-2Fe-3Al. *Metall. Trans. A*, **11** (1980) 1987.

[105] A. Devaraj, R. Williams, S. Nag, R. Srinivasan, H. Fraser and R. Banerjee. Three-dimensional morphology and composition of omega precipitates in a binary titanium–molybdenum alloy. *Scr. Mater.*, **61** (2009) 701.

[106] J. Murdock and C. McHargue. Self-diffusion in body-centered cubic titanium-vanadium alloys. *Acta Metall.*, **16** (1968) 493.

[107] N. L. Okamoto, S. Kasatani, M. Luckabauer, M. Tane and T. Ichitsubo. Effects of solute oxygen on kinetics of diffusionless isothermal ω transformation in β-titanium alloys. *Scr. Mater.*, **188** (2020) 88.

[108] F. Prima, P. Vermaut, G. Texier, D. Ansel and T. Gloriant. Evidence of α-nanophase heterogeneous nucleation from ω particles in a β-metastable Ti-based alloy by high-resolution electron microscopy. *Scr. Mater.*, **54** (2006) 645.

[109] S. Azimzadeh and H. Rack. Phase transformations in Ti-6.8 Mo-4.5 Fe-1.5 Al. *Metall. Mater. Trans. A*, **29** (1998) 2455.

[110] S. Nag, R. Banerjee, R. Srinivasan, J. Hwang, M. Harper and H. Fraser. ω-Assisted nucleation and growth of α precipitates in the Ti-5Al–5Mo–5V–3Cr–0.5 Fe β titanium alloy. *Acta Mater.*, **57** (2009) 2136.

[111] Y. Xia, J. Zhao, Q. Tian and X. Guo. Review of the effect of oxygen on titanium and deoxygenation technologies for recycling of titanium metal. *J. Min. Met. Mater. Soc.*, **71** (2019) 3209.

[112] V. Molokanov, D. Chernov and P. Budberg. Solubility of vanadium in α titanium. *Met. Sci. Heat Treat.*, **19** (1977) 704.

[113] H. Adenstedt, J. Pequignot and J. Raymer. The titanium-vanadium system. *Trans. Am. Soc. Met.*, **44** (1952) 990.

[114] G. Aurelio, A. F. Guillermet, G. Cuello and J. Campo. Metastable phases in the Ti-V system: Part I. neutron diffraction study and assessment of structural properties. *Metall. Mater. Trans. A*, **33** (2002) 1307.

[115] R. Wood. The lattice constants of high purity alpha titanium. *Proc. Phys. Soc.*, **80** (1962) 783.

[116] P. Hidnert. Thermal expansion of titanium. *J. Res. NIST*, **30** (1943) 1934 101.

[117] Y. M. Kozlovskii and S. Stankus. Thermal expansion of vanadium in the temperature range of 98–2400 K. *J. Phys. Conf. Ser .*, **1677** (2020) 012167.

[118] L. Vegard. Die Konstitution der Mischkristalle und die Raumfüllung der Atome. *Z. Phys.*, **5** (1921) 17.

[119] M. Hendrickson. *The role of misfit strain and oxygen content on formation and evolution of omega precipitate in metastable beta-titanium alloys*. Ph.D. thesis, University of North Texas (2016).

[120] D. Choudhuri, Y. Zheng, T. Alam, R. Shi, M. Hendrickson, S. Banerjee, Y. Wang, S. Srinivasan, H. Fraser and R. Banerjee. Coupled experimental and computational investigation of omega phase evolution in a high misfit titanium-vanadium alloy. *Acta Mater.*, **130** (2017) 215.

[121] L. Resch, G. Klinser, E. Hengge, R. Enzinger, M. Luckabauer, W. Sprengel and R. Würschum. Precipitation processes in Al–Mg–Si extending down to initial clustering revealed by the complementary techniques of positron lifetime spectroscopy and dilatometry. *J. Mater. Sci.*, **53** (2018) 14657.

[122] M. Starink. Kinetic equations for diffusion-controlled precipitation reactions. *J. Mater. Sci.*, **32** (1997) 4061.

[123] S. Vyazovkin and C. Wight. Kinetics in solids. *Annu. Rev. Phys. Chem.*, **48** (1997) 125.

[124] E.-S. Lee and Y. G. Kim. A transformation kinetic model and its application to cu–zn–al shape memory alloys I. isothermal conditions. *Acta Metall. Mater.*, **38** (1990) 1669.

[125] M. Starink. On the meaning of the impingement parameter in kinetic equations for nucleation and growth reactions. *J. Mater. Sci.*, **36** (2001) 4433.

[126] R. Fortunier, J. Leblond and J. Bergheau. A numerical model for multiple phase transformations in steels during thermal processes. *J. Shanghai Jiaotong Univ.*, **5** (2000) 213.

[127] J. Austin and R. Rickett. Kinetics of the decomposition of austenite at constant temperature. *Trans. AIME*, **135** (1939) 396.

[128] F. Cumbrera and F. Sanchez-Bajo. The use of the JMAYK kinetic equation for the analysis of solid-state reactions: critical considerations and recent interpretations. *Thermochim. Acta*, **266** (1995) 315.

[129] J. W. Christian. *The theory of transformations in metals and alloys.* Newnes, 3rd edition (2002).

[130] K. Edalati and Z. Horita. A review on high-pressure torsion (HPT) from 1935 to 1988. *Mater. Sci. Eng. A*, **652** (2016) 325.

[131] G. Gottstein. *Materialwissenschaft und Werkstofftechnik: Physikalische Grundlagen.* Springer-Verlag, 4th edition (2013).

[132] E. Kirkendall. Rates of diffusion of copper and zinc in alpha brass. *Trans. AIME*, **133** (1939) 186.

[133] E. Kirkendall. Diffusion of zinc in alpha brass. *Trans. AIME*, **147** (1942) 104.

[134] R. Simmons and R. Balluffi. Measurements of equilibrium vacancy concentrations in aluminum. *Phys. Rev.*, **117** (1960) 52.

[135] J. Rösler and E. Arzt. The kinetics of dislocation climb over hard particles–I. climb without attractive particle-dislocation interaction. *Acta Metall.*, **36** (1988) 1043.

[136] H.-E. Schaefer, K. Frenner and R. Würschum. Time-differential length change measurements for thermal defect investigations: Intermetallic B2-FeAl and B2-NiAl compounds, a case study. *Phys. Rev. Lett.*, **82** (1999) 948.

[137] J. A. Kotzurek, E.-M. Steyskal, B. Oberdorfer, A. Hohenwarter, R. Pippan, W. Sprengel and R. Würschum. Direct measurement of vacancy relaxation by dilatometry. *Appl. Phys. Lett.*, **109** (2016) 021906.

[138] W. Cai and W. D. Nix. *Imperfections in Crystalline Solids.* Cambridge University Press, 1st edition (2016).

[139] A. Hohenwarter and R. Pippan. Sample size and strain-rate-sensitivity effects on the homogeneity of high-pressure torsion deformed disks. *Metall. Mater. Trans. A*, **50** (2019) 601.

[140] Q. Wei, S. Cheng, K. Ramesh and E. Ma. Effect of nanocrystalline and ultrafine grain sizes on the strain rate sensitivity and activation volume: Fcc versus bcc metals. *Mater. Sci. Eng. A*, **381** (2004) 71.

[141] B. Oberdorfer, E.-M. Steyskal, W. Sprengel, W. Puff, P. Pikart, C. Hugenschmidt, M. Zehetbauer, R. Pippan and R. Würschum. In situ probing of fast defect annealing in Cu and Ni with a high-intensity positron beam. *Phys. Rev. Lett.*, **105** (2010) 146101.

[142] A. P. Zhilyaev and T. G. Langdon. Long-term self-annealing of copper and aluminium processed by high-pressure torsion. *J. Mater. Sci.*, **49** (2014) 6529.

[143] J. Crank. *The mathematics of diffusion.* Oxford university press, 2nd edition (1979).

[144] T. Ozawa. Non-isothermal kinetics of diffusion and its application to thermal analysis. *J. Therm. Anal.*, **5** (1973) 563.

[145] D. N. Seidman and R. Balluffi. Sources of thermally generated vacancies in single-crystal and polycrystalline gold. *Phys. Rev.*, **139** (1965) A1824.

[146] W. Wycisk and M. Feller-Kniepmeier. Quenching experiments in high purity Ni. *J. Nucl. Mater.*, **69** (1978) 616.

[147] R. Pippan, S. Scheriau, A. Taylor, M. Hafok, A. Hohenwarter and A. Bachmaier. Saturation of fragmentation during severe plastic deformation. *Annu. Rev. Mater. Res.*, **40** (2010) 319.

[148] E.-M. Steyskal. Untersuchung freier Volumen in submikrokristallinem Nickel mit der Methode der Dilatometrie. *Master thesis*, (2010).

[149] D. Setman, M. B. Kerber, E. Schafler and M. J. Zehetbauer. Activation enthalpies of deformation-induced lattice defects in severe plastic deformation nanometals measured by differential scanning calorimetry. *Metall. Mater. Trans. A*, **41** (2010) 810.

[150] D. Setman, E. Schafler, E. Korznikova and M. J. Zehetbauer. The presence and nature of vacancy type defects in nanometals detained by severe plastic deformation. *Mater. Sci. Eng. A*, **493** (2008) 116.

[151] P. Ehrhart, P. Jung, H. Schultz and H. Ullmaier. Landolt-börnstein-group III condensed matter: Atomic defects in metals (1991).

[152] D. W. Henderson. Thermal analysis of non-isothermal crystallization kinetics in glass forming liquids. *J. Non Cryst. Solids*, **30** (1979) 301.

[153] E. Louis and C. Garcia-Cordovilla. On the determination of kinetic parameters through the peak temperature method for differential scanning calorimetry. *J. Therm. Anal. Calorim.*, **29** (1984) 1139.

[154] B. Oberdorfer, E.-M. Steyskal, W. Sprengel, R. Pippan, M. Zehetbauer, W. Puff and R. Würschum. Recrystallization kinetics of ultrafine-grained Ni studied by dilatometry. *J. Alloys Compd.*, **509** (2011) S309.

[155] R. Enzinger, C. Neubauer, J. Kotzurek, W. Sprengel and R. Würschum. Kinetics of vacancy annealing upon time-linear heating applied to dilatometry. *J. Mater. Sci.*, **53** (2018) 2758.

Acknowledgements

I would like to express my sincerest gratitude to the following persons for their manifold contributions to the success of this thesis and for their ongoing support over the last years:

Univ.-Prof. Dr. Roland Würschum, Institute of Materials Physics, TU Graz,
for giving me the opportunity to work on this doctoral thesis under his constant, valuable guidance and for his dedication throughout the past years and beyond. I am especially grateful for many fruitful discussions accentuated by a pleasant working atmosphere as well as for his support during the writing process of this thesis and of our publications.

Univ.-Prof. Dr. Jürgen Eckert, Chair of Materials Physics, University of Leoben,
for acting as an external reviewer for this thesis and for his valuable comments during the preliminary evaluation of this thesis.

Ass.-Prof. Dr. Martin Luckabauer, Faculty of Engineering Technology, University of Twente,
for giving the impetus to investigate the most interesting materials as well as for producing and providing the sample material. I am especially grateful for many fruitful discussions in an excellent working atmosphere and for his continuing support when struggling with technical issues.

Assoc.-Prof. Dr. Wolfgang Sprengel, Institute of Materials Physics, TU Graz,
for his ongoing help and support regarding all kinds of subjects, for the excellent working atmosphere and for many valuable comments and discussions.

Prof. Dr. Tetsu Ichitsubo and Prof. Dr. Norihiko Okamoto, Institute for Materials Research, Tohoku University,

and all members of this institute involved in the Ti-V-project for giving the impetus to investigate this alloy system, for the fruitful discussions and for providing the sample material, without which my research would not have been possible.

Univ.-Prof. Dr. Stefan Pogatscher, Chair of Nonferrous Metallurgy, University of Leoben,

for his collaboration and the fruitful discussions concerning the Al-Mg-Si-project.

Dr. Laura Resch and Dipl.-Ing. Elisabeth Hengge, Institute of Materials Physics, TU Graz,

especially for working with me at the Al-Mg-Si-project, for many fruitful discussions and for the always warm-hearted, honest and competent working atmosphere.

Dipl.-Ing. Ladislaus Lang-Quantzendorff and Dipl.-Ing. Florian Brumbauer, Institute of Materials Physics, TU Graz,

for the exceptionally pleasant and productive working atmosphere from the time on, when they became my colleagues. Special thanks to Ladislaus for designing and constructing with me the water cooled bottom plate for the dilatometer.

All present and former members of the Institute of Materials Physics, TU Graz,

for their continuous support and the magnificent working atmosphere during the last years.

My family and my friends,

in particular my sister Maria and my brother Stefan as well as my parents Maria and Walther, for managing so masterfully to provide me with spots of light, whenever necessary. Further thanks to Christoph, Christian and Stefanie, who provided me with the most welcome distractions and moments of leisure, whenever I needed them.

Most importantly, however, my greatest thanks go to my partner Dominik for his understanding, for his support and for being always there for me.

AFFIDAVIT

I declare that I have authored this thesis independently, that I have not used other than the declared sources/resources, and that I have explicitly indicated all material which has been quoted either literally or by content from the sources used. The text document uploaded to TUGRAZonline is identical to the present doctoral thesis.

Date, Signature